BEILSTEIN JOURNAL OF ORGANIC CHEMISTRY

Organic TADF materials design

Edited by Eli Zysman-Colman

Imprint

Beilstein Journal of Organic Chemistry
www.bjoc.org
ISSN 1860-5397
Email: journals-support@beilstein-institut.de

The *Beilstein Journal of Organic Chemistry* is published by the Beilstein-Institut zur Förderung der Chemischen Wissenschaften.

Beilstein-Institut zur Förderung der Chemischen Wissenschaften
Trakehner Straße 7–9
60487 Frankfurt am Main
Germany
www.beilstein-institut.de

BEILSTEIN JOURNAL OF ORGANIC CHEMISTRY

Comparative study of thermally activated delayed fluorescent properties of donor–acceptor and donor–acceptor–donor architectures based on phenoxazine and dibenzo[*a,j*]phenazine

Saika Izumi‡[1], Prasannamani Govindharaj‡[2], Anna Drewniak[2], Paola Zimmermann Crocomo[2], Satoshi Minakata[1], Leonardo Evaristo de Sousa[3], Piotr de Silva*[3], Przemyslaw Data*[2] and Youhei Takeda*[1]

Full Research Paper

Open Access

Address:
[1]Department of Applied Chemistry, Graduate School of Engineering, Osaka University, Yamadaoka 2-1, Suita, Osaka 5650871, Japan, [2]Faculty of Chemistry, Silesian University of Technology, Strzody 9, 44-100 Gliwice, Poland and [3]Department of Energy Conversion and Storage, Technical University of Denmark, Anker Engelunds Vej 301, 2800 Kongens Lyngby, Denmark

Email:
Piotr de Silva* - pdes@dtu.dk; Przemyslaw Data* - przemyslaw.data@polsl.pl; Youhei Takeda* - takeda@chem.eng.osaka-u.ac.jp

* Corresponding author ‡ Equal contributors

Keywords:
charge-transfer; dibenzophenazine; donor–acceptor; organic light-emitting diodes; thermally activated delayed fluorescence

Beilstein J. Org. Chem. **2022,** *18,* 459–468.
https://doi.org/10.3762/bjoc.18.48

Received: 21 February 2022
Accepted: 21 April 2022
Published: 25 April 2022

This article is part of the thematic issue "Organic TADF materials design".

Guest Editor: E. Zysman-Colman

Abstract

A new thermally activated delayed fluorescence (TADF) compound based on a donor–acceptor (D–A) architecture (D = phenoxazine; A = dibenzo[*a,j*]phenazine) has been developed, and its photophysical properties were characterized. The D–A compound is applicable as an emitting material for efficient organic light-emitting diodes (OLEDs), and its external quantum efficiency (EQE) exceeds the theoretical maximum of those with prompt fluorescent emitters. Most importantly, comparative study of the D–A molecule and its D–A–D counterpart from the viewpoints of the experiments and theoretical calculations revealed the effect of the number of the electron donor on the thermally activated delayed fluorescent behavior.

Introduction

Thermally activated delayed fluorescence (TADF), which was firstly reported in 1961 by Parker and Hatchard [1], is a fundamental photophysical phenomenon that refers to delayed fluorescence radiated from the singlet excited state (S_1) as a consequence of a brief detour to a triplet excited state (T_n) [i.e., intersystem crossing (ISC) and reverse intersystem crossing (rISC)].

Since the revisit of TADF in organic light-emitting diodes (OLEDs) by Adachi in 2012 [2], TADF-active compounds have emerged as emitters in high-performance organic light-emitting diodes (OLEDs) [3-8], biological probes [9], photocatalysis [10], and some others [11]. Specifically, TADF-active purely organic compounds allow for achieving a very high external quantum efficiency (EQE) of OLEDs without using precious metals such as Ir and Pt in the emitter. Thus, the development of TADF-active organic compounds, the establishment of materials design through systematic structure–property relationship (SPR), and the understanding of the TADF mechanism are highly important tasks in this research field.

The singlet–triplet energy splitting between the S_1 and T_1 states (ΔE_{ST}) and spin–orbit coupling (SOC) play key roles in manifesting the TADF character of an organic compound. To boost the rISC process, ideally, the ΔE_{ST} is zero or even negative [12,13], while the SOC is as large as possible. One of the promising molecular design strategies to meet the above-mentioned criteria involves a highly twisted $(D)_n$–$(A)_m$ (D: electron donor; A: electron acceptor) system, in which efficient intramolecular charge transfer (ICT) occurs in the singlet excited state (^{1}CT). An efficient rISC can be mediated by mixing the ^{1}CT state with a locally excited triplet state on the donor (^3LE_D) or the acceptor (^3LE_A) through spin–vibronic coupling [14] or non-Condon effects [15,16].

In 2016, we developed a twisted D–A–D compound **POZ-DBPHZ** (Figure 1) that exhibits efficient orange-to-red TADF [17], and the OLEDs fabricated with **POZ-DBPHZ** achieved a high EQE up to 16%. However, the role of the number of donors and molecular symmetry in the TADF character of **POZ-DBPHZ** remained unexplored, due to the lack of a synthetic method to the asymmetric D–A structure. Herein, we report the synthesis of a new asymmetric D–A compound **1** (Figure 1) as a TADF emitter and its detailed physical properties. Moreover, the developed emitter's performance was evaluated in an OLED device. To clarify the influence of the donor number and structural symmetry on the physicochemical properties of the DBPHZ-cored D–A system, the properties of D–A compound **1** were compared with those of **POZ-DBPHZ**. Theoretical calculations further support the impact of the donor numbers in the DBPHZ-cored D–A system.

Results and Discussion

Synthesis of materials

To synthesize the designed D–A molecule **1**, an asymmetric dibenzophenazine electrophile was required. Recently, we have established a synthetic method for such a compound, i.e., 3-trifluoromethanesulfonyldibenzo[*a*,*j*]phenazine (**DBPHZ-OTf** in Scheme 1) to prepare linear-type A–D–A–D compounds [18]. Starting from the mono-functionalized compound **DBPHZ-OTf**, the target compound **1** was successfully synthesized through a Pd-catalyzed Buchwald–Hartwig amination with phenoxazine (**POZ**) in a good yield as red-brown solid (Scheme 1). The D–A–D counterpart **POZ-DBPHZ** was synthesized according to the previously reported process [17]. It is noted that the solubility of the D–A compound **1** in organic solvents is lower than that of the D–A–D compound, indicating a more aggregated state of the D–A molecules in the solid state,

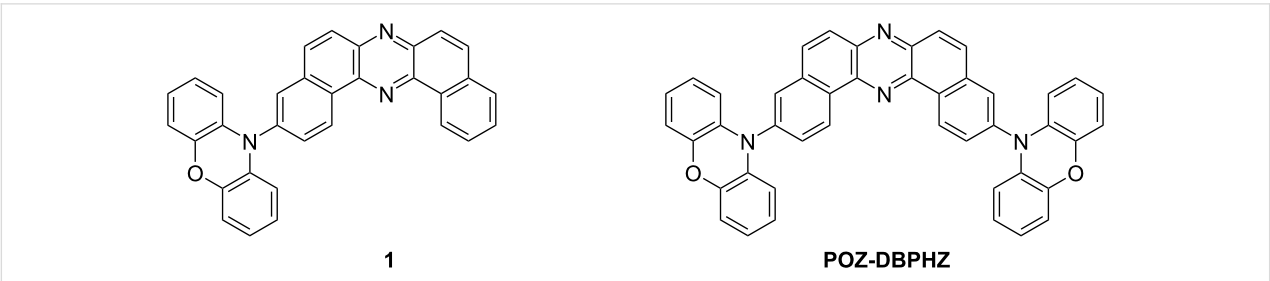

Figure 1: Chemical structures of **1** and **POZ-DBPHZ**.

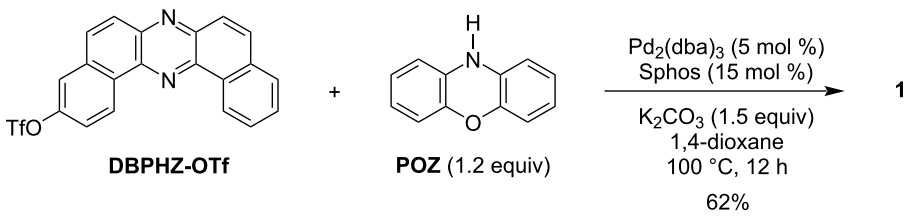

Scheme 1: Synthesis of compound **1**.

due to less steric hindrance on the acceptor plane arising from breaking the symmetry. The synthesized compound **1** was fully characterized by ^{1}H and ^{13}C NMR and IR spectroscopy, MS spectrometry as well as elemental analysis (for the detailed data, see Supporting Information File 1).

Steady-state PL spectra

To reveal the photophysical properties of diluted solutions of compound **1**, UV–vis absorption and steady-state photoluminescence (PL) spectra were acquired (Figure 2, and the summary of the properties presented in Table 1). The solutions were prepared with a variety of organic solvents at concentrations of ca. 10^{-5} M. It is noted that the solubility of **1** in cyclohexane is quite low, and thereby the concentration of the cyclohexane solution and the molar absorption coefficient ε were not determined. As is clearly seen from Figure 2, the absorption spectra were not affected by the dielectric constant of the solvents. In contrast, the emission peaks of the PL spectra drastically red-shifted from cyclohexane (λ_{PL} = 502 nm) to toluene (λ_{PL} = 608 nm), and no PL was observed in a more polar solvent such as THF and $CHCl_3$ (Figure 2). In addition, the shape of the PL spectrum changed from a vibrationally resolved shape typical of the emission from a locally excited state (^{1}LE) to a Gaussian-type broad one typical to the emission from a charge–transfer excited state (CT). The CT emission was totally quenched in a solvent that is more polar than toluene (Figure 2). These photophysical observations are consistent with those of the D–A–D-type compound **POZ-DBPHZ** [17], indicating that one D–A pair is sufficient for generating the CT excited state. In comparison with the photophysical properties of the D–A–D compound, the absorption of **1** (λ_{abs} = 461 nm) is almost the same as that of **POZ-DBPHZ** (λ_{abs} = 463 nm) [17], while the PL emission peak appeared in a slightly blue-shifted region (λ_{PL} = 502 nm) from D–A–D-type compound (λ_{PL} = 521 nm for **POZ-DBPHZ**) in cyclohexane. These data indicate that the effective length of π-conjugation is not affected by the number of donors, probably due to the right D–A dihedral angle for both compounds in the ground state. In contrary, the slight blue-shift of the PL spectra of the D–A compound **1** compared to **POZ-DBPHZ** reflects the contribution of an additional donor to relaxation of the molecular geometry in the excited state. The photoluminescence quantum yield (Φ_{PL}) of the D–A compound **1** is lower (0.13 in cyclohexane) than that of the D–A–D compound **POZ-DBPHZ** (0.33) [17], indicating a dominant non-radiative decay of the excited state for the D–A type compound, which was supported by the theoretical calculations (vide infra).

Table 1: Summary of steady-state photophysical data of diluted solutions of **1**.[a]

solvent	λ_{abs} (nm)	λ_{PL} (nm)	Φ_{PL}[b]
cyclohexane[c]	294, 389, 412	502	0.13
toluene	296, 393, 415	608	0.16
THF	295, 392, 415	–	<0.01
$CHCl_3$	295, 394, 416	–	<0.01

[a]Solution concentration: 10^{-5} M; [b]determined with an integrated sphere; [c]saturated solution was used, due to the low solubility in cyclohexane.

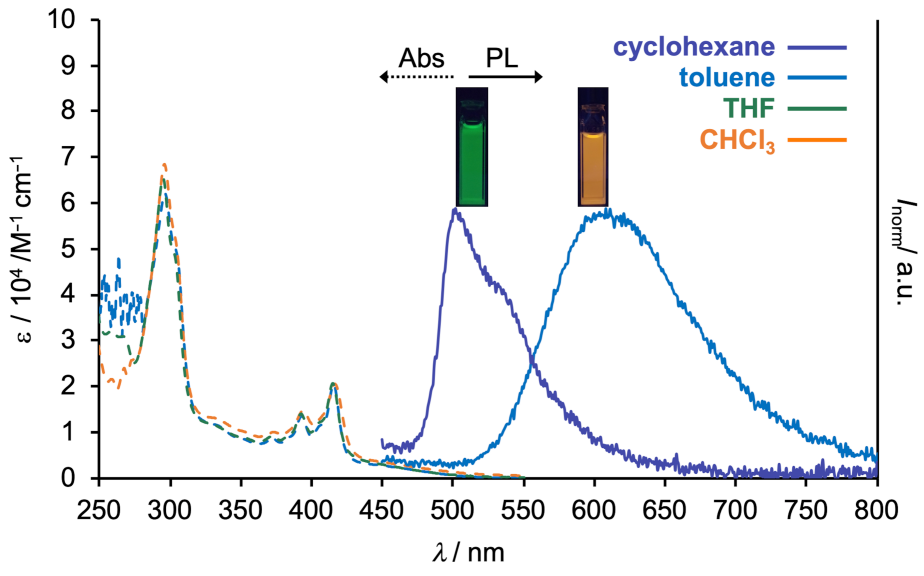

Figure 2: Steady-state UV–vis absorption (Abs) and photoluminescence (PL) spectra of dilute solutions ($c \approx 10^{-5}$ M) of compound **1**. The PL spectra were acquired with λ_{ex} = 340 nm for the cyclohexane solution and λ_{ex} = 360 nm for solutions in the other solvents.

In the solid state, the D–A compound **1** showed an emission at around λ_{em} = 560 nm with a very low Φ_{PL} (<0.1) (Figure S1 in Supporting Information File 1). The PL spectrum is similar to that in a CBP host matrix (vide infra). The compound **1** showed an aggregation-induced emission (AIE) behavior in a THF/water system, showing a more red-shifted emission peak at around λ_{em} = 600 nm when compared with the as-prepared solid state (Figure S2 in Supporting Information File 1). This indicates that in the as-prepared state and aggregation state the molecular stacking modes should be quite different from each other.

Time-resolved spectroscopic analysis

To investigate the delayed fluorescence behavior of the D–A compound **1**, more detailed photophysical studies were performed using a time-resolved spectroscopic technique (Figure 3). Time-resolved photoluminescence (PL) from a blended film (1 wt % of **1** in Zeonex®) at 300 K showed two-components emission consisting of a prompt fluorescence (PF) that decays within the order of nanoseconds and a delayed fluorescence (DF) that decays in the range of micro to milliseconds (Figure 3a). These PF and DF spectra are exactly overlapped with each other (Figure 3b), which indicated that both emis-

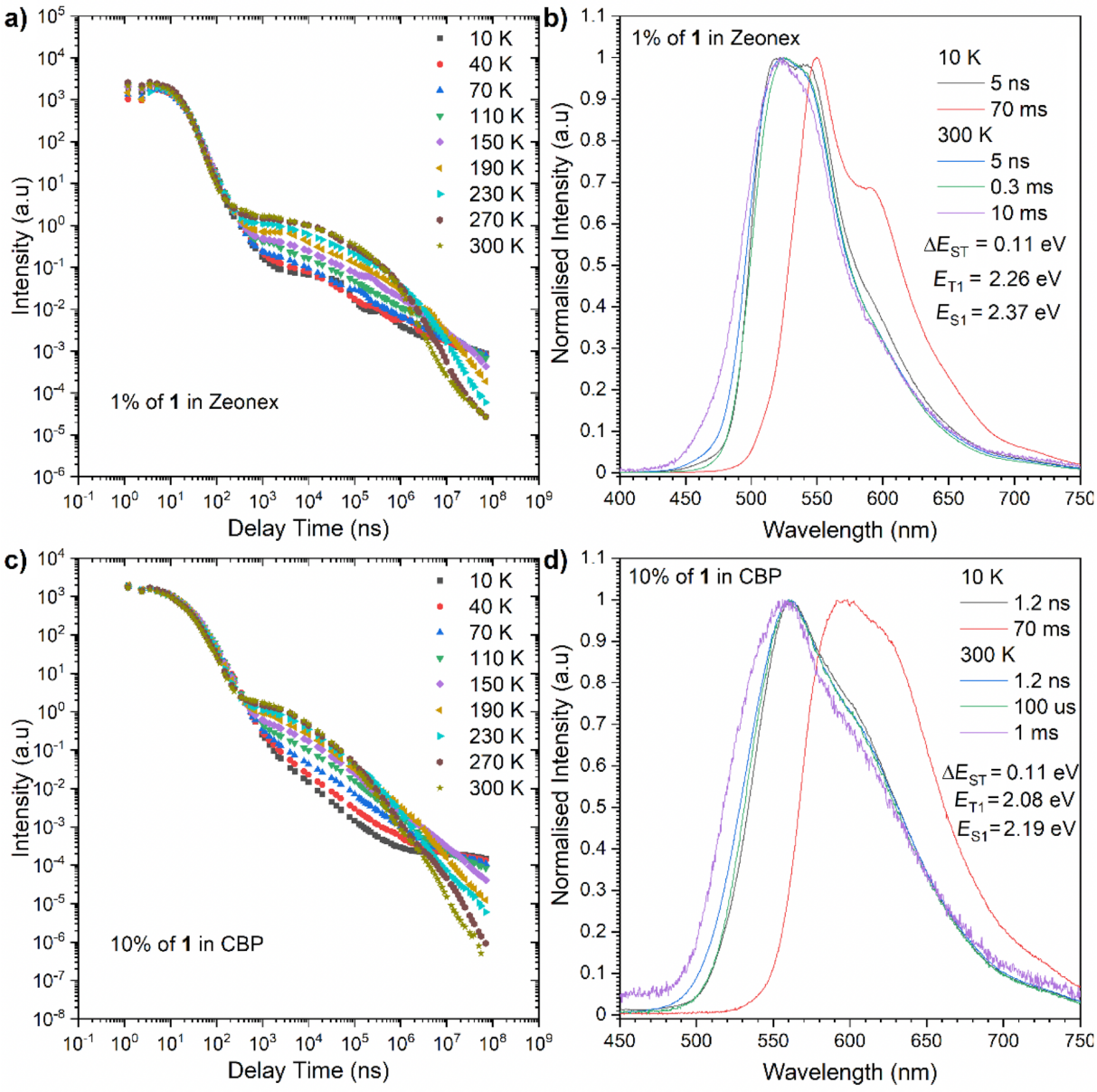

Figure 3: Time-resolved PL decay profiles (intensity vs delay time) and spectra of **1** in a), b) Zeonex® and c, d) CBP matrix. The energies correspond to the maximum emission peaks.

sions are radiated from the singlet excited state (S_1). Both emission spectra are not well resolved and in a Gaussian-type shape (Figure 2b), suggesting that these emissions have a mixed character of localized (^{1}LE) and charge-transfer state (^{1}CT, Figure 3b). The emission from the T_1 state (phosphorescence, PH) at a low temperature (10 K) with the energy of E_{T1} = 2.26 eV showed a similar spectral shape to the phosphorescence spectra of the acceptor core (DBPHZ) [17]. This would indicate that the T_1 state of the D–A compound is localized on the acceptor unit (^3LE_A). The ΔE_{ST} of **1** was found to be 0.11 eV, which is twice larger than that of **POZ-DBPHZ** in the same matrix (0.06 eV) [17]. These differences are ascribed to the change in electron density on the acceptor and the electron-donating power of POZ. Therefore, gradual increase of electron-donating strength brings T_1 energy closer to the acceptor T_1 energy and leads to a smaller E_{ST} gap. But, the activation energy E_a for the DF process, which was calculated from the Arrhenius plot obtained from the increase of the DF intensity against temperature, was lower for **1** (E_a = 27 meV) when compared to **POZ-DBPHZ** (E_a = 47 meV, Table 2) in Zeonex®. The directly determined activation energy of the D–A-type compound is half than that of the D–A–D compound, which is in contradiction to the ΔE_{ST} value (Table 2). If we support the observation with the DF/PF results that present a stronger TADF property for the mono-substituted derivative **1**, the conclusion of misleading ΔE_{ST} comparison can be reached. To avoid confusion, a more effective way is to compare only the activation energy of the DF process.

The time-resolved spectroscopic analysis of the emitter (10 wt % **1**) in an OLED matrix, 4,4'-bis(*N*-carbazolyl)-1,1'-biphenyl (CBP), revealed that the emission at 300 K yields a weaker DF when compared to the Zeonex® matrix (Figure 3c). In addition, the emission in CBP was more complicated, due to the emission spectra that move around with delay time (Figure S3, Supporting Information File 1). At 5.1 ns, the emission peak from PF was observed in a red-shifted region (by approximately 41 nm) than that observed in Zeonex® (λ_{em} = 524 nm) (Figure S3a in Supporting Information File 1). Thereafter, there was a monotonic red shift in the emission peak and the gradual increment during the delay time from 0 ns to 150 ns, and the largest red-shifted spectrum was found at 613 nm (at 150 ns) (Figure S3a, Supporting Information File 1). From 168 ns to 5 µs delay time, the emission peak plateaued at around λ_{em} = 607 nm (Figure S3b, Supporting Information File 1), then from 5 µs to 32 µs, a significant hypsochromic shift of the emission peak was observed down to 560 nm, and the emission peak stayed at this value (Figure S3c, Supporting Information File 1). This behavior brings the proposition that the PF in the nanosecond range based on a CT character with a little contribution from the ^{1}LE state have inhomogeneous energies. Firstly, the ^{1}LE state decays, and then decays of the lower-energy excited states follow. The triplet energy level of **1** is 2.08 eV, which is lower than that in Zeonex® (2.26 eV). A closer inspection of the transient curves and inset spectra at microsecond delays let us notice that the spectra shift slightly to lower energies (Figure S3 in Supporting Information File 1). This behavior is not unusual in CT-based emitters and can be explained by local interactions between the dipole moment of the host and the excited state dipole moment of the TADF molecule [19].

The activation energy for the TADF process of the D–A compound **1** is as low as 15 meV. Nevertheless, the TADF efficiency of the D–A compound in CBP is much lower when compared to that in Zeonex® and its D–A–D counterpart (Table 2). First, the DF/PF ratio is much smaller in CBP than in Zeonex®, suggesting a smaller triplet contribution to the overall emission. If we compare compound **1** with the previously studied D–A–D compound, the Φ_{PL} is slightly lower, but the highest impact is related with DF/PF, where **POZ-DBPHZ** has the twice higher value which in total should give a much lower performance in the device for **1**.

Thermal stability

To fabricate the OLED devices by thermal evaporation techniques, a high thermal stability is required. To evaluate the effect of the donor number on the thermal stability of the

Table 2: Summary of the general photophysical properties of compound **1**.

Compd.	host	λ_{em} [nm][a]	Φ_{PL}[b]	τ_{PF} [ns][c]	τ_{DF} [µs][d]	DF/PF[e]	E_a [eV][f]	S_1 [eV][g]	T_1 [eV][g]	ΔE_{ST} [eV][h]
1	Zeonex®	524	32.5	15.37 ± 1.35	6.9 ± 0.43	5.01	0.028	2.37	2.26	0.11
POZ-DBPHZ	Zeonex®	530	29.5	10.23 ± 0.16	26.4 ± 1.50	4.72	0.047	2.48	2.40	0.08
1	CBP	565	68.5	16.11 ± 0.38	2.96 ± 0.18	0.98	0.015	2.19	2.08	0.11
POZ-DBPHZ	CBP	595	79.0	2.7 ± 0.21	0.47 ± 0.04	1.94	0.019	2.28	2.26	0.02

[a]The maximum wavelength of photoluminescence spectra; [b]photoluminescence quantum yield in degassed; [c]prompt fluorescence lifetime; [d]delayed fluorescence lifetime; [e]the ratio of delayed fluorescence (DF) to prompt fluorescence (PF); [f]activation energy of the triplet to singlet transfer (error ± 0.01 eV); [g]singlet and triplet energy (error ± 0.03 eV); [h]energy splitting (error ± 0.05 eV). All parameters estimated at 300 K.

DBPHZ-cored D–A type emitter, the degradation temperature T_d (5 wt % loss) was investigated by thermogravimetric analysis (TGA), which showed a high T_d (5 wt % loss under N_2 atmosphere) of compound **1** (342 °C) (Figure S4a in Supporting Information File 1), which is high enough for a thermal deposition process. However, when compared with the D–A–D counterpart, the T_d of **1** is much lower (by 111 °C) than that of **POZ-DBPHZ** (453 °C) [17]. These data would support that the increase in the sterically hindered donors in emitting molecule suppress intermolecular contact to enhance the thermal stability.

OLED fabrication and characterization

The OLED device was fabricated and characterized in the CBP host (Figure 4). The HOMO–LUMO values obtained from the electrochemical measurement (Figure S5 in Supporting Information File 1) were used to evaluate whether the emitter works in a previously analyzed device structure [17]. The OLED device structure applied the following configuration: –ITO/NPB [*N*,*N*'-di(1-naphthyl)-*N*,*N*'-diphenyl-(1,1'-biphenyl)-4,4'-diamine] (40 nm)/10% of **1** in CBP (20 nm)/TPBi [2,2',2''-(1,3,5-benzinetriyl)-tris(1-phenyl-1*H*-benzimidazole)] (20 nm)/BCP (bathocuproine)] (20 nm)/LiF (1 nm)/Al (100 nm)– (Figure 4).

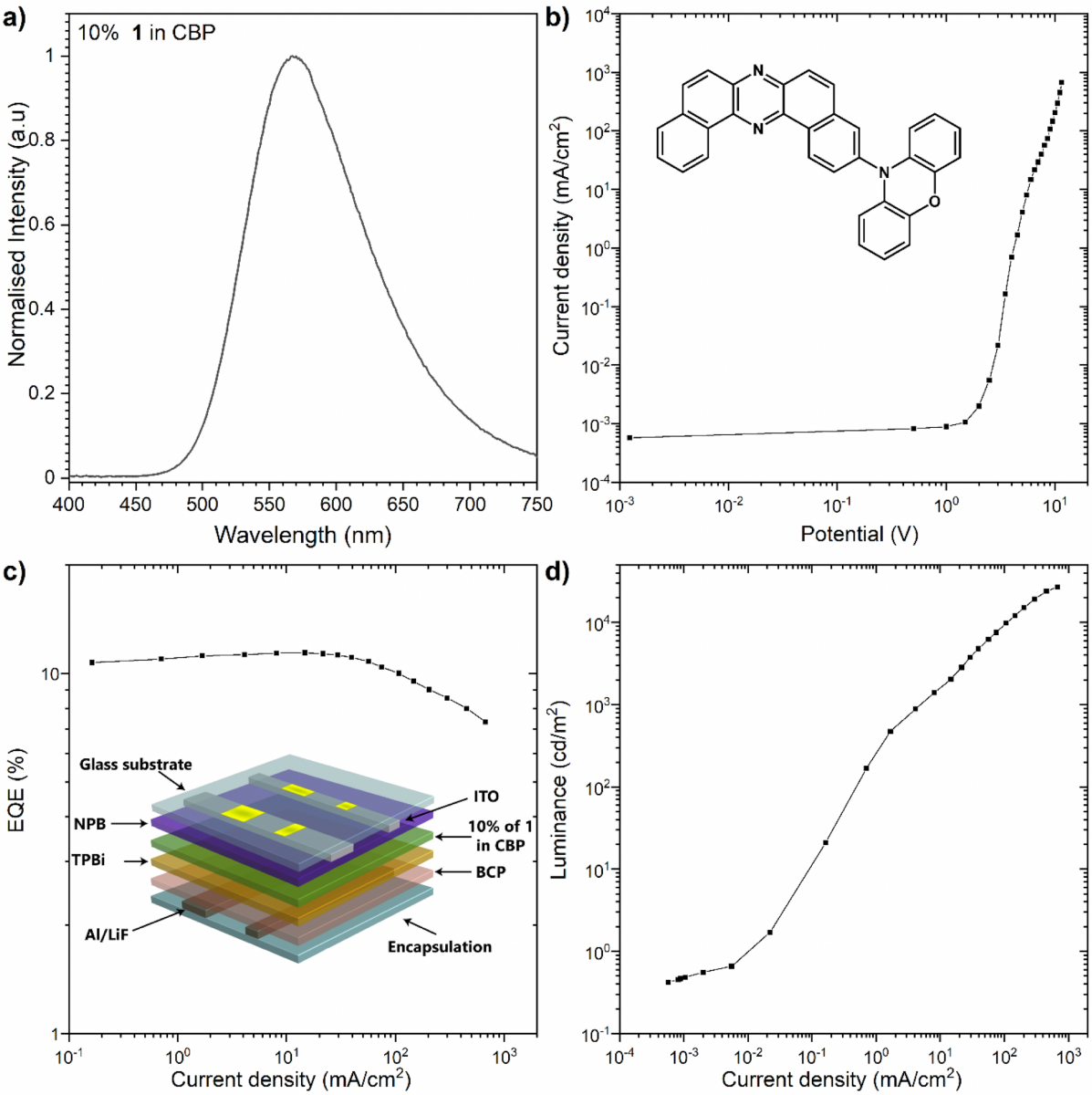

Figure 4: The characteristics of the OLED devices: a) electroluminescence spectra; b) current density-bias characteristics; c) EQE–current density characteristics; d) luminance–current density characteristics.

The external quantum efficiency (EQE) was measured at around 11.4%, where the device fabricated with the previously studied D–A–D compound **POZ-DBPHZ** showed 16%. As for luminance, a high luminance of 27,060 cd/m^2 was obtained, which is slightly lower than that we previously reported (>35,000 cd/m^2) [17]. A positive aspect about the device fabricated with compound **1** is the lower efficiency roll-off when compared with the previously studied D–A–D emitter. As the result, the efficiency is higher for the D–A compound **1** above 10,000 cd/m^2, and at the luminance, the EQE was kept around 10%, whereas in the case of doubly donor-substituted compound **POZ-DBPHZ**, the EQE dropped below 10% [17].

Theoretical calculations

We performed electronic structure calculations on both the D–A (**1**) and D–A–D (**POZ-DBPHZ**) compounds to understand better their respective TADF mechanisms and the efficacy of introducing two electronic donors on the acceptor unit. The calculations employed density functional theory (DFT) with the long-range corrected ωPBE functional and the 6-31G(d,p) basis set. Tuning of the range separation parameter was performed for both molecules [20] with the results collected in Table S1 (Supporting Information File 1). The Tamm–Dancoff (TDA) approximation was used in all excited state calculations and solvent effects were included by means of the polarizable continuum model (PCM) associated with a perturbative state specific solvation method using toluene as solvent. The photophysics of both molecules was analyzed using a unified approach for photophysical rate calculations that employs the nuclear ensemble method as implemented in the NEMO software [21,22] interfaced with the QChem 5.0 program suite [23]. A total of 500 geometries were sampled for each molecule and for each relevant electronic state. From these calculations, emission spectra were computed along with fluorescence, phosphorescence, and ISC rates, providing us insight into the mechanism behind the photophysical behavior of the molecules under analysis in this work.

Taking fluorescence properties as starting point, the simulations point out considerable similarity between the spectra of the D–A and D–A–D compounds. As shown in Figure S6 (Supporting Information File 1), the calculated fluorescence peaks lie at 510 nm and 505 nm for the D–A and D–A–D compounds, respectively. These results agree very well with those obtained from the measurement in Zeonex® (Table 2), which has a similar dielectric constant as toluene (≈2.3), the solvent used in the calculations. A comparison with results from steady-state PL spectra (Table 1), however, show that the predicted peak matches measurements made with cyclohexane, but appear to be blue shifted with respect to measurements in toluene. Considering that cyclohexane has only a slightly lower dielectric constant (≈2.0) than toluene, it is reasonable that calculations would produce similar predictions, which makes the red-shifted experimental emission in toluene more surprising. In addition to similarities in fluorescence energy, the D–A (**1**) and D–A–D (**POZ-DBPHZ**) compounds share very close calculated fluorescence rates (2.2×10^7 s^{-1} and 1.8×10^7 s^{-1}, respectively) which translate into prompt fluorescence lifetimes of 45 ns and 54 ns, respectively. These values are in the same order of magnitude as the experimental lifetimes shown in Table 2, further indicating the appropriateness of the theoretical approach.

From the first singlet excited state, we have estimated ISC rates for both molecules. Table S5 in Supporting Information File 1 shows the calculated ISC rates from S_1 to the first five triplet states. For both molecules, the estimated rate values are comparable or larger than those for fluorescence, which makes the ISC process competitive. Comparing all available processes from the S_1 state, we are able to estimate probabilities for each transition (detailed in Supporting Information File 1, Table S8 and Table S9). In the case of the D–A compound **1**, the singlet population is expected to split mostly into T_1 (33%) and T_2 states (42%), with about 2% probability expected for prompt fluorescence. On the other hand, for the D–A–D compound **POZ-DBPHZ**, transitions to T_1 display 48% probability whereas fluorescence has around 4%. The remaining probabilities are mostly distributed between transfers to T_2 and T_3 with about 20% each.

Transfers to higher lying triplet states may end up relaxing to the lowest triplet state by means of internal conversion. In this sense, it is important to look into the energy gaps between triplet states of both molecules. Considering the average gaps taken from all the conformations sampled in the nuclear ensemble from the T_1 state geometry, we obtain T_1 to T_2 gaps of approximately 0.4 eV for both compounds. This significant value suggests the possibility of the T_2 population not necessarily decaying to T_1 instantly. In contrast, the average energy difference between two adjacent triplet levels above T_2 is approximately 0.1 eV for both molecules, which indicates that internal conversion should be very efficient.

Following the above observations, we estimated rISC rates from the first two triplet states of both molecules and the results are collected in Table S6 and Table S7 (Supporting Information File 1). It is worth noting, that the D–A–D compound **POZ-DBPHZ** presents rISC rates that are larger than those of its D–A counterpart **1** by roughly one order of magnitude, which suggests that the addition of an extra donor unit is able to improve the TADF efficiency. For both triplet states, rISC transfers to S_1 are overwhelmingly larger than those to higher

singlet states. Similarly, these transfer rates to S_1 are orders of magnitude larger than estimated phosphorescence rates (Table S3 in Supporting Information File 1). The analysis of the probabilities associated with each transfer mechanism from T_1 and T_2 (shown in Table S8 and Table S9 of Supporting Information File 1) indicates that the expected depopulation mechanism for the first two triplet states is dominated by an rISC back to the first excited singlet state, which is responsible for the TADF behavior observed in both molecules.

The rate estimates finally allow us to paint a picture of the TADF mechanism of the two compounds. This is schematically shown in Figure 5, along with the calculated rates for each of the represented processes. In addition, we present natural transition orbitals (NTOs) for the three excited states most relevant for the TADF mechanism. These NTOs demonstrate the similar CT character of the S_1 state of both compounds, which helps explain their coinciding fluorescence spectra. Finally, the NTOs for the triplet states indicate a possible source for the difference in their TADF efficiencies. Whereas the first two triplet states of the D–A compound **1** correspond mostly to excitations localized in the acceptor fragment, the T_1 and T_2 states on the D–A–D molecule **POZ-DBPHZ** display a mixed CT/LE character. It is known that having two states with different electronic characters allows for larger spin–orbit couplings, so we would expect these couplings to be larger in the case of the D–A molecule when comparing with the D–A–D compound. This is indeed the case, as the average spin–orbit coupling for the T_1 to S_1 transition in the D–A compound **1** is 0.462 meV, whereas for the D–A–D compound **POZ-DBPHZ** it is 0.177 meV. However, the average energy gap taken from all geometries in the nuclear ensemble for this transition is 0.37 eV for the D–A–D compound and 0.71 eV for the D–A molecule. As such, the higher similarity in electronic character between the singlet and triplet states of the D–A–D molecule was enough to decrease the average energy gap without compromising significantly the spin–orbit coupling, resulting in an overall better TADF performance.

Conclusion

In conclusion, we have developed a new D–A-type TADF compound and investigated its physicochemical properties for comparison with the corresponding D–A–D analogue. The number of donor units has no effect on the absorption, due to the highly twisted D–A(–D) structures, while an additional donor unit led to a slight red shift in photoluminescence by the stabilization of the charge-transfer singlet excited states (^{1}CT). Most importantly, the additional donor unit not only lowers the ^{1}CT energy but also is bringing the T_1 energy to the approximation of the ^3LE_A energy, leading to a narrower singlet–triplet energy gap and a more efficient TADF process, when compared with the mono-donor-substituted compound. On one hand, the comparison of the activation energy for the TADF process for the two compounds gave an inversed order of energy. In addition, the one-less number of donor units in the molecular scaffold led to lower solubility in organic solvents and thermal stability, presumably due to the less steric hindrance around the π-extended conjugated acceptor unit with the unsymmetric molecule structure. The OLEDs fabricated with the D–A emitter achieved a good EQE up to 11%, which exceeds the theoretical

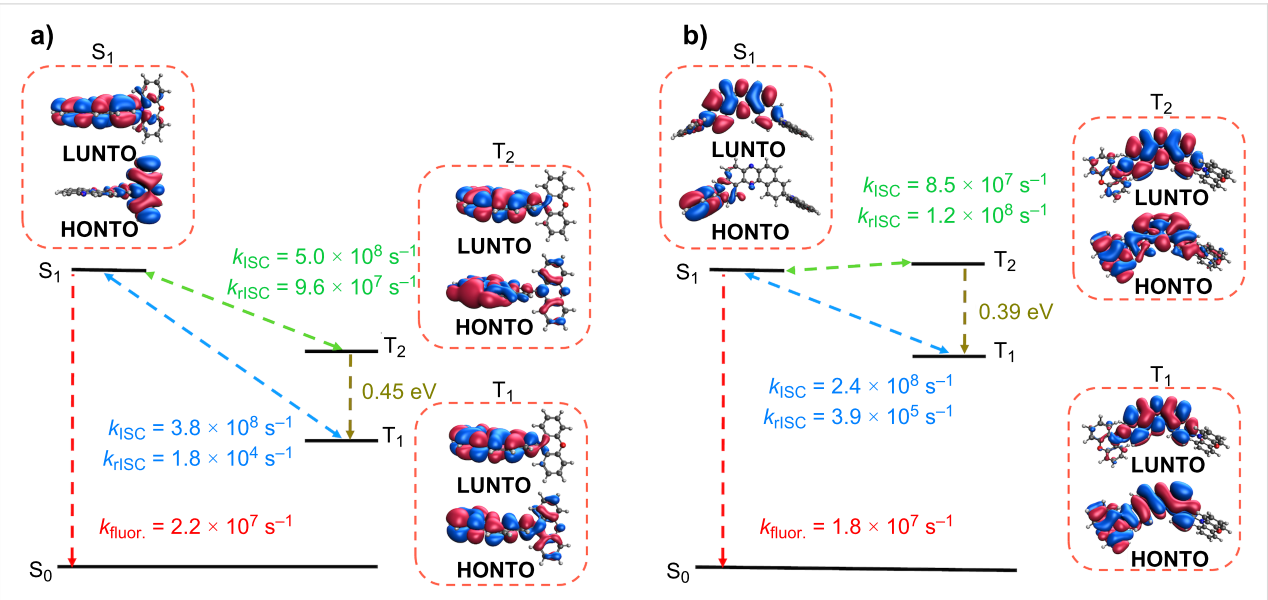

Figure 5: Schematics of the TADF mechanisms along with NTOs for the relevant electronic states for a) D–A compound **1** and b) D–A–D compound **POZ-DBPHZ**.

maximum (ca. 5%) of prompt fluorescent emitter-based OLEDs. The additional donor gave a better EQE of the OLED device than that fabricated with the D–A compound, due to a less efficient TADF process. Taken together the experimental and theoretical calculations, the role of the additional donor unit in the TADF mechanism is boosting the rISC process by balancing the singlet–triplet energy gap and spin–orbit coupling. The results showcased herein would allow for designing efficient TADF emitters more flexibly in the future.

Supporting Information

Supporting Information File 1

General information, synthetic procedures, spectral data, photophysical data, and theoretical calculation data.
[https://www.beilstein-journals.org/bjoc/content/supplementary/1860-5397-18-48-S1.pdf]

Funding

Y.T. acknowledges a Grant-in-Aid for Scientific Research on Innovative Area “Aquatic Functional Materials: Creation of New Materials Science for Environment-Friendly and Active Functions” (JSPS KAKENHI Grant Number JP19H05716) from the MEXT (Ministry of Education, Culture, Science and Technology, Japan), a Grant-in-Aid for Scientific Research (B) (JSPS KAKENHI Grant Number JP20H02813), and the Continuation Grants for Young Researchers from the Asahi Glass Foundation. Y.T. and S.M. acknowledge NIPPOH CHEMICALS for supplying *N,N*-diiodo-5,5-dimethylhydantoin (DIH). P. de S. and L. E. de S. acknowledge support by a research grant (00028053) from VILLUM FONDEN. Y.T., P.G. A.D. P.Z.C., P. de S. and P.D. acknowledge the EU’s Horizon 2020 for funding the OCTA project under grant agreement No 778158. Research work supported from the funds for science in 2018–2022 allocated to the implementation of an international co-financed project by the Polish Ministry of Education and Science. P.D. acknowledges the Polish National Science Centre funding, grant no. 2018/31/B/ST5/03085. P.G. acknowledges the supporting awards from the Silesian University of Technology (BKM-532/RCH4/2021). P.D., P.G., A.D. and P.Z.C. acknowledge the supporting actions from EU's Horizon 2020 ERA-Chair project ExCEED, grant agreement No 952008.

ORCID® iDs

Prasannamani Govindharaj - https://orcid.org/0000-0002-4400-2265
Leonardo Evaristo de Sousa - https://orcid.org/0000-0002-5880-5325
Piotr de Silva - https://orcid.org/0000-0002-4985-7350
Przemyslaw Data - https://orcid.org/0000-0002-1831-971X
Youhei Takeda - https://orcid.org/0000-0001-9103-4238

References

1. Parker, C. A.; Hatchard, C. G. *Trans. Faraday Soc.* **1961,** *57,* 1894–1904. doi:10.1039/tf9615701894
2. Uoyama, H.; Goushi, K.; Shizu, K.; Nomura, H.; Adachi, C. *Nature* **2012,** *492,* 234–238. doi:10.1038/nature11687
3. Tao, Y.; Yuan, K.; Chen, T.; Xu, P.; Li, H.; Chen, R.; Zheng, C.; Zhang, L.; Huang, W. *Adv. Mater. (Weinheim, Ger.)* **2014,** *26,* 7931–7958. doi:10.1002/adma.201402532
4. Yang, Z.; Mao, Z.; Xie, Z.; Zhang, Y.; Liu, S.; Zhao, J.; Xu, J.; Chi, Z.; Aldred, M. P. *Chem. Soc. Rev.* **2017,** *46,* 915–1016. doi:10.1039/c6cs00368k
5. Liu, Y.; Li, C.; Ren, Z.; Yan, S.; Bryce, M. R. *Nat. Rev. Mater.* **2018,** *3,* 18020. doi:10.1038/natrevmats.2018.20
6. Huang, T.; Jiang, W.; Duan, L. *J. Mater. Chem. C* **2018,** *6,* 5577–5596. doi:10.1039/c8tc01139g
7. Chen, X.-K.; Kim, D.; Brédas, J.-L. *Acc. Chem. Res.* **2018,** *51,* 2215–2224. doi:10.1021/acs.accounts.8b00174
8. Nakanotani, H.; Tsuchiya, Y.; Adachi, C. *Chem. Lett.* **2021,** *50,* 938–948. doi:10.1246/cl.200915
9. Nguyen, V.-N.; Kumar, A.; Lee, M. H.; Yoon, J. *Coord. Chem. Rev.* **2020,** *425,* 213545. doi:10.1016/j.ccr.2020.213545
10. Candish, L.; Collins, K. D.; Cook, G. C.; Douglas, J. J.; Gómez-Suárez, A.; Jolit, A.; Keess, S. *Chem. Rev.* **2022,** *122,* 2907–2980. doi:10.1021/acs.chemrev.1c00416
11. Data, P.; Takeda, Y. *Chem. – Asian J.* **2019,** *14,* 1613–1636. doi:10.1002/asia.201801791
12. de Silva, P. *J. Phys. Chem. Lett.* **2019,** *10,* 5674–5679. doi:10.1021/acs.jpclett.9b02333
13. Wagner, J.; Zimmermann Crocomo, P.; Kochman, M. A.; Kubas, A.; Data, P.; Lindner, M. *Angew. Chem., Int. Ed.* **2022,** in press. doi:10.1002/anie.202202232
14. Im, Y.; Kim, M.; Cho, Y. J.; Seo, J.-A.; Yook, K. S.; Lee, J. Y. *Chem. Mater.* **2017,** *29,* 1946–1963. doi:10.1021/acs.chemmater.6b05324
15. de Silva, P.; Kim, C. A.; Zhu, T.; Van Voorhis, T. *Chem. Mater.* **2019,** *31,* 6995–7006. doi:10.1021/acs.chemmater.9b01601
16. de Sousa, L. E.; de Silva, P. *ChemRxiv* **2022**. doi:10.26434/chemrxiv-2022-pq978
17. Data, P.; Pander, P.; Okazaki, M.; Takeda, Y.; Minakata, S.; Monkman, A. P. *Angew. Chem., Int. Ed.* **2016,** *55,* 5739–5744. doi:10.1002/anie.201600113
18. Izumi, S.; Higginbotham, H. F.; Nyga, A.; Stachelek, P.; Tohnai, N.; de Silva, P.; Data, P.; Takeda, Y.; Minakata, S. *J. Am. Chem. Soc.* **2020,** *142,* 1482–1491. doi:10.1021/jacs.9b11578
19. Dias, F. B.; Penfold, T. J.; Monkman, A. P. *Methods Appl. Fluoresc.* **2017,** *5,* 012001. doi:10.1088/2050-6120/aa537e
20. Stein, T.; Kronik, L.; Baer, R. *J. Am. Chem. Soc.* **2009,** *131,* 2818–2820. doi:10.1021/ja8087482
21. de Sousa, L. E.; de Silva, P. *J. Chem. Theory Comput.* **2021,** *17,* 5816–5824. doi:10.1021/acs.jctc.1c00476
22. *NEMO,* Version 0.2.0; de Sousa, L. E., https://github.com/LeonardoESousa/NEMO.

23. Shao, Y.; Gan, Z.; Epifanovsky, E.; Gilbert, A. T. B.; Wormit, M.; Kussmann, J.; Lange, A. W.; Behn, A.; Deng, J.; Feng, X.; Ghosh, D.; Goldey, M.; Horn, P. R.; Jacobson, L. D.; Kaliman, I.; Khaliullin, R. Z.; Kuś, T.; Landau, A.; Liu, J.; Proynov, E. I.; Rhee, Y. M.; Richard, R. M.; Rohrdanz, M. A.; Steele, R. P.; Sundstrom, E. J.; Woodcock, H. L., III; Zimmerman, P. M.; Zuev, D.; Albrecht, B.; Alguire, E.; Austin, B.; Beran, G. J. O.; Bernard, Y. A.; Berquist, E.; Brandhorst, K.; Bravaya, K. B.; Brown, S. T.; Casanova, D.; Chang, C.-M.; Chen, Y.; Chien, S. H.; Closser, K. D.; Crittenden, D. L.; Diedenhofen, M.; DiStasio, R. A., Jr.; Do, H.; Dutoi, A. D.; Edgar, R. G.; Fatehi, S.; Fusti-Molnar, L.; Ghysels, A.; Golubeva-Zadorozhnaya, A.; Gomes, J.; Hanson-Heine, M. W. D.; Harbach, P. H. P.; Hauser, A. W.; Hohenstein, E. G.; Holden, Z. C.; Jagau, T.-C.; Ji, H.; Kaduk, B.; Khistyaev, K.; Kim, J.; Kim, J.; King, R. A.; Klunzinger, P.; Kosenkov, D.; Kowalczyk, T.; Krauter, C. M.; Lao, K. U.; Laurent, A. D.; Lawler, K. V.; Levchenko, S. V.; Lin, C. Y.; Liu, F.; Livshits, E.; Lochan, R. C.; Luenser, A.; Manohar, P.; Manzer, S. F.; Mao, S.-P.; Mardirossian, N.; Marenich, A. V.; Maurer, S. A.; Mayhall, N. J.; Neuscamman, E.; Oana, C. M.; Olivares-Amaya, R.; O'Neill, D. P.; Parkhill, J. A.; Perrine, T. M.; Peverati, R.; Prociuk, A.; Rehn, D. R.; Rosta, E.; Russ, N. J.; Sharada, S. M.; Sharma, S.; Small, D. W.; Sodt, A.; Stein, T.; Stück, D.; Su, Y.-C.; Thom, A. J. W.; Tsuchimochi, T.; Vanovschi, V.; Vogt, L.; Vydrov, O.; Wang, T.; Watson, M. A.; Wenzel, J.; White, A.; Williams, C. F.; Yang, J.; Yeganeh, S.; Yost, S. R.; You, Z.-Q.; Zhang, I. Y.; Zhang, X.; Zhao, Y.; Brooks, B. R.; Chan, G. K. L.; Chipman, D. M.; Cramer, C. J.; Goddard, W. A., III; Gordon, M. S.; Hehre, W. J.; Klamt, A.; Schaefer, H. F., III; Schmidt, M. W.; Sherrill, C. D.; Truhlar, D. G.; Warshel, A.; Xu, X.; Aspuru-Guzik, A.; Baer, R.; Bell, A. T.; Besley, N. A.; Chai, J.-D.; Dreuw, A.; Dunietz, B. D.; Furlani, T. R.; Gwaltney, S. R.; Hsu, C.-P.; Jung, Y.; Kong, J.; Lambrecht, D. S.; Liang, W.; Ochsenfeld, C.; Rassolov, V. A.; Slipchenko, L. V.; Subotnik, J. E.; Van Voorhis, T.; Herbert, J. M.; Krylov, A. I.; Gill, P. M. W.; Head-Gordon, M. *Mol. Phys.* **2015,** *113,* 184–215. doi:10.1080/00268976.2014.952696

License and Terms

BEILSTEIN JOURNAL OF ORGANIC CHEMISTRY

Substituent effect on TADF properties of 2-modified 4,6-bis(3,6-di-*tert*-butyl-9-carbazolyl)-5-methylpyrimidines

Irina Fiodorova[1], Tomas Serevičius[*2], Rokas Skaisgiris[2], Saulius Juršėnas[2] and Sigitas Tumkevicius[*1]

Full Research Paper

Open Access

Address:
[1]Institute of Chemistry, Vilnius University, Naugarduko 24, LT-03225, Vilnius, Lithuania and [2]Institute of Photonics and Nanotechnology, Vilnius University, Saulėtekio 3, LT-10257 Vilnius, Lithuania

Email:
Tomas Serevičius[*] - tomas.serevicius@tmi.vu.lt;
Sigitas Tumkevicius[*] - sigitas.tumkevicius@chf.vu.lt

* Corresponding author

Keywords:
carbazole; pyrimidine; RTP; synthesis; thermally activated delayed fluorescence

Beilstein J. Org. Chem. **2022,** *18,* 497–507.
https://doi.org/10.3762/bjoc.18.52

Received: 04 March 2022
Accepted: 28 April 2022
Published: 05 May 2022

This article is part of the thematic issue "Organic TADF materials design".

Guest Editor: E. Zysman-Colman

Abstract

The interest in organic materials exhibiting thermally activated delayed fluorescence (TADF) significantly increased in recent years owing to their potential application as emitters in highly efficient organic light emitting diodes (OLEDs). Simple modification of the molecular structure of TADF compounds through the selection of different electron-donating or accepting fragments opens great possibilities to tune the emission properties and rates. Here we present the synthesis of a series of novel pyrimidine–carbazole emitters and their photophysical characterization in view of effects of substituents in the pyrimidine ring on their TADF properties. We demonstrate that electron-withdrawing substituents directly connected to the pyrimidine unit have greater impact on the lowering of the energy gap between singlet and triplet states (ΔE_{ST}) for efficient TADF as compared to those attached through a phenylene bridge. A modification of the pyrimidine unit with CN, SCH_3, and SO_2CH_3 functional groups at position 2 is shown to enhance the emission yield up to 0.5 with pronounced TADF activity.

Introduction

The first reports on highly efficient thermally activated delayed fluorescence (TADF) mechanism and its successful realization in organic light emitting diodes (OLEDs) by Adachi and co-workers [1,2] have drawn the attention to the design and synthesis of various emissive donor–acceptor organic compounds. Efficient triplet harvesting in TADF compounds leads to internal quantum efficiencies up to 100% and electroluminescence yields exceeding 20% [3,4]. TADF OLEDs usually contain pure organic molecules, which avoid expensive noble metals and allow broad possibilities of molecular design. One of

the main requirement for efficient TADF is a negligible energy difference between the lowest singlet and triplet states (ΔE_{ST}) which is often obtained in (hetero)aromatic compounds possessing twisted electron-donor (D) and acceptor (A) fragments with strong intramolecular charge transfer (ICT) [5-7]. Moreover, the number and nature of various side units on the emitter framework can also affect the properties of TADF compounds [3]. Among the electron-donating units, 9,10-dihydroacridine, carbazole or phenoxazine derivatives often are used as D units, while the π-electron-deficient nitrogen heterocycles such as triazine, diazines or aromatics containing cyano and sulfone groups are popular acceptor units for the construction of highly efficient TADF emitters [8-11]. Pyrimidine (1,3-diazine) owing to its aromaticity, significant π-deficiency, strong electron affinity, high luminous efficiency, good electrical and optical properties, and easy chemical modification is a desired structural unit in organic structures targeted for numerous applications including organic photovoltaic solar cells (OPV) [12-14], organic field-effect transistors (OFETs) [15-17], chemical and biosensors [18-23], and OLEDs [3,7-9,24]. In case of TADF emitters, a pyrimidine ring is often connected with a donor unit through a phenylene group as a conjugate π-spacer (s) [25-28]. As the majority of research describes TADF compounds with D-s–A–s–D layout, reports on TADF properties of pyrimidine emitters where the pyrimidine moiety is directly bonded with a donor moiety are scarce [29-31], though several examples of such pyrimidine-based conjugates found utility as high triplet energy hosts [32,33]. Envisaging the potential of the pyrimidine–carbazole pair for achieving efficient deep-blue emission, we were interested to study the influence of substituents in position 2 of the pyrimidine ring on the TADF properties of pyrimidine–carbazole emitters. For this purpose, we performed the synthesis of novel 4,6-bis(3,6-di-*tert*-butyl-9*H*-carbazol-9-yl)pyrimidines modified with various substituents in position 2 of the pyrimidine ring (Figure 1).

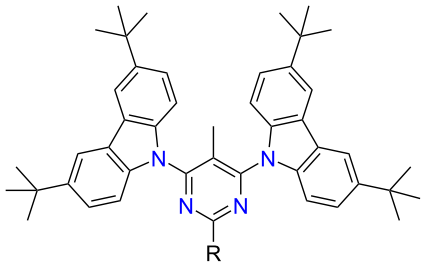

R = H, SMe, SO_2Me, CN, Ph, 4-CNC_6H_4, 3-CNC_6H_4, 3-BrC_6H_4, SC_6H_4-*t*-Bu-4, $SO_2C_6H_4$-*t*-Bu-4

Figure 1: 2-Modified 4,6-bis(3,6-di-*tert*-butyl-9*H*-carbazol-9-yl)-5-methylpyrimidines.

For comparison, analysis of the TADF properties of a similar pyrimidine–carbazole emitter **tCbz-mPYR** is also included in this paper [29]. To enhance the electron-accepting character of the pyrimidine moiety some electron-withdrawing groups, namely cyano, bromo or sulfonyl groups were introduced directly or through a phenylene bridge into position 2 of the pyrimidine ring.

Results and Discussion

Synthesis

Due to the versatile reactivity of a methylthio group in the pyrimidine nucleus [34,35] we used 4,6-bis(3,6-di-*tert*-butyl-9*H*-carbazol-9-yl)-5-methyl-2-methylthiopyrimidine (**tCbz-mPYR**) as a starting material for the synthesis of 2-substituted pyrimidine emitters (Scheme 1). Compound **tCbz-mPYR** was synthesized by using the palladium-catalyzed Buchwald–Hartwig amination reaction of 4,6-dichloro-5-methyl-2-methylpyrimidine with 3,6-di-*tert*-butylcarbazole according to the procedure reported by us previously [29].

In order to remove the methylthio group in **tCbz-mPYR** and to obtain the 2-unsubstituted pyrimidine derivative **1**, a hydrogenolysis reaction employing Raney Ni was carried out. Efficient methods for the introduction of aryl moieties into methylthio-substituted nitrogen heterocycles such as **tCBz-mPYR** are a Ni(0)-catalyzed cross-coupling reaction with Grignard reagents [34,36] or the Liebeskind–Srogl reaction employing arylboronic acids [37-39]. Taking into account a large assortment of arylboronic acids and the simplicity of the method, we chose the Liebeskind–Srogl cross-coupling reaction for the synthesis of the target 2-arylpyrimidine derivatives. Thus, heating **tCbz-mPYR** with phenyl-, 4-cyanophenyl-, 3-cyanophenyl-, or 3-bromophenylboronic acid at 130 °C in dioxane in the presence of $Pd(PPh_3)_4$, copper(I) 3-methylsalicylate (CuMeSal), and Cs_2CO_3 as a catalyst system furnished the corresponding 2-substituted pyrimidines **2a**–**d**. For the introduction of cyano and 4-(*tert*-butyl)phenylthio groups into position 2 of the pyrimidine, the conversion of the methylthio group to the better leaving methylsulfonyl group was necessary to perform. A suitable oxidant for this purpose appeared to be oxone [40]. Thus, the oxidation of **tCbz-mPYR** with oxone proceeded in DMF at 80 °C to provide the 2-methylsulfonyl derivative **3** in 92% yield. Then, treatment of compound **3** with NaCN or 4-(*tert*-butyl)thiophenol led to the formation of the 2-cyano- and 2-(4-*tert*-butylphenylthio) derivatives **4** and **5** in 65% and 77% yield, respectively. Finally, compound **5** in the reaction with oxone furnished 2-(4-*tert*-butylphenylsulfonyl) derivative **6** in reasonable 68% yield. ^1H and ^{13}C NMR spectroscopy and HRMS were employed to confirm the structures of the synthesized compounds (see Figures S1–S27 in Supporting Information File 1).

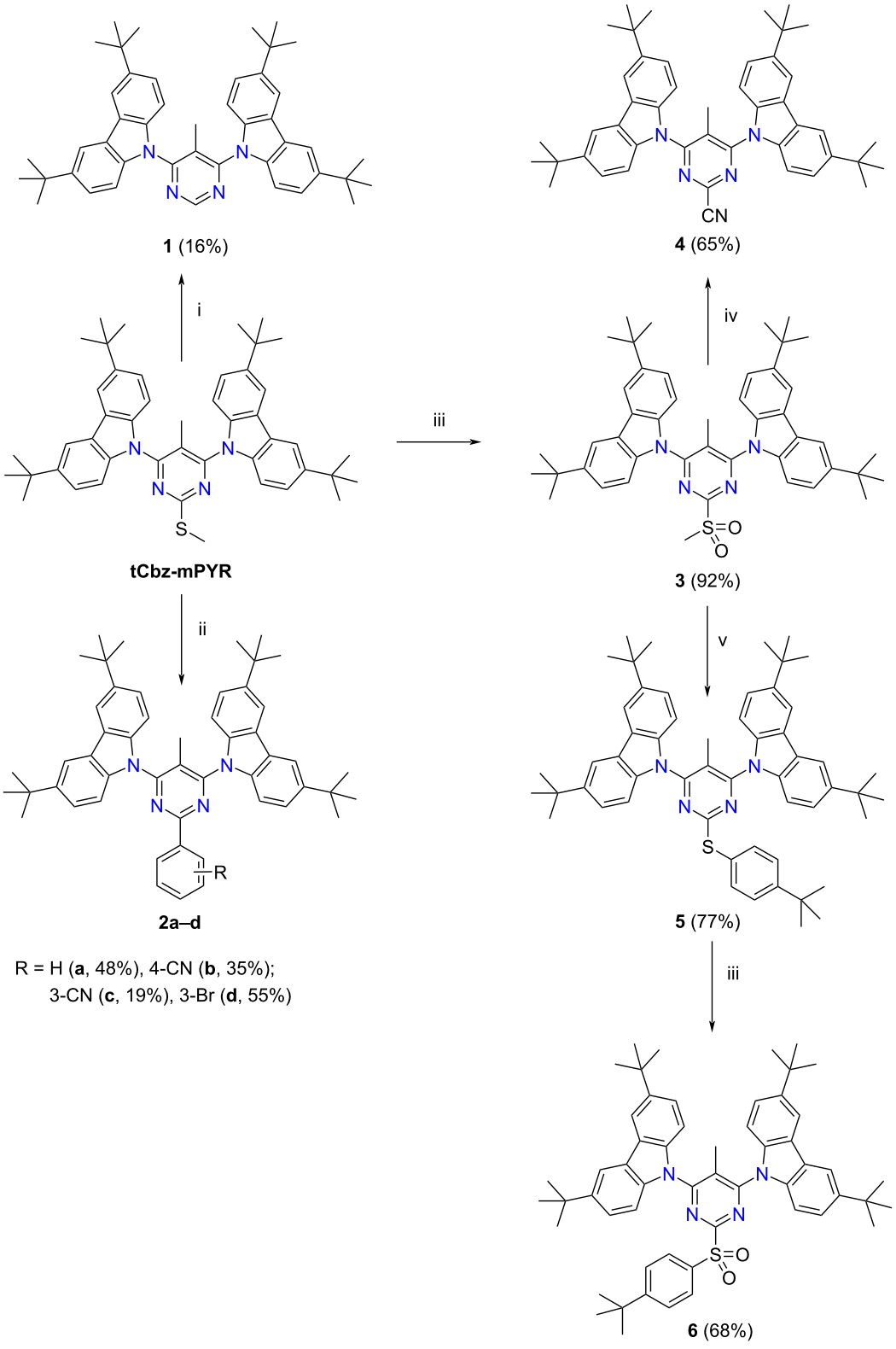

Scheme 1: Synthesis of 4,6-bis(3,6-di-*tert*-butyl-9*H*-carbazol-9-yl)-5-methyl-2-substituted pyrimidines **1**–**6**. Reagents and conditions: i – Raney Ni, MeOH, 90 °C, 2 h; ii – arylboronic acid (1.3 equiv), $Pd(PPh_3)_4$ (5 mol %), Cs_2CO_3 (2 equiv; 1 equiv in case of *meta*-substituted boronic acids), copper(I) 3-methylsalicylate (2.2 equiv), dioxane, 130 °C, 4 h, argon; iii – oxone (2.5 equiv), DMF, 80 °C, 3 h; iv – NaCN (2.2 equiv), THF, reflux, 3.5 h; v – 4-*t*-BuC_6H_4SH (1.1 equiv), Et_3N (1.1 equiv), THF, 50 °C, overnight, argon.

DFT analysis

To assess the structural and electronic properties of the chromophores **tCbz-mPYR** and **1**–**6**, quantum chemical calculations were performed. DFT analysis revealed that all studied compounds were of similar molecular geometry with partially twisted carbazole units (in the order of 45–47°). The steric hindrance between the carbazole fragments and the pyrimidine core was enhanced by introducing a methyl group in position 5 of the latter [29], enabling sufficient HOMO–LUMO decoupling. Single-bonded phenyl substituents (compounds **2a**–**d**) are almost coplanar with the pyrimidine core (dihedral angle 0.5–1.5°), while a phenyl group connected with the pyrimidine ring via a sulfur atom (compounds **5** and **6**) is twisted out of the pyrimidine plane and is not conjugated with the pyrimidine ring. Despite the similar molecular structures, the studied chromophores showed somewhat different electronic properties, mainly due to the variation of the acceptor structure. The DFT computed spatial distribution of frontier molecular orbitals (FMOs) of compounds **tCbz-mPYR** and **1**–**6** is presented in Figure 2. A comparison of the electronic structures revealed that the electron density distribution in the HOMO is rather similar for all molecules and tended to localize on the electron-donat-

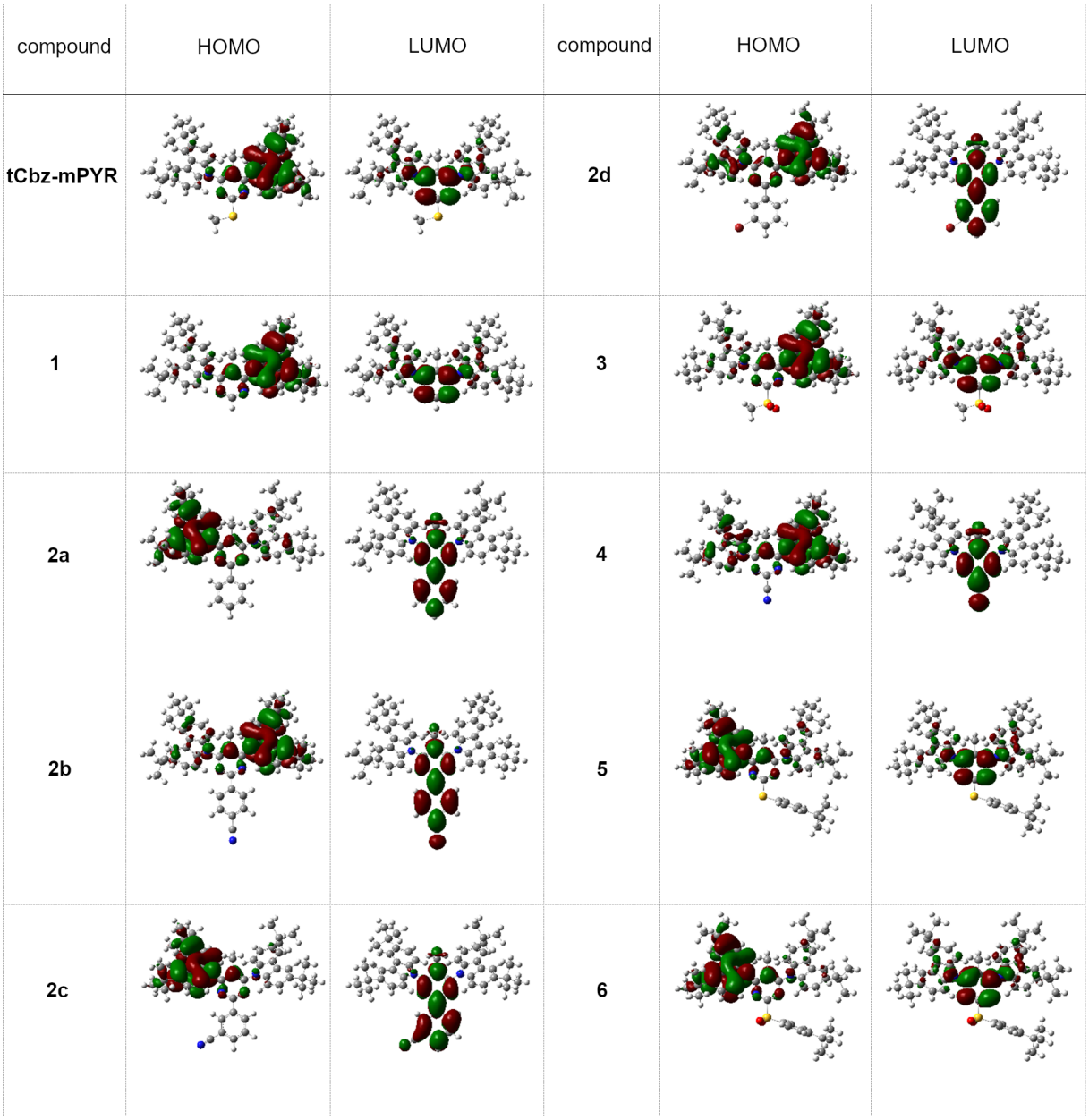

Figure 2: HOMO and LUMO spatial distributions of carbazole–pyrimidine TADF compounds.

ing carbazole moiety partially extending to the pyrimidine ring. The main differences in the electronic structure can be observed in the LUMO distribution. For the 2-methylthio- and 2-(*tert*-butylphenyl)thio-substituted compounds (**tCbz-mPYR** and **5**) or the corresponding sulfonyl derivatives (**3** and **6**), the LUMO is localized over the electron-withdrawing pyrimidine unit with low extension to tCbz, being very similar to the LUMO distribution for pyrimidine derivative **1** without a substituent at the position 2 of the pyrimidine ring. The π-electron density distribution in the LUMO of compounds bearing a phenyl (**2a**), *para/meta*-cyanophenyl, and *meta*-bromophenyl moiety (**2b**–**d**) at position 2 of the pyrimidine ring tends to localize over the pyrimidine ring and nearby phenyl groups, resulting in a lower HOMO–LUMO overlap. A similar LUMO localization is observed for compound **4** with a 2-cyano group.

The energies of the HOMO level were in the range from −5.50 eV to −5.70 eV with lower values for those compounds bearing electron-withdrawing groups (Table 1). The LUMO energies varied from −1,38 eV for compound **5** with a phenylthio group to −2.15 eV for compound **2b** bearing a *p*-cyanophenyl group in position 2 of the pyrimidine ring. The $S_0 \rightarrow S_1$ transition energies ranged from 3–3.4 eV with lower values for the CN/Br/phenyl-substituted compounds due to the larger conjugation length of the acceptor unit (also evidenced by a deeper LUMO), followed by lower oscillator strengths of $S_0 \rightarrow S_1$ transition due to more evident HOMO–LUMO decoupling (≈0.04 vs ≈0.4). Lower singlet–triplet energy gaps were estimated for compounds with stronger acceptor units (down to 200 meV), beneficial for efficient thermal triplet upconversion.

Absorption and emission properties

Absorption (10^{-5} M toluene solutions) and emission spectra (1 wt % PMMA films) of the carbazole–pyrimidine TADF compounds are shown in Figure 3 and details are enclosed in Table 2. The absorption spectra were rather similar for all compounds, described with, typical for tCbz units, vibronic progression-having peaks bellow ≈340 nm [41]. Molar absorption coefficients were in the range of 19700–34200 M^{-1} cm^{-1}, being in line with DFT predicted $S_0 \rightarrow S_1$ oscillator strengths and LUMO energies. The fluorescence spectra, on the other hand, showed much larger differences upon the modification of the acceptor unit. In this case, the emission wavelength was tuned in the range of 480 meV, starting from 411 nm (compounds **1** and **2a**) to 468 nm (compound **2b**). Such trend was in line with the increase of the strength of the acceptor unit, namely the energy of the LUMO (see Table 1 and Figure S28 in Supporting Information File 1), while the lower emission energy was observed for compounds with more pronounced charge-transfer (CT) character. This was also evidenced by larger FWHM values of fluorescence spectra for compounds with stronger CT emission (e.g., compounds **1** and **4**). The phosphorescence (PH) spectra of the carbazole–pyrimidine TADF compounds were rather intriguing. 10 K PH spectra of compounds **tCbz-mPYR**, **1**, **3**, **5**, and **6** clearly resembled that of individual tCbz units, peaking at about 418 nm [29], while for the rest of the compounds the PH spectra were red-shifted, though still maintaining the vibronic structure. However, the closer inspection of the PH spectra, see Figure S29 in Supporting Information File 1, revealed that all PH spectra coincided with that of the tCbz unit. Actually, the lowest-energy 0–0' vibronic peak was of very low intensity for compounds **2a**–**d** or **4** as well as the intensity ratio of high-energy replicas was also different, though the T_1 energy was the same for all carbazole–pyrimidine compounds. The compounds **2a**–**d** and **4** have one common feature, namely, their acceptor unit is modified with various phenyl-like fragments, increasing the flexibility of the molecular structure, probably altering the electron–vibronic coupling. A similar behavior was observed

Table 1: DFT computed $S_0 \rightarrow S_1/T_1$ transition energies, oscillator strengths of $S_0 \rightarrow S_1$ transitions, and ΔE_{ST} values of carbazole–pyrimidine TADF compounds.

Compd.	$f_{S0 \rightarrow S1}$[a]	$E_{S0 \rightarrow S1}$ (eV)[b]	$E_{S0 \rightarrow T1}$ (eV)[c]	ΔE_{S1T1} (meV)[d]	HOMO (eV)[e]	LUMO (eV)[f]
tCbz-mPYR	0.3940	3.4265	3.1380	289	–5.53	–1.42
1	0.3999	3.4508	3.1400	311	–5.53	–1.39
2a	0.0383	3.4094	2.9911	418	–5.51	–1.52
2b	0.0360	2.9562	2.7535	203	–5.61	–2.15
2c	0.0473	3.1616	2.9003	261	–5.57	–1.89
2d	0.0465	3.2820	2.9518	330	–5.55	–1.71
3	0.3959	3.2132	2.9251	288	–5.66	–1.79
4	0.0496	3.0245	2.7858	239	–5.70	–2.09
5	0.4100	3.4377	3.1390	299	–5.50	–1.38
6	0.3779	3.2706	2.9864	284	–5.63	–1.71

[a]$S_0 \rightarrow S_1$ transition oscillator strength; [b]$S_0 \rightarrow S_1$ transition energies; [c]$S_0 \rightarrow T_1$ transition energies; [d]singlet–triplet energy gap; [e]HOMO energies; [f]LUMO energies.

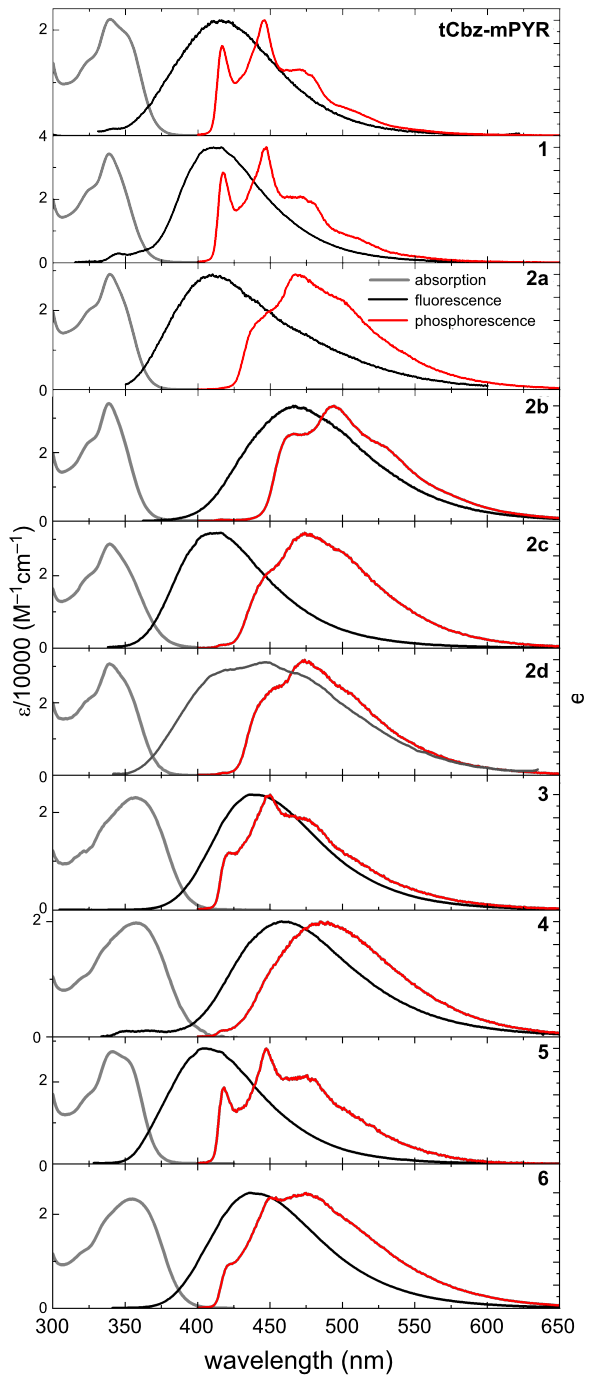

Figure 3: Absorption (grey lines), fluorescence (black lines) and 10K phosphorescence (red lines) spectra of carbazole–pyrimidine TADF compounds. 10^{-5} M toluene solutions were used for absorption measurements, while 1 wt % PMMA films were used for emission measurements.

for similar pyrimidine TADF compounds [42]. Moreover, fluorescence line shapes of compounds **2a** and **2d** were different from the rest of compounds with low-energy shoulder. More detailed analysis (see Figure S30 in Supporting Information File 1) revealed the presence of room-temperature phosphorescence (RTP), perturbing the lineshape of PL spectra. The estimated singlet–triplet energy gaps (ΔE_{ST}) of carbazole–pyrimidine TADF compounds were in the range of 159–530 meV, systematically decreasing for compounds with stronger acceptor unit (see Figure S28d in Supporting Information File 1). ΔE_{ST} was large for the majority of compounds, however, for compounds **2b, 3**, **4**, and **6** modified with CN and SO_2CH_3 groups ΔE_{ST} was as low as 159 meV, promising for efficient thermally activated triplet upconversion.

Fluorescence decay transients of 1 wt % PMMA films of carbazole–pyrimidine TADF compounds are shown in Figure 4. Typical for TADF compounds temporal profiles having two decay regimes were observed when the initial decay was of prompt fluorescence and the latter one was of TADF. The PF decay rate (1–4 × 10^8 s^{-1}) was typical for directly bound carbazole–pyrimidine TADF compounds [43,44], though a somewhat lower value was estimated for compound **3** modified with a methylsulfonyl group. More insights could be drawn by analyzing the fluorescence quantum yield (Φ_F) as well as radiative (k_r) and non-radiative (k_{nr}) fluorescence decay rates (see Table 2). The Φ_{PF} was typical for carbazole–pyrimidine TADF compounds [31,43,44], in the range of 0.01–0.07 and decreased for compounds with stronger acceptor units (see Figure S28b in Supporting Information File 1). The radiative decay rate was in the range of 1.3–13.0 × 10^6 s^{-1}. Typically, k_r was larger for compounds with weaker acceptor units and a lower CT fluorescence strength (see Figure S28c in Supporting Information File 1). In case of k_{nr}, a similar analysis is hardly possible, as k_{nr} accounts for two different rates, namely internal conversion to S_0 and intersystem crossing. However, some faint trends could be seen, as compounds with the strongest donor units tend to have the larger k_{nr} (compounds **2b**–**d**).

In case of delayed fluorescence, more complicated fluorescence temporal profiles were observed, aggravating its analysis. DF decay transients were perturbed by conformational disorder, typical for D–A TADF compounds in solid films [41,45-47]. The presence of conformational disorder made exponential fitting of DF transients hardly possible due to the multiexponential temporal profiles of the DF decay. Unfortunately, TADF decay rates were inaccessible. Similar emission decay transients were also estimated for RTP compounds **2a** and **2d** both at singlet and triplet emission peaks (see Figure S31 in Supporting Information File 1). The largest DF quantum yield, ranging from 0.34–0.49, was estimated for compounds **tCbz-mPYR**, **3**, and **4** with the lowest ΔE_{ST}, modified with CN, SCH_3, and SO_2CH_3 functional groups directly at the pyrimidine unit. The introduction of phenyl substituents (compounds **2a**–**d**) or S-aryl units (compounds **5** and **6**) at position 2 of the pyrimidine ring

Table 2: Fluorescence parameters of carbazole–pyrimidine TADF compounds.

Compd.	λ_{abs} (nm)[a]	ε ($M^{-1}cm^{-1}$)[b]	λ_{PL} (nm)[c]	Φ_{PF}[d]	Φ_{DF}[e]	k_{PF} ($\times10^8$ s)[f]	k_r ($\times10^6$ s)[g]	k_{nr} ($\times10^8$ s)[h]	Φ_{DF}/Φ_{PF}[i]	ΔE_{ST} (meV)[j]
tCbz-mPYR	339	22000	415	0.05	0.40	2.5	13.0	2.4	8.0	530
1	339	33420	411	0.07	0.11	1.4	9.3	1.3	1.6	397
2a	339	29100	411	0.03	0.06	2.1	6.8	2.0	2.0	510
2b	339	34200	468	0.01	0.24	3.1	3.0	3.1	24.0	128
2c	339	28700	410	0.01	0.18	3.0	3.7	3.0	18.0	443
2d	339	30700	447	0.01	0.05	4.2	2.4	4.1	5.0	501
3	357	23000	440	0.06	0.49	0.7	4.0	0.6	8.2	265
4	358	19700	460	0.01	0.34	1.1	1.3	1.0	34.0	159
5	341	27400	408	0.03	0.05	3.0	8.2	2.9	1.7	530
6	355	23000	441	0.04	0.02	1.2	5.1	1.1	0.5	273

[a]Absorption peak in toluene; [b]molar absorption coefficient in toluene; [c]fluorescence peak in 1 wt % PMMA; [d]prompt fluorescence quantum yield 1 wt % PMMA; [e]delayed fluorescence quantum yield 1 wt % PMMA; [f]fluorescence decay rates 1 wt % PMMA; [g]radiative decay rates 1 wt % PMMA; [h]nonradiative decay rates 1 wt % PMMA; [i]prompt and delayed fluorescence quantum yield ratio 1 wt % PMMA; [j]singlet–triplet energy gap 1 wt % PMMA.

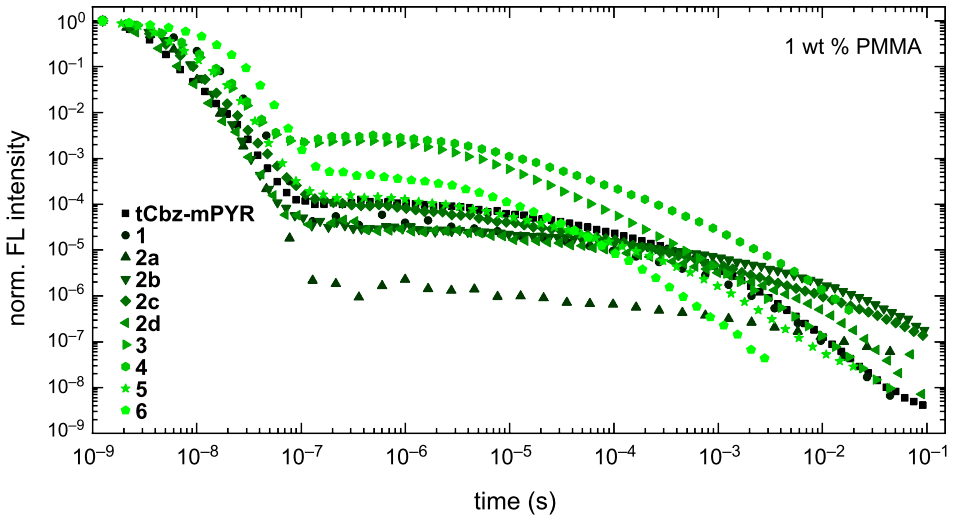

Figure 4: Fluorescence decay transients of 1 wt % PMMA films of carbazole–pyrimidine TADF compounds in oxygen-free conditions.

led to lower Φ_{DF}, probably due to the enlarged nonradiative decay rate. Interestingly, ΔE_{ST} was remarkably larger for **tCbz-mPYR** despite its high Φ_{DF}. In this case, rISC probably was promoted by efficient triplet upconversion through spin-vibronicaly bound T_n energy levels [48].

Conclusion

In summary, a series of novel pyrimidine–carbazole TADF emitters bearing different substituents in position 2 of the pyrimidine moiety were successfully prepared by using Liebeskind–Srogl cross-coupling, hydrogenolysis, oxidation reactions of 4,6-bis(3,6-di-*tert*-butyl-9-carbazolyl)-5-methyl-2-methylthiopyrimidine and following nucleophilic substitution of the methylsulfonyl group with sodium cyanide and 4-(*tert*-butyl)thiophenol. The thorough photophysical analysis was carried out to assess the impact of different substituents in position 2 of the pyrimidine ring. It was shown that HOMO–LUMO overlap and the resulting ΔE_{ST} can be easily minimized, enabling rather efficient TADF. We have shown that electron-withdrawing substituents connected directly to the pyrimidine unit have a larger impact on TADF efficiency in comparison with those attached through a phenylene bridge. The largest delayed fluorescence quantum yield, ranging from 0.34–0.49, was estimated for compounds with CN, SCH_3, and SO_2CH_3 functional groups at the position 2 of the pyrimidine unit. We believe that our findings on the TADF properties of

differently substituted carbazole–pyrimidines will be useful for molecular design of high-performance TADF emitters in the future.

Experimental

General information

Reagents and solvents were purchased directly from commercial suppliers and solvents were purified by known procedures. Melting points were determined in open capillaries with a digital melting point IA9100 series apparatus (ThermoFischer Scientific) and were not corrected. Thin-layer chromatography was performed using TLC aluminum sheets with silica gel (Merck 60 F254). Visualization was accomplished by UV light. Column chromatography was performed using silica gel 60 (0.040–0.063 mm, Merck). NMR spectra were recorded on a Bruker Ascend 400 (400 MHz and 100 MHz for ^{1}H and ^{13}C, respectively). ^{1}H NMR and ^{13}C NMR spectra were referenced to residual solvent peaks. High-resolution mass spectrometry (HRMS) analyses were carried out on a Dual-ESI Q-TOF 6520 (Agilent Technologies) mass spectrometer.

Photophysical properties were analyzed in 10^{-5} M toluene solutions as well as 1 wt % PMMA (poly(methyl methacrylate)) films. The solid-state samples were prepared by dissolving the compounds and polymer or host material at appropriate ratios in toluene solution and then wet-casting the solutions on quartz substrates. The absorption spectra were recorded by a Lambda 950 UV–vis–NIR spectrometer (Perkin Elmer). The fluorescence quantum yields (Φ_F) in ambient air were estimated by the integrating sphere method [49] in integrating sphere (Sphere Optics) coupled to a CCD spectrometer PMA-12 (Hamamatsu) via optical fibers excited with a CW xenon lamp. Φ_{PF} and Φ_{DF} values were estimated according to [50]. Time-integrated fluorescence, phosphorescence spectra as well as fluorescence decay kinetics were recorded with a time-gated intensified iCCD camera iStar DH340T (Andor) with a spectrograph SR-303i (Shamrock) coupled with nanosecond YAG:Nd^{3+} laser NT 242 with an optical parametric generator (Ekspla, pulse width 7 ns, 1 kHz frequency, 100 nJ pulse energy). Fluorescence decay transients were obtained by exponentially increasing the delay and integration time [51]. Phosphorescence spectra were recorded at 10 K temperature after a 100 μs delay with a 49 ms integration time. Solid-state samples were mounted in a closed cycle He cryostat (Cryo Industries 204 N) for PL measurements in oxygen-free conditions.

Quantum chemical calculations were carried out by using density functional theory at the B3LYP/6-31G(d) level as implemented in a software package Gaussian 09 [52]. The solvation behaviour of the surrounding toluene was estimated by the polarizable continuum model. Although the B3LYP/6-31G(d) theory level due to the neglected long-range exchange interaction can give less accurate results for calculated molecular geometries and transition energies [53], however, it should be sufficient for brief analysis.

Procedures and product characterization

4,6-Bis[3,6-di(*tert*-butyl)-9*H*-carbazol-9-yl]-5-methylpyrimidine (1). Compound **1** was synthesized in a manner similar to [30]. A mixture of compound **tCbz-mPYR** (90 mg, 0.13 mmol, 1 equiv), Raney nickel (270 mg, 3 equiv by mass), prepared before reaction according to [54], and methanol (3 mL) were placed in a screw-cap vial equipped with a magnetic stirring bar. The reaction mixture was heated at 90 °C under stirring for 2 h. Then, Raney nickel was filtered off and washed with hot chloroform. The filtrate was concentrated and the obtained residue was purified by column chromatography using chloroform/petroleum ether 2:1 to pure chloroform as an eluent to give 13.5 mg (16%) of compound **1**. Mp > 300 °C (from 2-propanol); ^{1}H NMR (400 MHz, $CDCl_3$) δ 1.52 (s, 36H, $(CH_3)_3C$), 2.01 (s, 3H, CH_3), 7.48 (d, J = 8 Hz, 4H, CH_{Cbz}), 7.62 (d, J = 8 Hz, 4H, CH_{Cbz}), 8.18 (s, 4H, CH_{Cbz}), 9.23 (s, 1H, CH_{py}) ppm; ^{13}C NMR (100 MHz, $CDCl_3$) δ 15.2, 31.9, 34.9, 110.7, 116.6, 121.8, 124.2, 124.7, 137.8, 144.6, 157.1, 160.2 ppm; HRMS–ESI (*m/z*): $[M + H]^+$ calcd for $C_{45}H_{53}N_4$, 649.4265; found, 649.4265.

2-Aryl-4,6-bis[3,6-di(*tert*-butyl)-9*H*-carbazol-9-yl]-5-methylpyrimidines **2a–d**

General procedure. 4,6-Bis(3,6-di-*tert*-butyl-carbazol-9-yl)-5-methyl-2-methylthiopyrimidine (50 mg, 0.072 mmol), the corresponding boronic acid (0.094 mmol), CuMeSal (34 mg, 0.158 mmol), $Pd(PPh_3)_4$ (4.2 mg, 0.0036 mmol), Cs_2CO_3 (46.8 mg, 0.144 mmol, in case of *meta*-substituted boronic acid, 1 equiv) and dioxane (3 mL) were placed in a screw-cap vial equipped with a magnetic stirring bar and flushed with argon for 10 min. The reaction mixture was heated at 130 °C under stirring for 4 h. Then, dioxane was removed by distillation under reduced pressure, water (40 mL) was added to the residue, and the mixture was extracted with chloroform (3 × 25 mL). The combined extracts were washed with brine, dried with anhydrous Na_2SO_4, filtered, and chloroform was removed by distillation under reduced pressure. The residue was purified by column chromatography using chloroform/petroleum ether (1:1 for compound **2a**; 1:2 for compounds **2b**, **2c**; 1:4 for compound **2d**) as an eluent to give the corresponding product.

4,6-Bis[3,6-di(*tert*-butyl)-9*H*-carbazol-9-yl]-5-methyl-2-phenylpyrimidine (2a). Yield 48%; mp > 320 °C (from 2-propanol); ^{1}H NMR (400 MHz, $CDCl_3$) δ 1.54 (s, 36H, $(CH_3)_3C$), 1.96 (s, 3H, CH_3), 7.52–7.59 (m, 7H, ArH, CH_{Cbz})

7.61–7.66 (m, 4H, CH_{Cbz}), 8.20 (s, 4H, CH_{Cbz}), 8.58–8.63 (m, 2H, ArH) ppm; ^{13}C NMR (100 MHz, $CDCl_3$) δ 15.2, 32.0, 34.86; 111.0, 116.5, 118.4, 124.0, 124.6, 128.4, 128.7, 131.1, 136.9, 137.9, 144.4, 160.2, 163.0 ppm; HRMS–ESI (*m/z*): $[M + H]^+$ calcd for $C_{51}H_{57}N_4$, 725.4578; found, 725.4576.

4,6-Bis[3,6-di(*tert*-butyl)-9*H*-carbazol-9-yl]-2-(4-cyanophenyl)-5-methylpyrimidine (2b). Yield 35%; mp 266–270 °C (from 2-propanol); ^{1}H NMR (400 MHz, $CDCl_3$) δ 1.54 (s, 36H, $(CH_3)_3C$), 2.00 (s, 3H, CH_3), 7.54 (d, ^3J = 8.61 Hz, 4H, CH_{Cbz}), 7.64 (dd, ^3J = 8.61 Hz, ^4J = 1.69 Hz, 4H, CH_{Cbz}), 7.82 (d, ^3J = 8.35 Hz, 2H, ArH), 8.21 (d, ^4J = 1.61 Hz, 4H, CH_{Cbz}), 8.70 (d, ^3J = 8.35 Hz, 2H, ArH) ppm; ^{13}C NMR (100 MHz, $CDCl_3$) δ 15.4, 32.0, 34.9, 110.9, 114.3, 116.7, 118.9, 119.7, 124.1, 124.7, 128.8, 132.6, 137.7, 140.9, 144.7, 160.5 ppm; HRMS–ESI (*m/z*): $[M + H]^+$ calcd for $C_{52}H_{56}N_5$), 750.4530; found, 750.4534.

4,6-Bis[3,6-di(*tert*-butyl)-9*H*-carbazol-9-yl]-2-(3-cyanophenyl)-5-methylpyrimidine (2c). Yield 19%; mp 233–236 °C (from 2-propanol); ^{1}H NMR (400 MHz, $CDCl_3$) δ 1.44 (s, 36H, $(CH_3)_3C$), 1.89 (s, 3H; CH_3), 7.43 (d, ^3J = 8.63 Hz, 4H, CH_{Cbz}), 7.52–7.56 (m, 5H, CH_{Cbz}, ArH), 7.71 (d, ^3J = 7.7 Hz, 1H, ArH), 8.10 (d, ^4J = 1.68 Hz, 4H, CH_{Cbz}), 8.72 (d, ^3J = 8.0 Hz, 1H, ArH), 8.77 (s, 1H, ArH) ppm; ^{13}C NMR (100 MHz, $CDCl_3$) δ 15.4, 32.0, 34.9, 110.8, 113.0, 116.7, 118.7, 119.7, 124.2, 124.7, 129.6, 131.9, 132.5, 134.2, 137.7, 138.1, 144.7, 160.5, 160.8 ppm; HRMS–ESI (*m/z*): $[M + H]^+$ calcd for $C_{52}H_{56}N_5$, 750.4530; found, 750.4524.

4,6-Bis[3,6-di(*tert*-butyl)-9*H*-carbazol-9-yl]-2-(3-bromophenyl)-5-methylpyrimidine (2d). Yield 55%; mp > 250 °C; ^{1}H NMR (400 MHz, $CDCl_3$) δ 1.54 (s, 36H, $(CH_3)_3C$), 1.95 (s, 3H, CH_3), 7.40 (t, ^3J = 7.88 Hz, 1H, ArH), 7.53 (d, ^3J = 8.6 Hz, 4H, CH_{Cbz}), 7.63 (dd, ^3J = 8.68 Hz, ^4J = 1.92 Hz, 4H, CH_{Cbz}), 7.67 (m, 1H, ArH), 8.20 (d, ^4J = 1.64 Hz, 4H, CH_{Cbz}), 8.53 (dt, ^3J = 8.0 Hz, ^4J = 1.24 Hz, 1H, ArH), 8.72 (t, ^4J = 1.72 Hz, 1H, ArH) ppm; ^{13}C NMR (100 MHz, $CDCl_3$) δ 15.2, 32.0, 34.9, 110.9, 116.6, 119.2, 123.0, 124.1, 124.6, 127.0, 130.3, 131.2, 134.0, 137.8, 139.0, 144.5, 160.4, 161.7 ppm; HRMS–ESI (*m/z*): $[M + H]^+$ calcd for $C_{51}H_{56}BrN_4$, 803.3683; found, 803.3675.

4,6-Bis(3,6-di-*tert*-butyl-9*H*-carbazol-9-yl)-5-methyl-2-methylsulfonylpyrimidine (3). A mixture of compound **tCbz-mPYR** (60 mg, 0.086 mmol), oxone (133.2 mg, 0.217 mmol, 2.5 equiv by active component), and DMF (3 mL) were stirred at 80 °C for 3 h. After completion of the reaction, water (40 mL) was added to reaction mixture and the aqueous solution was extracted with chloroform (3 × 25 mL). The combined extract was washed with brine twice, dried with anhydrous Na_2SO_4, filtered, and chloroform was removed by distillation under reduced pressure. The residue was purified by column chromatography using chloroform/petroleum ether 2:1 as an eluent to give 58 mg (92%) of compound **3**. Mp > 350 °C (from 2-propanol); ^{1}H NMR (400 MHz, $CDCl_3$) δ 1.52 (s, 36H, $(CH_3)_3C$), 2.03 (s, 3H, CH_3), 3.45 (s, 3H, CH_3SO_2), 7.54 (d, *J* = 8.65 Hz, 4H, CH), 7.64 (dd, *J* = 8.67 Hz, *J* = 1.89 Hz, 4H, CH), 8.15 (d, J = 1.68 Hz, 4H, CH) ppm; ^{13}C NMR (100 MHz, $CDCl_3$) δ 16.5, 31.9, 34.9, 39.4, 111.2, 116.7, 122.6, 124.4, 125.2, 137.3, 145.6, 160.8, 162.5, 163.8 ppm; HRMS–ESI (*m/z*): $[M + H]^+$ calcd for $C_{46}H_{55}N_4O_2S$, 727.4040; found, 727.4034.

4,6-Bis(3,6-di-*tert*-butyl-9*H*-carbazol-9-yl)-5-methylpyrimidine-2-carbonitrile (4). A mixture of compound **3** (50 mg, 0.069 mmol), NaCN (7.4 mg, 0.151 mmol), and THF (2 mL) was refluxed under stirring for 3.5 h. After completion of the reaction, THF was removed by distillation under reduced pressure, water (30 mL) was added to the residue, and the aqueous solution was extracted with chloroform (3 × 25 mL). The combined extract was washed with brine, dried with anhydrous Na_2SO_4, filtered, and chloroform was removed by distillation under reduced pressure. The residue was purified by column chromatography using chloroform/petroleum ether 1:2 as an eluent to give 30 mg (65%) of compound **4**. Mp > 320 °C (from 2-propanol); ^{1}H NMR (400 MHz, $CDCl_3$) δ 1.43 (s, 36H, $(CH_3)_3C$), 1.92 (s, 3H, CH_3), 7.40 (d, ^3J = 8.63 Hz, 4H, CH_{Cbz}), 7.55 (dd, ^3J = 8.66 Hz, ^4J = 1.93 Hz, 4H, CH_{Cbz}), 8.07 (d, ^4J = 1.67 Hz, 4H, CH_{Cbz}) ppm; ^{13}C NMR (100 MHz, $CDCl_3$) δ 16.4, 31.9, 34.9, 111.0, 115.4, 116.8, 123.8, 124.3, 125.1, 137.2, 142.4, 145.6, 160.7 ppm; HRMS–ESI (*m/z*): $[M + H]^+$ calcd for $C_{46}H_{52}N_5$, 674.4217; found, 674,4213.

4,6-Bis[3,6-di(*tert*-butyl)-9*H*-carbazol-9-yl]-2-[4-(*tert*-butyl)phenylthio]-5-methylpyrimidine (5). A mixture of compound **3** (40 mg, 0.055 mmol), 4-(*tert*-butyl)thiophenol (10.4 µL, 0.061 mmol), NEt_3 (8.4 µL, 0.061 mmol), and THF (2 mL) were placed in a screw-cap vial equipped with a magnetic stirring bar and flushed with argon for 10 min. The reaction mixture was stirred at 50 °C overnight. Then, THF was removed by distillation under reduced pressure, water (30 mL) was added to residue, and the aqueous solution was extracted with chloroform (3 × 25 mL). The combined extract was washed with brine, dried with anhydrous Na_2SO_4, filtered, and chloroform was removed by distillation under reduced pressure. The residue was purified by column chromatography using chloroform/petroleum ether 1:2 as an eluent to give 35 mg (77%) of compound **5**. Mp 214–217 °C (from 2-propanol); ^{1}H NMR (400 MHz, $CDCl_3$) δ 1.19 (s, 9H, $(CH_3)_3C_{benz}$), 1.37 (s, 36H, $(CH_3)_3C_{Cbz}$), 1.69 (s, 3H, CH_3), 7.28–7.35 (m, 6H, ArH, CH_{Cbz}), 7.44 (dd, ^3J = 8.65 Hz, ^4J = 1.66 Hz, 4H, CH_{Cbz}),

7.60 (d, ^3J = 8.27 Hz, 2H, ArH), 8.00 (d, ^4J = 1.39 Hz, 4H, CH_{Cbz}) ppm; ^{13}C NMR (100 MHz, $CDCl_3$) δ 15.3, 31.3, 32.0, 34.7, 34.8, 111.4, 114.8, 116.3, 123.8, 124.6, 125.6, 126.2, 135.7, 137.6, 144.5, 152.6, 159.9, 170.9 ppm; HRMS–ESI (*m/z*): $[M + H]^+$ calcd for $C_{55}H_{65}N_4S$, 813.4924; found, 813.4919.

4,6-Bis[3,6-di(*tert*-butyl)-9*H*-carbazol-9-yl]-2-[4-(*tert*-butyl)phenylsulfonyl]-5-methylpyrimidine (6). Compound **6** was synthesized from compound **5** according to the procedure described for compound **3**. Yield 68%, mp 275–278 °C (from 2-propanol); ^1H NMR (400 MHz, $CDCl_3$) δ 1.38 (s, 9H, $(CH_3)_3C_{benz}$), 1.51 (s, 36H, $(CH_3)_3C_{Cbz}$), 1.91 (s, 3H, CH_3), 7.43 (d, ^3J = 8.66 Hz, 4H, CH_{Cbz}), 7.56–7.65 (m, 6H, ArH, CH_{Cbz}), 8.13 (d, ^4J = 1.69 Hz, 4H, CH_{Cbz}), 8.17 (m, 2H, ArH) ppm; ^{13}C NMR (100 MHz, $CDCl_3$) δ 16.6, 31.1, 31.9, 34.9, 35.4, 111.4, 116.6, 121.3, 124.2, 125.1, 126.2, 129.9, 134.5, 137.3, 145.4, 158.2, 160.5, 164.5 ppm; HRMS–ESI (*m/z*): $[M + H]^+$ calcd for $C_{55}H_{65}N_4O_2S$, 845.4823; found, 845.4812.

Supporting Information

Supporting Information File 1

Copies of NMR spectra and extended photophysical properties.
[https://www.beilstein-journals.org/bjoc/content/supplementary/1860-5397-18-52-S1.pdf]

ORCID® iDs

Tomas Serevičius - https://orcid.org/0000-0003-1319-7669
Sigitas Tumkevicius - https://orcid.org/0000-0002-3279-1770

References

1. Uoyama, H.; Goushi, K.; Shizu, K.; Nomura, H.; Adachi, C. *Nature* **2012,** *492,* 234–238. doi:10.1038/nature11687
2. Endo, A.; Sato, K.; Yoshimura, K.; Kai, T.; Kawada, A.; Miyazaki, H.; Adachi, C. *Appl. Phys. Lett.* **2011,** *98,* 083302. doi:10.1063/1.3558906
3. Xie, F.-M.; Zhou, J.-X.; Li, Y.-Q.; Tang, J.-X. *J. Mater. Chem. C* **2020,** *8,* 9476–9494. doi:10.1039/d0tc02252g
4. Wong, M. Y.; Zysman-Colman, E. *Adv. Mater. (Weinheim, Ger.)* **2017,** *29,* 1605444. doi:10.1002/adma.201605444
5. Dias, F. B.; Penfold, T. J.; Monkman, A. P. *Methods Appl. Fluoresc.* **2017,** *5,* 012001. doi:10.1088/2050-6120/aa537e
6. Tao, Y.; Yuan, K.; Chen, T.; Xu, P.; Li, H.; Chen, R.; Zheng, C.; Zhang, L.; Huang, W. *Adv. Mater. (Weinheim, Ger.)* **2014,** *26,* 7931–7958. doi:10.1002/adma.201402532
7. Yang, Z.; Mao, Z.; Xie, Z.; Zhang, Y.; Liu, S.; Zhao, J.; Xu, J.; Chi, Z.; Aldred, M. P. *Chem. Soc. Rev.* **2017,** *46,* 915–1016. doi:10.1039/c6cs00368k
8. Cai, X.; Su, S.-J. *Adv. Funct. Mater.* **2018,** *28,* 1802558. doi:10.1002/adfm.201802558
9. Komatsu, R.; Sasabe, H.; Kido, J. *J. Photonics Energy* **2018,** *8,* 032108. doi:10.1117/1.jpe.8.032108
10. Lee, C. H.; Choi, S. H.; Oh, S. J.; Lee, J. H.; Shim, J. W.; Adachi, C.; Lee, S. Y. *RSC Adv.* **2020,** *10,* 42897–42902. doi:10.1039/d0ra07865d
11. Yu, L.; Yang, C. *J. Mater. Chem. C* **2021,** *9,* 17265–17286. doi:10.1039/d1tc04397h
12. Lin, L.-Y.; Tsai, C.-H.; Wong, K.-T.; Huang, T.-W.; Wu, C.-C.; Chou, S.-H.; Lin, F.; Chen, S.-H.; Tsai, A.-I. *J. Mater. Chem.* **2011,** *21,* 5950–5958. doi:10.1039/c1jm10201j
13. Chiu, S.-W.; Lin, L.-Y.; Lin, H.-W.; Chen, Y.-H.; Huang, Z.-Y.; Lin, Y.-T.; Lin, F.; Liu, Y.-H.; Wong, K.-T. *Chem. Commun.* **2012,** *48,* 1857–1859. doi:10.1039/c2cc16390j
14. Wu, C.-H.; Pan, T.-Y.; Hong, S.-H.; Wang, C.-L.; Kuo, H.-H.; Chu, Y.-Y.; Diau, E. W.-G.; Lin, C.-Y. *Chem. Commun.* **2012,** *48,* 4329–4331. doi:10.1039/c2cc30892d
15. Ortiz, R. P.; Casado, J.; Hernández, V.; López Navarrete, J. T.; Letizia, J. A.; Ratner, M. A.; Facchetti, A.; Marks, T. J. *Chem. – Eur. J.* **2009,** *15,* 5023–5039. doi:10.1002/chem.200802424
16. Irfan, A.; Al-Sehemi, A. G.; Al-Assiri, M. S. *J. Mol. Graphics Modell.* **2013,** *44,* 168–176. doi:10.1016/j.jmgm.2013.06.003
17. Kojima, T.; Nishida, J.-i.; Tokito, S.; Yamashita, Y. *Chem. Lett.* **2009,** *38,* 428–429. doi:10.1246/cl.2009.428
18. Achelle, S.; Nouira, I.; Pfaffinger, B.; Ramondenc, Y.; Plé, N.; Rodríguez-López, J. *J. Org. Chem.* **2009,** *74,* 3711–3717. doi:10.1021/jo900107u
19. Cvejn, D.; Achelle, S.; Pytela, O.; Malval, J.-P.; Spangenberg, A.; Cabon, N.; Bureš, F.; Robin-le Guen, F. *Dyes Pigm.* **2016,** *124,* 101–109. doi:10.1016/j.dyepig.2015.09.012
20. Tang, R.; Wang, X.; Zhang, W.; Zhuang, X.; Bi, S.; Zhang, W.; Zhang, F. *J. Mater. Chem. C* **2016,** *4,* 7640–7648. doi:10.1039/c6tc02591a
21. Achelle, S.; Rodríguez-López, J.; Bureš, F.; Robin-le Guen, F. *Chem. Rec.* **2020,** *20,* 440–451. doi:10.1002/tcr.201900064
22. Verbitskiy, E. V.; Dinastiya, E. M.; Baranova, A. A.; Khokhlov, K. O.; Chuvashov, R. D.; Yakovleva, Y. A.; Makarova, N. I.; Vetrova, E. V.; Metelitsa, A. V.; Slepukhin, P. A.; Rusinov, G. L.; Chupakhin, O. N.; Charushin, V. N. *Dyes Pigm.* **2018,** *159,* 35–44. doi:10.1016/j.dyepig.2018.05.075
23. Boländer, A.; Kieser, D.; Voss, C.; Bauer, S.; Schön, C.; Burgold, S.; Bittner, T.; Hölzer, J.; Heyny-von Haußen, R.; Mall, G.; Goetschy, V.; Czech, C.; Knust, H.; Berger, R.; Herms, J.; Hilger, I.; Schmidt, B. *J. Med. Chem.* **2012,** *55,* 9170–9180. doi:10.1021/jm300653b
24. Achelle, S.; Hodée, M.; Massue, J.; Fihey, A.; Katan, C. *Dyes Pigm.* **2022,** *200,* 110157. doi:10.1016/j.dyepig.2022.110157
25. Komatsu, R.; Sasabe, H.; Seino, Y.; Nakao, K.; Kido, J. *J. Mater. Chem. C* **2016,** *4,* 2274–2278. doi:10.1039/c5tc04057d
26. Xiang, Y.; Zhao, Y.; Xu, N.; Gong, S.; Ni, F.; Wu, K.; Luo, J.; Xie, G.; Lu, Z.-H.; Yang, C. *J. Mater. Chem. C* **2017,** *5,* 12204–12210. doi:10.1039/c7tc04181k
27. Xiang, Y.; Li, P.; Gong, S.; Huang, Y.-H.; Wang, C.-Y.; Zhong, C.; Zeng, W.; Chen, Z.; Lee, W.-K.; Yin, X.; Wu, C.-C.; Yang, C. *Sci. Adv.* **2020,** *6,* eaba7855. doi:10.1126/sciadv.aba7855
28. Komatsu, R.; Ohsawa, T.; Sasabe, H.; Nakao, K.; Hayasaka, Y.; Kido, J. *ACS Appl. Mater. Interfaces* **2017,** *9,* 4742–4749. doi:10.1021/acsami.6b13482
29. Serevičius, T.; Skaisgiris, R.; Fiodorova, I.; Steckis, V.; Dodonova, J.; Banevičius, D.; Kazlauskas, K.; Juršėnas, S.; Tumkevičius, S. *Org. Electron.* **2020,** *82,* 105723. doi:10.1016/j.orgel.2020.105723

30. Serevičius, T.; Skaisgiris, R.; Fiodorova, I.; Kreiza, G.; Banevičius, D.; Kazlauskas, K.; Tumkevičius, S.; Juršėnas, S. *J. Mater. Chem. C* **2021,** *9,* 836–841. doi:10.1039/d0tc05503d
31. Tsiko, U.; Bezvikonnyi, O.; Sych, G.; Keruckienė, R.; Volyniuk, D.; Simokaitienė, J.; Danyliv, I.; Danyliv, Y.; Bučinskas, A.; Tan, X.; Gražulevičius, J. V. *J. Adv. Res.* **2021,** *33,* 41–51. doi:10.1016/j.jare.2021.01.014
32. Li, S.-W.; Yu, C.-H.; Ko, C.-L.; Chatterjee, T.; Hung, W.-Y.; Wong, K.-T. *ACS Appl. Mater. Interfaces* **2018,** *10,* 12930–12936. doi:10.1021/acsami.8b02766
33. Rodella, F.; Saxena, R.; Bagnich, S.; Banevičius, D.; Kreiza, G.; Athanasopoulos, S.; Juršėnas, S.; Kazlauskas, K.; Köhler, A.; Strohriegl, P. *J. Mater. Chem. C* **2021,** *9,* 17471–17482. doi:10.1039/d1tc03598c
34. Itami, K.; Yamazaki, D.; Yoshida, J.-i. *J. Am. Chem. Soc.* **2004,** *126,* 15396–15397. doi:10.1021/ja044923w
35. Maddess, M. L.; Carter, R. *Synthesis* **2012,** *44,* 1109–1118. doi:10.1055/s-0031-1289744
36. Urbonas, R. V.; Poskus, V.; Bucevicius, J.; Dodonova, J.; Tumkevicius, S. *Synlett* **2013,** *24,* 1383–1386. doi:10.1055/s-0033-1338951
37. Kusturin, C.; Liebeskind, L. S.; Rahman, H.; Sample, K.; Schweitzer, B.; Srogl, J.; Neumann, W. L. *Org. Lett.* **2003,** *5,* 4349–4352. doi:10.1021/ol035649y
38. Prieur, V.; Pujol, M. D.; Guillaumet, G. *Eur. J. Org. Chem.* **2015,** 6547–6556. doi:10.1002/ejoc.201500625
39. Belaroussi, R.; Ejjoummany, A.; El Hakmaoui, A.; Akssira, M.; Guillaumet, G.; Routier, S. *RSC Adv.* **2018,** *8,* 732–741. doi:10.1039/c7ra12246b
40. Jakubkienė, V.; Vaičiūnaitė, E.; Kriukaitė, K.; Didžgalvis, J.; Tumkevičius, S. *Synth. Commun.* **2018,** *48,* 1974–1985. doi:10.1080/00397911.2018.1474229
41. Serevičius, T.; Skaisgiris, R.; Gudeika, D.; Kazlauskas, K.; Juršėnas, S. *Phys. Chem. Chem. Phys.* **2022,** *24,* 313–320. doi:10.1039/d1cp04905d
42. Serevičius, T.; Skaisgiris, R.; Dodonova, J.; Jagintavičius, L.; Banevičius, D.; Kazlauskas, K.; Tumkevičius, S.; Juršėnas, S. *ACS Appl. Mater. Interfaces* **2020,** *12,* 10727–10736. doi:10.1021/acsami.9b21394
43. Li, Z.; Li, W.; Keum, C.; Archer, E.; Zhao, B.; Slawin, A. M. Z.; Huang, W.; Gather, M. C.; Samuel, I. D. W.; Zysman-Colman, E. *J. Phys. Chem. C* **2019,** *123,* 24772–24785. doi:10.1021/acs.jpcc.9b08479
44. Chan, C.-Y.; Cui, L.-S.; Kim, J. U.; Nakanotani, H.; Adachi, C. *Adv. Funct. Mater.* **2018,** *28,* 1706023. doi:10.1002/adfm.201706023
45. Northey, T.; Stacey, J.; Penfold, T. J. *J. Mater. Chem. C* **2017,** *5,* 11001–11009. doi:10.1039/c7tc04099g
46. Stavrou, K.; Franca, L. G.; Monkman, A. P. *ACS Appl. Electron. Mater.* **2020,** *2,* 2868–2881. doi:10.1021/acsaelm.0c00514
47. Woo, S.-J.; Kim, Y.-H.; Kim, J.-J. *Chem. Mater.* **2021,** *33,* 5618–5630. doi:10.1021/acs.chemmater.1c01011
48. Etherington, M. K.; Gibson, J.; Higginbotham, H. F.; Penfold, T. J.; Monkman, A. P. *Nat. Commun.* **2016,** *7,* 13680. doi:10.1038/ncomms13680
49. de Mello, J. C.; Wittmann, H. F.; Friend, R. H. *Adv. Mater. (Weinheim, Ger.)* **1997,** *9,* 230–232. doi:10.1002/adma.19970090308
50. Serevičius, T.; Skaisgiris, R.; Kreiza, G.; Dodonova, J.; Kazlauskas, K.; Orentas, E.; Tumkevičius, S.; Juršėnas, S. *J. Phys. Chem. A* **2021,** *125,* 1637–1641. doi:10.1021/acs.jpca.0c10391
51. Rothe, C.; Monkman, A. P. *Phys. Rev. B* **2003,** *68,* 075208. doi:10.1103/physrevb.68.075208
52. *Gaussian 09;* Gaussian Inc.: Wallingford, CT, 2004.
53. Chen, X.-K. *CCS Chem.* **2020,** *2,* 1256–1267. doi:10.31635/ccschem.020.202000281
54. Yang, Z.; Huang, Y.-B.; Guo, Q.-X.; Fu, Y. *Chem. Commun.* **2013,** *49,* 5328–5330. doi:10.1039/c3cc40980e

License and Terms

BEILSTEIN JOURNAL OF ORGANIC CHEMISTRY

Post-synthesis from Lewis acid–base interaction: an alternative way to generate light and harvest triplet excitons

Hengjia Liu[1] and Guohua Xie[*1,2,3]

Review

Open Access

Address:
[1]Sauvage Center for Molecular Sciences, Hubei Key Lab on Organic and Polymeric Optoelectronic Materials, Department of Chemistry, Wuhan University, Wuhan 430072, People's Republic of China, [2]Key Laboratory for preparation and Application of Ordered Structural Materials of Guangdong Province, Shantou University, Shantou 518060, People's Republic of China and [3]Wuhan National Laboratory for Optoelectronics, Huazhong University of Science and Technology, Wuhan 430074, People's Republic of China

Email:
Guohua Xie[*] - guohua.xie@whu.edu.cn

* Corresponding author

Keywords:
excitons; fluorescence; Lewis acid; Lewis base; post-synthesis

Beilstein J. Org. Chem. **2022,** *18,* 825–836.
https://doi.org/10.3762/bjoc.18.83

Received: 01 March 2022
Accepted: 24 June 2022
Published: 12 July 2022

This article is part of the thematic issue "Organic TADF materials design".

Guest Editor: E. Zysman-Colman

Abstract

The changes in absorption and emission of fluorescent materials with the introduction of Lewis acids have been frequently observed due to either physical or chemical interactions. In this mini-review, we elaborate how Lewis acids adjust the optical properties and the bandgap of luminescent materials by simple coordination reactions. It is common that fluorescent materials containing Lewis basic nitrogen heterocycles are more likely to provide the feasible band gap modulation. The essence of such phenomenon originates from Lewis acid–base coordination and adducts, which highly depends on the electron-accepting property of the Lewis acids. This intermolecular mechanism, considered as post-synthesis of new luminescent compounds offers promising applications in sensing and electroluminescence by manipulating the frontier molecular orbital energy levels of organic conjugated materials, simply based on Lewis acid–base chemistry.

Introduction

Organic light emitting diodes (OLEDs) show great potential to dominate the next generation of flat-panel displays and efficient light sources attributed to the advantages of self-illumination, high efficiency, wide color gamut, and flexibility [1-3]. In OLEDs photons are mainly generated by radiative recombination in the emitting layer [4]. Therefore, the development of efficient luminescent materials and the exploration of new luminescent mechanisms are one of the core tasks in academic research. The most common luminescent materials are fluorescent compounds. Based on the spin statistics, the fluorescent emitters can only use singlet excitons for light generation [5]. In contrast, phosphorescent materials based on metal complexes

could achieve a high internal quantum efficiency (IQE) up to 100% through intersystem crossing (ISC) [6,7]. In 2012, Adachi et al. first reported purely organic thermally activated delayed fluorescent (TADF) materials, which achieved nearly 100% exciton utilization via reverse intersystem crossing (RISC) [8]. Meanwhile, novel materials based on new luminescence mechanisms such as hybridized local and charge-transfer (HLCT) and doublet emission have been designed and demonstrated [9,10]. However, the development of these materials often requires complicated molecular design and synthesis [11,12]. Alternatively, it is also possible to produce light emission by molecular exciplexes composed of multiple molecules [13]. The exciplex contains new excited states through charge transfer between a donor molecule and an acceptor molecule. This provides a simple way to create new luminescence processes through the intermolecular interactions of existing molecules [14].

It has been reported that new emitters can be realized by adding a Lewis acid to a fluorescent conjugated compound [15,16]. Lewis acids are common complexing agents [17] and are frequently used to dope conjugated polymers to enhance their conductivity while the luminescence is completely quenched [18,19]. In contrast, in the presence of nitrogen-containing heterocycles in the fluorescent materials, the addition of a Lewis acid tended to induce red-shifted absorption and emission, shedding light on the fact that the Lewis acid interacts easily with the nitrogen-containing fluorescent materials. This interaction mechanism is the coordination between Lewis acids and bases, which can finely adjust the optoelectronic properties of the fluorescent molecules, such as band gaps, peak wavelengths, and even frontier molecular orbitals if bound together [20]. The traditional way to manipulate the optoelectronic properties of the emitters highly depends on the molecular design and structures, including linkers, donor and acceptor units, which requires complex and time-consuming molecular synthesis and optimization [21-23]. In contrast, the introduction of specific Lewis acid–base pairs in existing molecules can be utilized to achieve brand new luminescent properties. In this mini-review, we summarize unique electron donor and acceptor materials which regulate luminescent properties via Lewis acid–base interactions and briefly explain the exploration of their chemical nature and interaction mechanisms.

Review

Lewis acids as electron acceptors

Some Lewis acids have good solubility in common organic solvents, which makes it easy to fabricate films for optoelectronic applications [24]. Because of their strong electrophilicity [25], Lewis acids may dominate charge distributions of the fluorescent materials featured with electron-rich nitrogen-containing heterocycles, resulting in the change of energy levels and spectra. The following will illustrate Lewis acids used in the exploration of luminescent materials and mechanisms due to Lewis acid–base interactions. The chemical structures of some candidate Lewis acids are shown in Figure 1.

In 2002, Monkman reported the addition of camphor sulfonic acid (CSA) to the fluorescent polymer poly{2,5-pyridylene-*co*-1,4-[2,5-bis(2-ethylhexyloxy)]phenylene} (compound **1** in Figure 2) containing pyridine groups led to the protonation effect [26]. CSA has strong acidity and low volatility, which is feasible to be bound with pyridine groups. As shown in Figure 3a, the protonation by CSA resulted in a significant red-shift in the photoluminescence (PL) spectrum, which was simi-

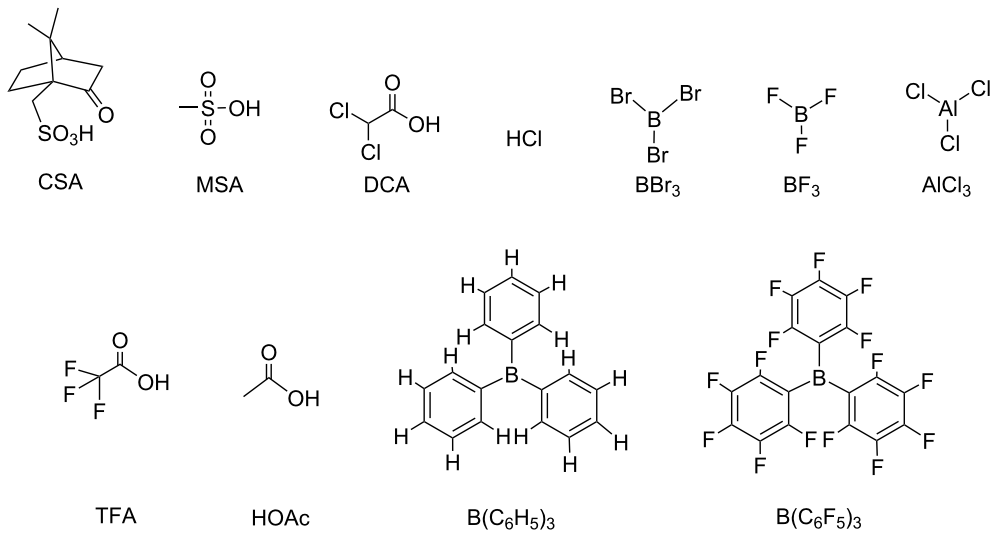

Figure 1: Chemical structures of Lewis acid examples.

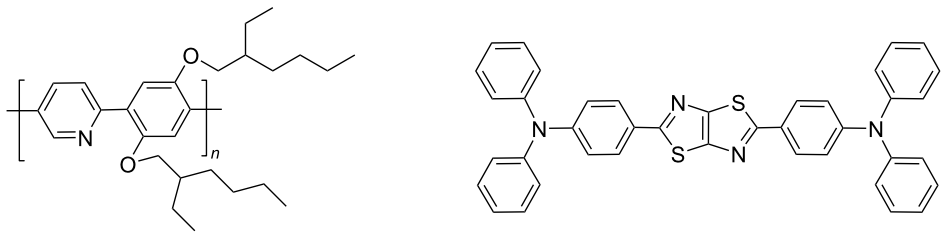

Figure 2: Chemical structures of Lewis basic fluorescent polymer poly{2,5-pyridylene-*co*-1,4-[2,5-bis(2-ethylhexyloxy)]phenylene} **1** and D–A–D compound 2,5-bis((*N*,*N*-diphenylamino)phenyl)thiazolothiazole **2**.

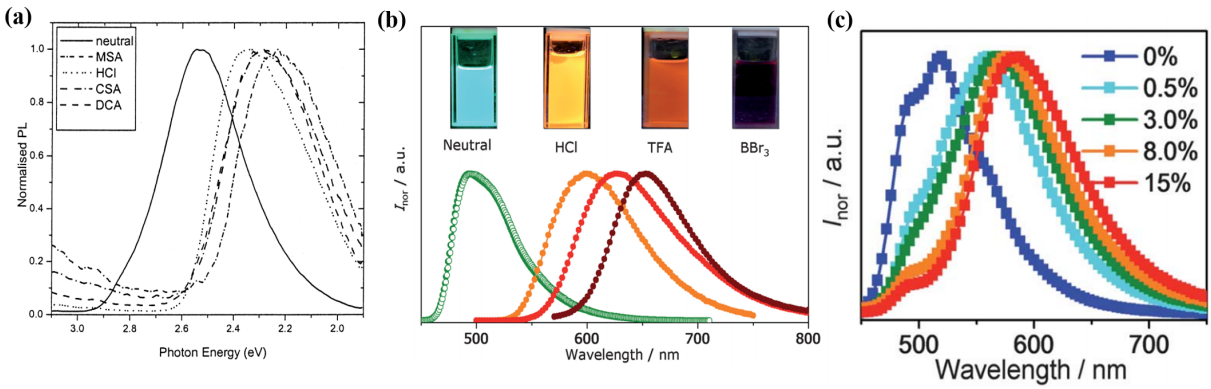

Figure 3: (a) Normalized PL spectra of films with compound **1** doped with different Lewis acids. (b) PL spectra of compound **2** under different acid conditions in dichloromethane. (c) EL spectra of devices with compound **2** doped with CSA at different concentrations. Figure 3a was reprinted with permission from [26], Copyright 2002 American Chemical Society. This content is not subject to CC BY 4.0. Figure 3b and 3c were reproduced from [27] with permission from The Royal Society of Chemistry. This content is not subject to CC BY 4.0.

lar to the cases caused by other Lewis acids such as methanesulfonic acid (MSA) and dichloracetic acid (DCA). Wang et al. used HCl, TFA, and BBr_3 as dopants which were respectively added to the donor–acceptor–donor (D–A–D) molecule 2,5-bis((*N*,*N*-diphenylamino)phenyl)thiazolothiazole (compound **2** in Figure 2) containing thiazolothiazole units. As shown in Figure 3b, four different colors ranged from green, yellow, red and NIR regions, i.e., a dramatic wavelength shift of 215 nm [27]. Light-emitting devices were fabricated by adding different concentrations of CSA into the fluorescent compound and a wide range of color tunability was observed in the EL spectra (see Figure 3c).

In 2009, Welch et al. employed the Lewis acid $B(C_6F_5)_3$ (BCF) to bind to nitrogen atoms at the basic site a of π-conjugated polymer, providing a simple strategy to regulate the optical properties of the A–D–A chromophore with charge transfer excited state properties [28]. In 2019, Wang et al. constructed a novel exciplex system by using the Lewis acids $B(C_6F_5)_3$ and $B(C_6H_5)_3$ as electron acceptors, respectively [29]. $B(C_6F_5)_3$ displays high chemical stability and Lewis acidity [30]. Moreover, its good solubility endows the possibility to form Lewis acid–base adducts in films by solution processing. The strong electron attraction of the fluorine substituents on the benzene rings of $B(C_6F_5)_3$ is responsible for its stronger Lewis acidity compared to $B(C_6H_5)_3$, and reacted efficiently with the basic fluorescent materials.

In 2011, Hayashi investigated the modification of pyridyl-conjugated polymer films with the Lewis acid BF_3 [31]. Through repeated acid–base treatment, the polymer film can achieve reversible color changing. Due to the poor solubility, the doped polymer film was simply prepared by BF_3 vapor treatment. The schematic diagram is shown in Figure 4. It is clear that the film achieved a gradient of colors from top to bottom under 365 nm UV light, which confirmed that the emission was sensitive to BF_3 concentration. Yang et al. used also TFA to shape the fluorescence emission based on the protonation effect between the dissociated H^+ and the fluorescent material [32].

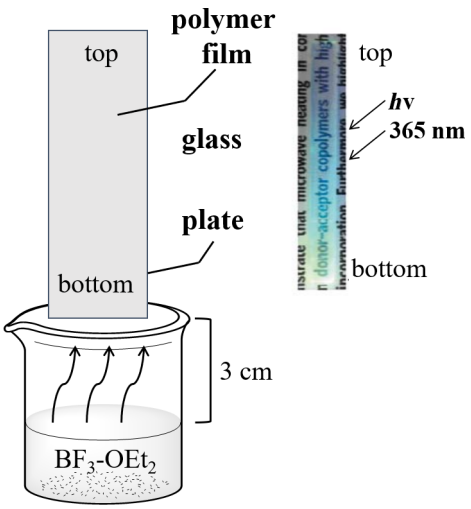

Figure 4: Schematic diagram of a BF_3·OEt_2 vapor-treated device and the macroscopic gradation emissive pattern of polymer films on a glass plate after treatment and excited by 365 nm UV light. Figure 4 was reproduced from [31] with permission from The Royal Society of Chemistry. This content is not subject to CC BY 4.0.

Lin et al. used the Lewis acids $B(C_6F_5)_3$ and $AlCl_3$ to regulate the optoelectronic properties of a fluorene-based copolymer with an sp^2 nitrogen heteroatom via supramolecular coordination [33]. The PL emission in solution showed an obvious red-shifted profile. The polymer LED with different molar equivalents of Lewis acids was investigated. The EL peak wavelength was gradually red-shifted with increasing the concentration of the Lewis acid, changing from 440 nm to 520 nm. In order to further explore the doping mechanism of Lewis acid on organic semiconductors, Yurash et al. found that $B(C_6F_5)_3$ possessed the best doping effect and thus increased the conductivity, compared with BF_3, BBr_3, and $AlCl_3$, respectively, mixed in the low bandgap conjugated polymer materials. This is ascribed to the formation of Lewis acid–base adducts [34].

Fluorescent materials as electron donors

Hancock et al. compared the PL and EL spectra of the π-conjugated heterocyclic oligomer 6,6'-bis(2-(1-pyrenyl)-4-octylquinoline) (BPYOQ, compound **3** in Figure 5), which could be tuned in the whole visible range through the complex reaction

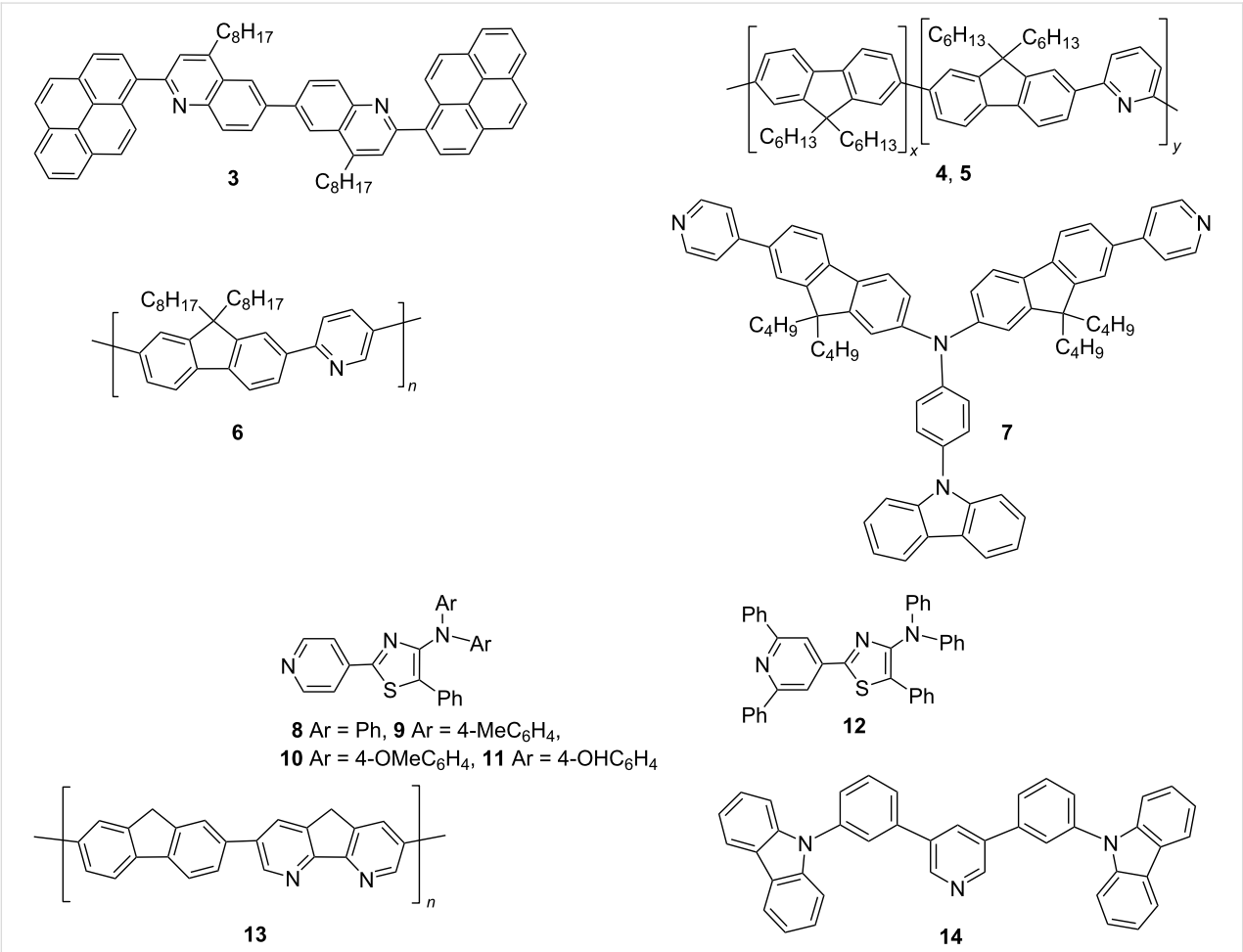

Figure 5: Chemical structures of Lewis basic fluorescent compounds **3–14**.

with CSA [35]. This is supposed to be the first EL example of the protonated organic semiconductor. Compound **3** is an aromatic end-capped oligoquinoline, with both quinoline and pyridine as N-containing heterocycles rich in electrons, which are the key structural factors leading to acid discoloration. At the same time, Kappaun et al. synthesized a series of conjugated alternating and statistical copolymers (poly[2,7-(9,9-dihexylfluorenyl)-*alt*-(2,6-pyridinyl)]) (compound **4** in Figure 5) and (poly[2,7-(9,9-dihexylfluorenyl)-*stat*-(2,6-pyridinyl)]) (compound **5** in Figure 5) with pyrene and pyridine units [36]. The pyridine groups in the conjugated polymer contain basic sites presumably induced by nitrogen atoms, where protonation occurred.

In 2012, Zalar et al. synthesized the conjugated polymer F8Py (compound **6** in Figure 5), in which the incorporation of the pyridine co-monomer provides a lone pair of electrons for binding Lewis acids [37]. The formation of acid–base adducts accurately regulated the band gap of the luminescent polymer. The PL spectra in solution showed the evident red-shift upon mixing the polymer with the Lewis acid (Figure 6a). This property was also successfully demonstrated in OLEDs to modify the electroluminescence (EL) characteristics (Figure 6b).

In 2020, Yang et al. designed and synthesized a blue fluorescent material CzPA-F-PD (compound **7** in Figure 5), which consisted of the twisted A–π–D–π–A structure with *N*-(4-aminophenyl)carbazole (CzPA) as electron donor unit, pyridine as electron acceptor unit, and 9,9-dioctylfluorene (F) as π-conjugated linker [32]. Compound **7** showed remarkable dual-fluorescence properties when mixed with a very small amount of trifluoroacetic acid (TFA). As shown in Figure 6c, the PL spectra in solution were dominated by the amount of TFA. At the appropriate ratio, the solution-processed device with compound **7** as single emission layer generated broadband white light emission under EL process (see Figure 6d).

In 2016, Yamaguchi et al. designed and synthesized a series of 5-*N*-arylaminothiazoles with 4-pyridyl groups at the 2-position (compounds **8–12** in Figure 5), which behaved as strong Lewis basic sites [38]. After adding BCF to compound **12**, a new emission peak was generated in the orange-red region, accom-

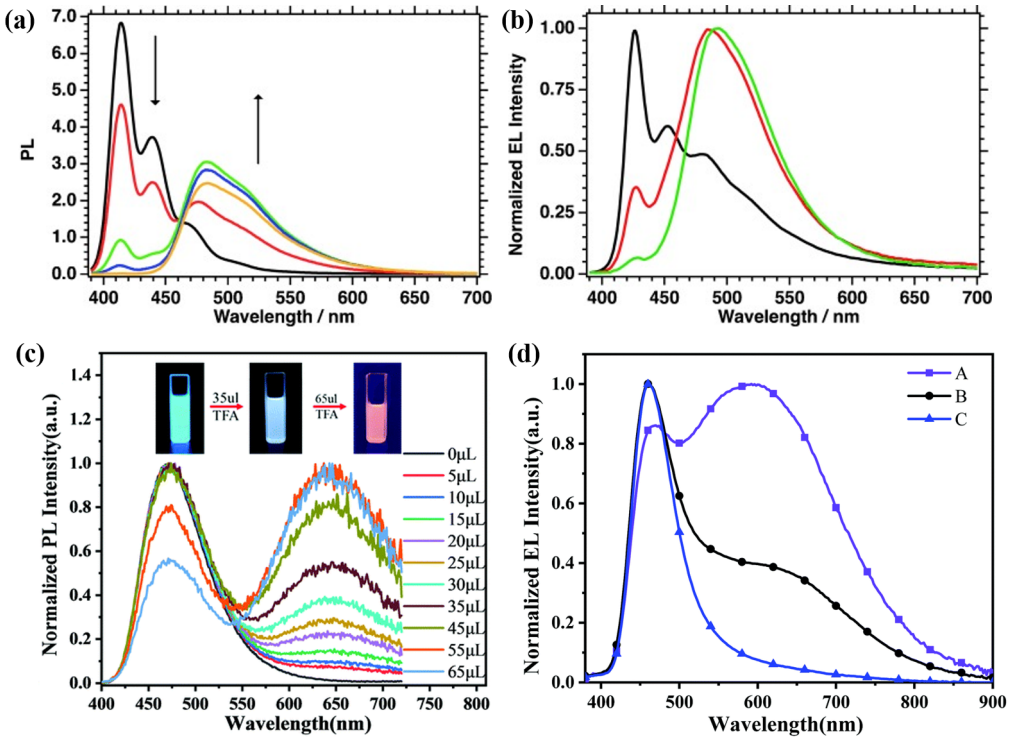

Figure 6: (a) PL spectra of compound **6** in toluene after addition of 0.0 (black line), 0.1 (red line), 0.3 (green line), 0.7 (blue line), 1.3 mol equiv (orange line) $B(C_6F_5)_3$. (b) EL spectra of the device with compound **6** at a constant current density of 111 mA cm^{-2} for 0.00 (black line), 0.01 (red line), and 0.02 mol equiv (green) $B(C_6F_5)_3$. (c) PL spectra of compound **7** in solution containing different amounts of TFA under irradiation of UV light. (d) EL spectra of devices with different ratios of compound **7** and TFA; device A, compound **7**/TFA 50:1 (v/v); device B, compound **7**/TFA 5000:1 (v/v); device C, neat film of compound **7**. Figure 6a and 6b were reproduced from [37], P. Zalar et al., "Color Tuning in Polymer Light-Emitting Diodes with Lewis Acids", Angew. Chem., Int. Ed., with permission from John Wiley and Sons. Copyright © 2012 WILEY-VCH Verlag GmbH & Co. KGaA, Weinheim. This content is not subject to CC BY 4.0. Figure 6c and 6d were reproduced from [32] with permission from The Royal Society of Chemistry. This content is not subject to CC BY 4.0.

panied with a decrease of the original blue emission, as shown in Figure 7. The PL emission changed from blue to orange. This phenomenon was also reproducible by adding other Lewis acids, such as BCl_3 and $AlCl_3$. Interestingly, white light emission was achievable by adjusting the ratio of $B(C_6F_5)_3$. Regarding the materials developed by Lin et al., supramolecular coordination of PF8-co-DAF8 (**13**, Figure 5) with Lewis acids played an important role. They selected the more rigid 4,5-diazafluorene (DAF) with nitrogen atoms inserted at the 4 and 5-positons of the fluorene moiety [33]. The heteroatomic fluorene showed enhanced planarity of the molecule. The coordination tended to be more efficient if a stronger Lewis acid was employed.

The bipolar host material 35DCzPPy (**14**, Figure 5) was initially synthesized by Kido's group [39]. It combines two carbazole electron donors with high triplet energy and a pyridine electron acceptor with high electron affinity. Later in 2020, Wang's group employed this host material, respectively mixed with two Lewis acids, namely BCF and $B(C_6H_5)_3$, to construct highly luminescent exciplexes [29]. The PL spectra of the new emission system showed an obvious red-shift through intermolecular charge transfer. Compared with $B(C_6H_5)_3$, the exciplex system constructed by BCF exhibited a more pronounced red-shift in the PL spectra and unexpectedly improved EL properties.

The fluorescent materials, which can easily interact with Lewis acids and simultaneously exhibit significant chemical and photophysical changes, have some common structural characteristics. For instance, heterocyclic units containing a nitrogen atom such as pyridine and thiazole, are one of the key structural features either in small molecules or polymers. Thus, the introduction of nitrogen with lone pairs of electrons in fluorescent materials, makes them have a good affinity for Lewis acids. In other words, these fluorescent materials contain Lewis basic sites for the formation of Lewis acid–base pairs. According to this principle, it can be inferred that analogous materials containing basic nitrogen atoms tend to interact with the Lewis acids discussed in this review and thus lead to a significant shift of their optoelectronic properties. It has been confirmed that organic molecules containing pyrimidine, pyrazine, and indole groups display similar interactions upon the addition of Lewis acids [40-42].

Lewis acid–base interaction mechanisms

Chemical essence of Lewis acid–base interaction

All the above discussed fluorescent materials share the common characteristics of Lewis basicity. Therefore, the changes in band gaps and colors of the donor materials is essentially attributed to a Lewis acid–base complexation reaction. In order to clarify the coordination reaction of nitrogen atoms, Bazan's group designed a conjugated polymer containing pyridine and thiazole groups and small molecule **15** (Figure 8) and compared the ^1H NMR spectra and ^{19}F NMR spectra after the addition of 1 equivalent $B(C_6F_5)_3$ at various temperatures from 230 to 300 K (see Figure 9) [43].

As shown in Figure 9a, when the temperature reached 280 K, the aromatic resonances became intense, implying the appearance of a new species, which was assigned to the Lewis acid–base adduct. Fifteen new resonance peaks were also observed in the ^{19}F NMR spectrum (see Figure 9b), which were different from the same chemical environment of fluorine atoms in the original $B(C_6F_5)_3$. To further explore the interaction of the Lewis acid–base pairs, Huang et al. added $B(C_6F_5)_3$ to pyridine group-capped diketopyrrolopyrrole (DPP) molecules, i.e., DPPPy-Py-F (**16**), DPPPy-Ph-3F (**17**), and DPPPy-Ph-F (**18**, Figure 8), and determined the ^{11}B NMR spectra (Figure 9c) [44]. When coordinated with nitrogen atoms, the resonance peak shifted slightly from ca. −10 to 0 ppm, which suggested the interaction between boron and nitrogen atoms.

Wang's group studied the interaction of compound **14** respectively with $B(C_6F_5)_3$ and $B(C_6H_5)_3$ by X-ray photoelectron spectroscopy (XPS) [29]. The B(1s) signal showed peaks at 190.61 and 191.08 eV, respectively. This is close to the reported characteristic B–N binding energy (190.5 eV) in B–N

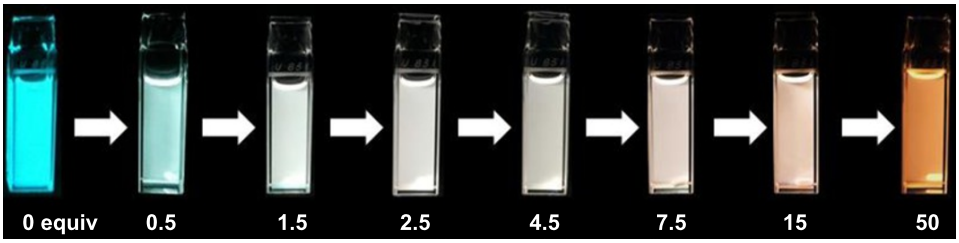

Figure 7: Photos of a solution of compound **12** and $B(C_6F_5)_3$ at different ratios in toluene under a 365 nm UV lamp. Figure 7 was reproduced from [38] (© 2016 K. Yamaguchi et al., published by Wiley-VCH Verlag GmbH & Co. KGaA, distributed under the terms of the Creative Commons Attribution-NonCommercial 4.0 International License, https://creativecommons.org/licenses/by-nc/4.0/). This content is not subject to CC BY 4.0.

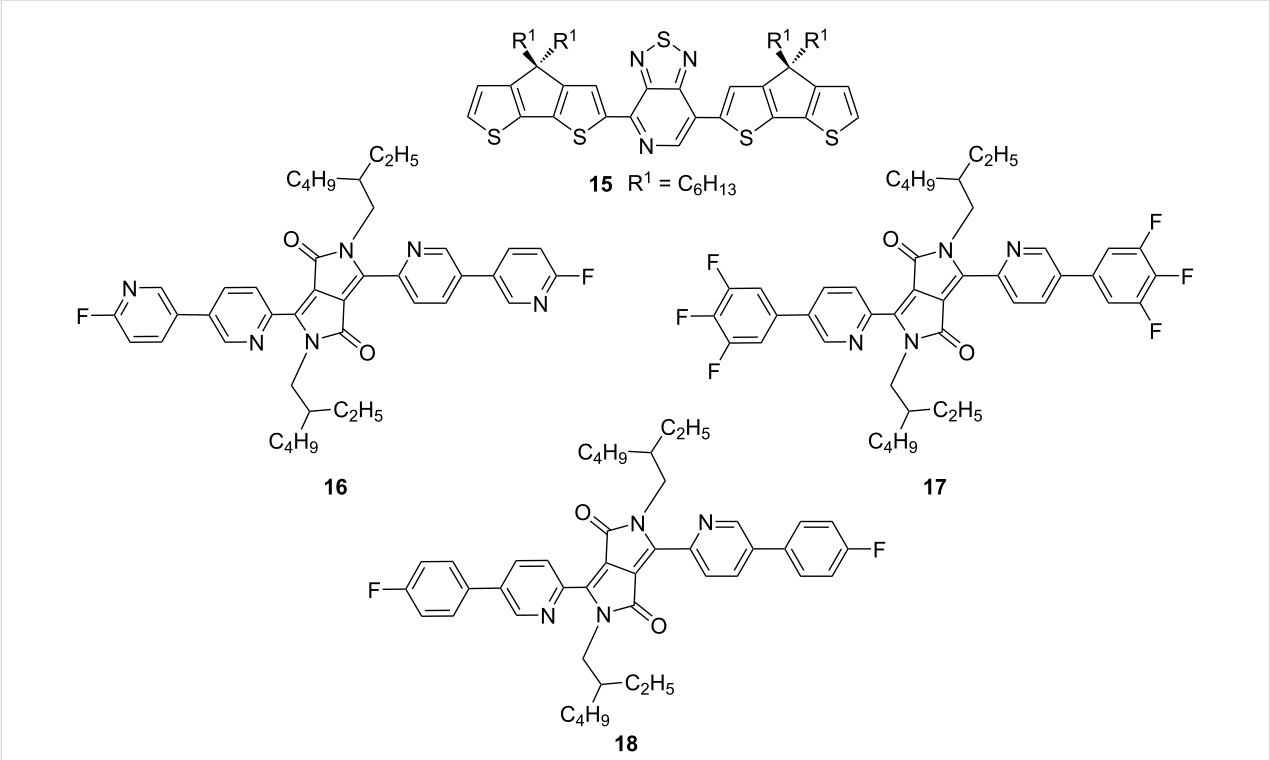

Figure 8: Structure of small molecule **15** containing pyridine and thiazole groups reported by Bazan et al. and pyridine groups-containing diketo-pyrrolopyrroles (DPP) **16**–**18** investigated by Huang et al.

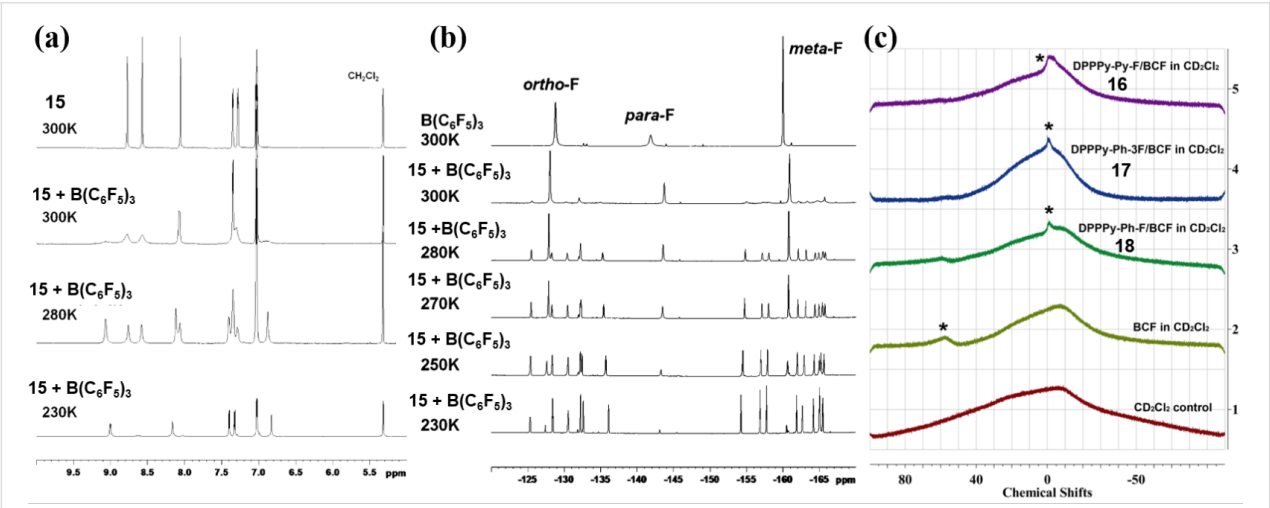

Figure 9: (a) ^{1}H NMR spectra in the aromatic region and (b) ^{19}F NMR spectra of compound **15** (top) and the mixture with 1 equivalent $B(C_6F_5)_3$ at different temperatures from 300 to 230 K. (c) ^{11}B NMR spectra of $B(C_6F_5)_3$, DPPPy-Py-F (compound **16**)/$B(C_6F_5)_3$, DPPPy-Ph-3F (compound **17**)/$B(C_6F_5)_3$, and DPPPy-Ph-F (compound **18**)/$B(C_6F_5)_3$ in CD_2Cl_2, respectively. Figure 9a and 9b were reprinted with permission from [43], Copyright 2011 American Chemical Society. This content is not subject to CC BY 4.0. Figure 9c was reprinted from [44], Dyes and Pigments, vol. 153, by J. Huang; Y. Li, Y. Wang; H. Meng; D. Yan; B. Jiang; Z. Wei; C. Zhan, "A Lewis acid-base chemistry approach towards narrow bandgap dye molecules", pages 1–9, Copyright (2018), with permission from Elsevier. This content is not subject to CC BY 4.0.

crystals. Despite the weak signals of boron in these two Lewis acids, it was assumed that compound **14** formed a B–N coordination bond when doped with $B(C_6F_5)_3$ and $B(C_6H_5)_3$, respectively.

Luminescent mechanisms

In view of the phenomenon that Lewis acid–base coordination contributes to a decrease of the band gap and bathochromic shifts of absorption and emission, it is essential to explore the

mechanisms. Welch et al. supposed that the strong electrophilic Lewis acid triggers charge transfer with nitrogen-containing heterocycles containing lone-pair electrons. Consequently, it reduces the electron density of the π-conjugated system and the characteristics of the excited states, accounting for the decrease of band gap [27,37,43]. In 2018, Li et al. used density functional theory (DFT) to investigate the energy levels of polymers **19** (P1) and **20** (P2, Figure 10) containing pyrazine groups before and after the addition of $B(C_6F_5)_3$ (see Figure 11a) [45]. Considering the electrostatic potential surface (EPS) maps (see Figure 11b) of the pyrazine-containing polymers before and after $B(C_6F_5)_3$ coordination, it is likely that $B(C_6F_5)_3$ sacrificed the electron density of the polymer skeleton and turned it from an electron-rich to an electron-deficient species. This was assumed to be the reason for the decrease of the band gap. Meanwhile, the LUMO levels estimated from electrochemistry experiments (see Figure 11c and 11d) were also depressed from −3.60 eV (compound **19**) to −3.96 eV (compound **19**/$B(C_6F_5)_3$) and from −3.59 eV (compound **20**) to −4.12 eV (compound **20**/$B(C_6F_5)_3$), which were consistent with the theoretical calculation results.

Yang and co-workers compared the energy level distributions of the HOMO and LUMO of CzPA-F-PD (compound **7** in Figure 5) before and after protonation, which were diverse [32]. The cyclic voltammogram (CV) curves of CzPA-F-PD and CzPA-F-PD-H^+ showed that the energy levels of both the HOMO and LUMO of CzPA-F-PD-H^+ decreased relative to

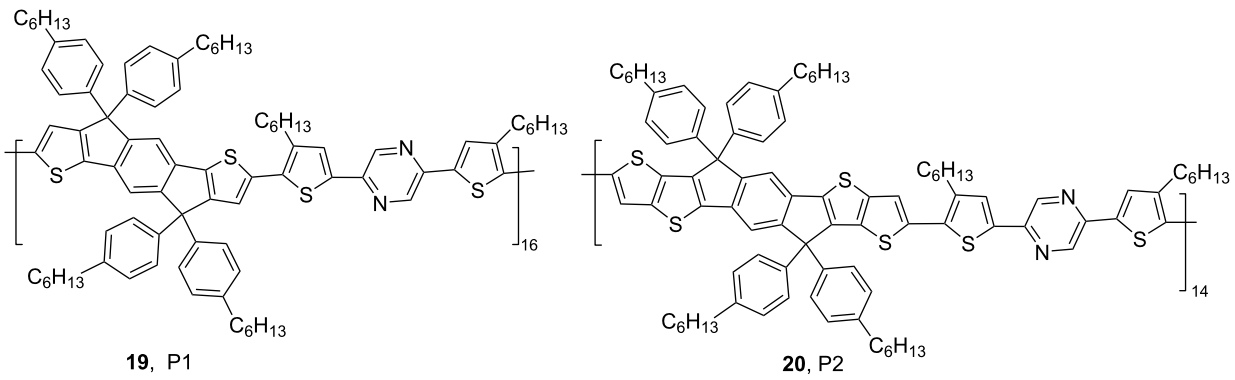

Figure 10: Pyrazine-containing polymers **19** and **20** investigated by Li et al.

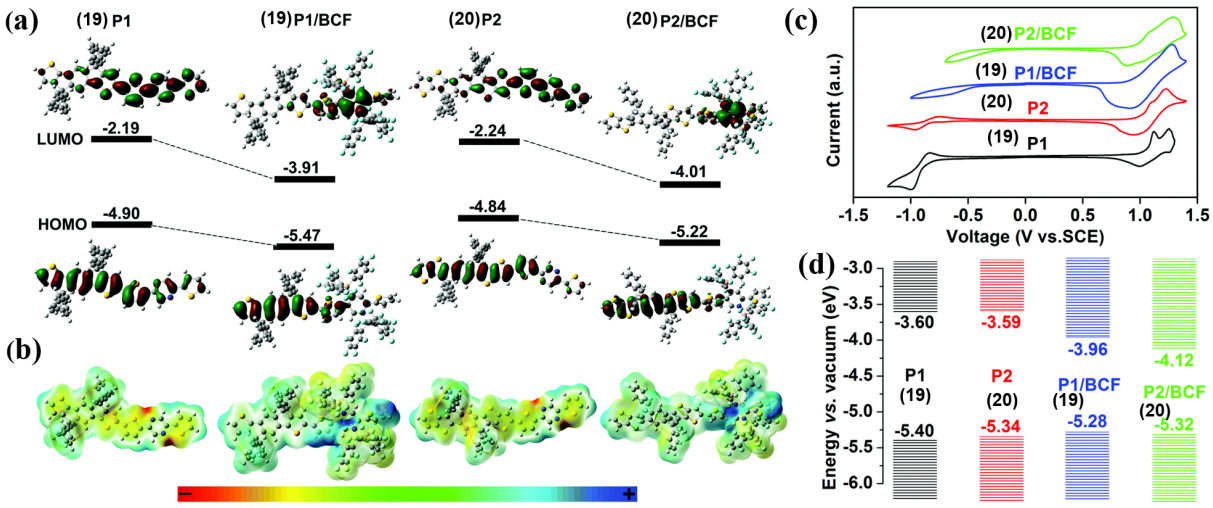

Figure 11: (a) HOMO/LUMO orbitals and energy levels (unit: eV) and (b) electrostatic potential surface (EPS) maps calculated by Gaussian 09 at the B3LYP/6-31G(d,p) level of theory. (c) Cyclic voltammetry curves of the four compounds and HOMO/LUMO energy level diagram and (d) estimated from the CV tests. Figure 11a–d were reproduced from [45] with permission from The Royal Society of Chemistry. This content is not subject to CC BY 4.0.

those of CzPA-F-PD, and the LUMO level decreased more significantly. According to the theoretical calculation results, the HOMO and LUMO distributions of CzPA-F-PD-H^+ were more spatially separated, the charge transfer characteristics of the excited states turned to be stronger, and the localized excited states characteristics was reduced. The energy level gap between S_1 and T_1 (ΔE_{ST}) of CzPA-F-PD-H^+ was 0.16 eV, which is significantly lower than the 0.39 eV of CzPA-F-PD [32].

The formation of exciplexes, e.g., with the donor-like 35DCzPPy (compound **14** in Figure 5) and acceptor-like Lewis acids, effectively reduces the energy gap between S_1 and S_0 and thus leads to a red-shift of emission (Figure 12a), as claimed by Xie and Wang's group [29]. The absorption of both 35DCzPPy:$B(C_6F_5)_3$ and 35DCzPPy:$B(C_6H_5)_3$ were nearly identical to that of their constituting materials, which suggested that there existed no new ground-state in the exciplex films (Figure 12b). The reduction of the LUMO energy level would correlate closely with the protonation effect on the pyridine unit of the donor. More importantly, delayed fluorescence profiles of the exciplexes were detected (see Figure 12c, τ_1 = 57.07 ns and τ_2 = 158.20 ns), which proved the possibility to harvest triplet excitons based on Lewis acid–base adducts. Therefore, the OLED using 35DCzPPy:$B(C_6F_5)_3$ as the emitting layer exhibited a maximum external quantum efficiency of ≈6.2%, surpassing the upper limit (ca. 5%) of the conventional fluorescence devices.

Strength of Lewis acid–base interactions

The energy levels of Lewis acid–base adducts are sensitive to the strength of the Lewis acids and bases. In 2002, Monkman et al. found that the degree of the spectral red-shift of protonated conjugated polymers depended greatly on the strength of the Lewis acid (Figure 3a) [26]. Wang et al. modulated the electron-accepting strength of intramolecular charge transfer molecules by using different acids and obtained four distinctly different solid-state emission colors of green (524 nm), yellow (576 nm), red (640 nm), and NIR (739 nm) (Figure 3b) [27]. The stronger Lewis acidity resulted in a stronger emission and bathochromic shift when comparing the effects of BCF and $B(C_6H_5)_3$ on the optoelectronic properties of the organic UV fluorescent material 35DCzPPy (**14**, Figure 5) [29,39]. As illustrated in Figure 12a, BCF can narrow down the bandgap of the exciplex because of the stronger electrophilicity of the fluorine atoms. Similarly, Yamaguchi et al. used molecular modifications to introduce stronger electron donors to luminescent molecules and obtained stronger spectral changes [38]. This demonstrates that stronger Lewis acids and Lewis bases will result in stronger charge transfer. Moreover, stronger electron donors or more accessible nitrogen-containing groups would interact easily via Lewis acid coordination. As shown in Figure 13b, the energy levels determined from the optimized structures of compounds **21** and **22** (Figure 13a) by DFT suggest that pyridine is a better binding site than thiophene [43].

The effect of steric hindrance on the Lewis acid–base binding should not be ignored. If there is large steric hindrance of the Lewis basic molecules, it will hinder the coordination with a Lewis acid. For example, Bazan's group investigated the analogous compounds **21** and **22** shown in Figure 13a, featuring the same nitrogen heterocycles but with different steric hindrances. Subsequently, the ability of their coordination with $B(C_6F_5)_3$ and BBr_3 was compared, respectively [43]. As displayed in Figure 13c and 13d, the UV–vis–NIR absorption spectra manifested that the larger steric hindrance interrupted the binding of BCF more effectively than that of BBr_3.

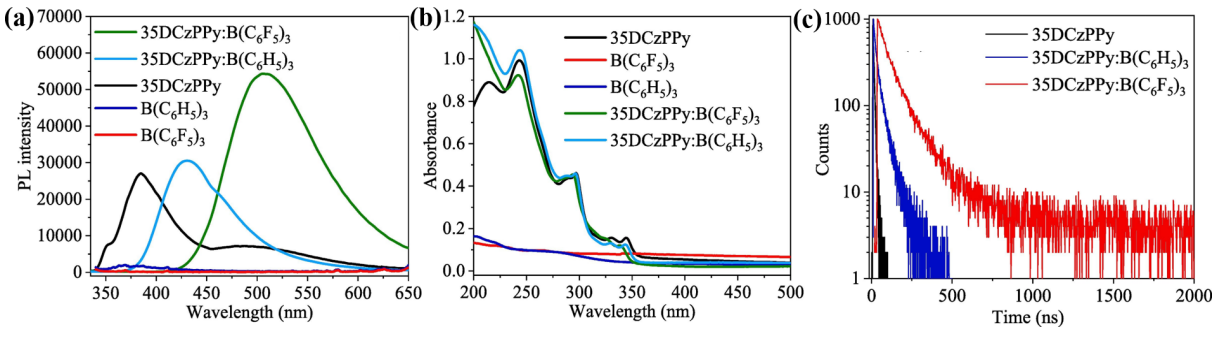

Figure 12: (a) UV–vis absorbance and (b) PL spectra (excited by 330 nm) for 35DCzPPy (compound **14**), $B(C_6F_5)_3$, $B(C_6H_5)_3$, 35DCzPPy:$B(C_6F_5)_3$ (1:1), and 35DCzPPy:$B(C_6H_5)_3$ (1:1) in films. (c) Fluorescence decay curves for the solid films of 35DCzPPy, 35DCzPPy:$B(C_6H_5)_3$, and 35DCzPPy:$B(C_6F_5)_3$ recorded at photoluminescence maxima (385, 435, and 509 nm) at room temperature. Figure 12 was reprinted from [29], Chemical Engineering Journal, vol. 380, by M. Zhang; G. Xie; Q. Xue; H. Wang, "Electroluminescence of intra-molecular exciplexes based on novel Lewis acid borane acceptors and a high triplet level donor", article no. 122527, Copyright (2020), with permission from Elsevier.

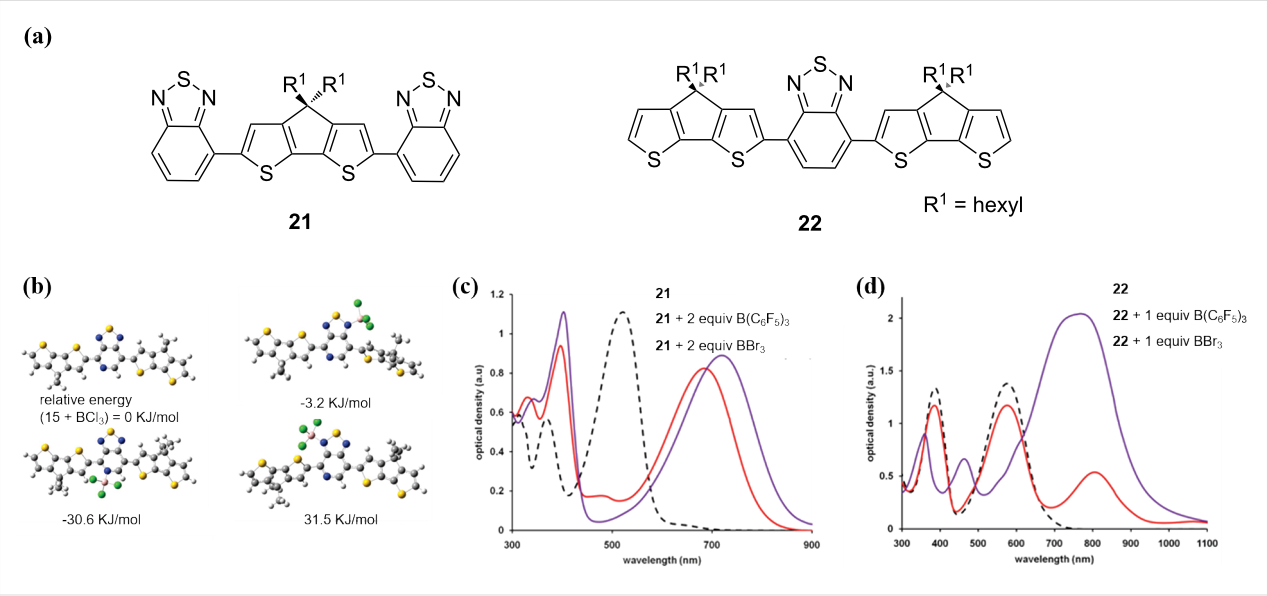

Figure 13: (a) Schematic diagram of the low-band gap materials **21** and **22**. (b) Ground state geometry optimizations of compound **15** and its corresponding adducts with BCl_3. The optimized structures were calculated using DFT at the B3LYP/6-31G (d,p) level of theory. UV–vis–NIR absorption spectra of (c) compound **21** and (d) compound **22** before and after adding the Lewis acids $B(C_6F_5)_3$ and BBr_3 in *o*-DCB solution, respectively. Figure 13b–d were reprinted with permission from [43], Copyright 2011 American Chemical Society. This content is not subject to CC BY 4.0.

Conclusion

For fluorescent materials containing nitrogen atoms with Lewis basic nature, it is easily found that the addition of suitable Lewis acids can lead to a dramatic red-shift in the absorption and emission of the mixtures. The electrophilic Lewis acid as electron acceptor frequently reacts with the nitrogen-containing heterocyclic conjugated molecules, ascribed to the charge redistributions of the molecules. This governs their optoelectronic properties and most likely rouses the non-radiative triplet excitons of reverse intersystem crossing.

Lewis acid–base chemistry provides a simple and effective way to finely regulate the optoelectronic properties of fluorescent materials, avoiding the complicated molecular synthesis. Lewis acid–base interactions found some promising applications in band gap engineering, photoluminescence, and electroluminescence. The in-depth study of the mechanisms of this phenomenon could inspire the innovation in cutting-edge researches beyond organic light-emitting diodes [29,32], e.g., organic thin-film transistors [45,46], organic photovoltaics [47], and chemical sensing [48].

Funding

The authors acknowledge the financial support from the National Natural Science Foundation of China (Nos. 51873159 and 62175189). G. X. acknowledges the funding support from the Program for Promoting Academic Collaboration and Senior Talent Fostering between China and Canada, Australia, New Zealand and Latin America (2021-109), the Open Fund of Key Laboratory for Preparation and Application of Ordered Structural Materials of Guangdong Province, Shantou University (No. KLPAOSM202003), and the Open Project Program of Wuhan National Laboratory for Optoelectronics (No. 2019WNLOKF015).

ORCID® iDs

Guohua Xie - https://orcid.org/0000-0003-0764-7889

References

1. Wong, M. Y.; Zysman-Colman, E. *Adv. Mater. (Weinheim, Ger.)* **2017,** *29,* 1605444. doi:10.1002/adma.201605444
2. Reineke, S.; Lindner, F.; Schwartz, G.; Seidler, N.; Walzer, K.; Lüssem, B.; Leo, K. *Nature* **2009,** *459,* 234–238. doi:10.1038/nature08003
3. Yin, D.; Feng, J.; Ma, R.; Liu, Y.-F.; Zhang, Y.-L.; Zhang, X.-L.; Bi, Y.-G.; Chen, Q.-D.; Sun, H.-B. *Nat. Commun.* **2016,** *7,* 11573. doi:10.1038/ncomms11573
4. Tang, C. W.; VanSlyke, S. A. *Appl. Phys. Lett.* **1987,** *51,* 913–915. doi:10.1063/1.98799
5. Tao, Y.; Yuan, K.; Chen, T.; Xu, P.; Li, H.; Chen, R.; Zheng, C.; Zhang, L.; Huang, W. *Adv. Mater. (Weinheim, Ger.)* **2014,** *26,* 7931–7958. doi:10.1002/adma.201402532
6. Adachi, C.; Baldo, M. A.; Thompson, M. E.; Forrest, S. R. *J. Appl. Phys.* **2001,** *90,* 5048–5051. doi:10.1063/1.1409582
7. Minaev, B.; Baryshnikov, G.; Agren, H. *Phys. Chem. Chem. Phys.* **2014,** *16,* 1719–1758. doi:10.1039/c3cp53806k
8. Uoyama, H.; Goushi, K.; Shizu, K.; Nomura, H.; Adachi, C. *Nature* **2012,** *492,* 234–238. doi:10.1038/nature11687
9. Li, W.; Pan, Y.; Yao, L.; Liu, H.; Zhang, S.; Wang, C.; Shen, F.; Lu, P.; Yang, B.; Ma, Y. *Adv. Opt. Mater.* **2014,** *2,* 892–901. doi:10.1002/adom.201400154

10. Ai, X.; Evans, E. W.; Dong, S.; Gillett, A. J.; Guo, H.; Chen, Y.; Hele, T. J. H.; Friend, R. H.; Li, F. *Nature* **2018,** *563,* 536–540. doi:10.1038/s41586-018-0695-9
11. Ma, X.; Mao, X.; Zhang, S.; Huang, X.; Cheng, Y.; Zhu, C. *Polym. Chem.* **2013,** *4,* 520–527. doi:10.1039/c2py20677c
12. Armelao, L.; Quici, S.; Barigelletti, F.; Accorsi, G.; Bottaro, G.; Cavazzini, M.; Tondello, E. *Coord. Chem. Rev.* **2010,** *254,* 487–505. doi:10.1016/j.ccr.2009.07.025
13. Liu, X.-K.; Chen, Z.; Zheng, C.-J.; Liu, C.-L.; Lee, C.-S.; Li, F.; Ou, X.-M.; Zhang, X.-H. *Adv. Mater. (Weinheim, Ger.)* **2015,** *27,* 2378–2383. doi:10.1002/adma.201405062
14. Zhao, J.; Zheng, C.; Zhou, Y.; Li, C.; Ye, J.; Du, X.; Li, W.; He, Z.; Zhang, M.; Lin, H.; Tao, S.; Zhang, X. *Mater. Horiz.* **2019,** *6,* 1425–1432. doi:10.1039/c9mh00373h
15. Monkman, A. P.; Halim, M.; Samuel, I. D. W.; Horsburgh, L. E. *J. Chem. Phys.* **1998,** *109,* 10372–10378. doi:10.1063/1.477692
16. Enoki, T.; Matsuo, K.; Ohshita, J.; Ooyama, Y. *Phys. Chem. Chem. Phys.* **2017,** *19,* 3565–3574. doi:10.1039/c6cp08573c
17. Yoon, C. O.; Reghu, M.; Moses, D.; Heeger, A. J.; Cao, Y. *Synth. Met.* **1994,** *63,* 47–52. doi:10.1016/0379-6779(94)90247-x
18. Alam, M. M.; Jenekhe, S. A. *J. Phys. Chem. B* **2002,** *106,* 11172–11177. doi:10.1021/jp021230y
19. Luan, K.; Dao, T.; Kido, J. *J. Photopolym. Sci. Technol.* **2002,** *15,* 261–264. doi:10.2494/photopolymer.15.261
20. Zhu, C.; Guo, Z.-H.; Mu, A. U.; Liu, Y.; Wheeler, S. E.; Fang, L. *J. Org. Chem.* **2016,** *81,* 4347–4352. doi:10.1021/acs.joc.6b00238
21. Thirion, D.; Rault-Berthelot, J.; Vignau, L.; Poriel, C. *Org. Lett.* **2011,** *13,* 4418–4421. doi:10.1021/ol201751p
22. Thurakkal, S.; Sanju, K. S.; Soman, A.; Unni, K. N. N.; Joseph, J.; Ramaiah, D. *New J. Chem.* **2018,** *42,* 5456–5464. doi:10.1039/c7nj04386d
23. Li, Y.; Yao, J.; Wang, C.; Zhou, X.; Xu, Y.; Hanif, M.; Qiu, X.; Hu, D.; Ma, D.; Ma, Y. *Dyes Pigm.* **2020,** *173,* 107960. doi:10.1016/j.dyepig.2019.107960
24. Zalar, P.; Kuik, M.; Henson, Z. B.; Woellner, C.; Zhang, Y.; Sharenko, A.; Bazan, G. C.; Nguyen, T.-Q. *Adv. Mater. (Weinheim, Ger.)* **2014,** *26,* 724–727. doi:10.1002/adma.201303357
25. Mayr, H.; Schade, C.; Rubow, M.; Schneider, R. *Angew. Chem., Int. Ed. Engl.* **1987,** *26,* 1029–1030. doi:10.1002/anie.198710291
26. Monkman, A. P.; Pålsson, L.-O.; Higgins, R. W. T.; Wang, C.; Bryce, M. R.; Batsanov, A. S.; Howard, J. A. K. *J. Am. Chem. Soc.* **2002,** *124,* 6049–6055. doi:10.1021/ja012409+
27. Wang, K.; Huang, S.; Zhang, Y.; Zhao, S.; Zhang, H.; Wang, Y. *Chem. Sci.* **2013,** *4,* 3288–3293. doi:10.1039/c3sc51091c
28. Welch, G. C.; Coffin, R.; Peet, J.; Bazan, G. C. *J. Am. Chem. Soc.* **2009,** *131,* 10802–10803. doi:10.1021/ja902789w
29. Zhang, M.; Xie, G.; Xue, Q.; Wang, H.-B. *Chem. Eng. J.* **2020,** *380,* 122527. doi:10.1016/j.cej.2019.122527
30. Piers, W. E. *Adv. Organomet. Chem.* **2004,** *52,* 1–76. doi:10.1016/s0065-3055(04)52001-4
31. Hayashi, S.; Asano, A.; Koizumi, T. *Polym. Chem.* **2011,** *2,* 2764–2766. doi:10.1039/c1py00363a
32. Yang, J.; Liu, X.; Liu, Z.; Wang, L.; Sun, J.; Guo, Z.; Xu, H.; Wang, H.; Zhao, B.; Xie, G. *J. Mater. Chem. C* **2020,** *8,* 2442–2450. doi:10.1039/c9tc06425g
33. Lin, J.; Liu, B.; Yu, M.; Xie, L.; Zhu, W.; Ling, H.; Zhang, X.; Ding, X.; Wang, X.; Stavrinou, P. N.; Wang, J.; Bradley, D. D. C.; Huang, W. *Macromol. Rapid Commun.* **2016,** *37,* 1807–1813. doi:10.1002/marc.201600445
34. Yurash, B.; Cao, D. X.; Brus, V. V.; Leifert, D.; Wang, M.; Dixon, A.; Seifrid, M.; Mansour, A. E.; Lungwitz, D.; Liu, T.; Santiago, P. J.; Graham, K. R.; Koch, N.; Bazan, G. C.; Nguyen, T.-Q. *Nat. Mater.* **2019,** *18,* 1327–1334. doi:10.1038/s41563-019-0479-0
35. Hancock, J. M.; Jenekhe, S. A. *Macromolecules* **2008,** *41,* 6864–6867. doi:10.1021/ma8016037
36. Kappaun, S.; Horner, S.; Kelterer, A.-M.; Waich, K.; Grasse, F.; Graf, M.; Romaner, L.; Niedermair, F.; Müllen, K.; Grimsdale, A. C.; Saf, R.; List, E. J. W.; Zojer, E.; Slugovc, C. *Macromol. Chem. Phys.* **2008,** *209,* 2122–2134. doi:10.1002/macp.200800386
37. Zalar, P.; Henson, Z. B.; Welch, G. C.; Bazan, G. C.; Nguyen, T.-Q. *Angew. Chem., Int. Ed.* **2012,** *51,* 7495–7498. doi:10.1002/anie.201202570
38. Yamaguchi, K.; Murai, T.; Guo, J.-D.; Sasamori, T.; Tokitoh, N. *ChemistryOpen* **2016,** *5,* 434–438. doi:10.1002/open.201600059
39. Su, S.-J.; Sasabe, H.; Takeda, T.; Kido, J. *Chem. Mater.* **2008,** *20,* 1691–1693. doi:10.1021/cm703682q
40. Achelle, S.; Robin-le Guen, F. *Tetrahedron Lett.* **2013,** *54,* 4491–4496. doi:10.1016/j.tetlet.2013.06.040
41. Fernandez-Cestau, J.; Bertrand, B.; Blaya, M.; Jones, G. A.; Penfold, T. J.; Bochmann, M. *Chem. Commun.* **2015,** *51,* 16629–16632. doi:10.1039/c5cc07523h
42. Zhang, Y.; Garcia-Amorós, J.; Captain, B.; Raymo, F. M. *J. Mater. Chem. C* **2016,** *4,* 2744–2747. doi:10.1039/c5tc03331d
43. Welch, G. C.; Bazan, G. C. *J. Am. Chem. Soc.* **2011,** *133,* 4632–4644. doi:10.1021/ja110968m
44. Huang, J.; Li, Y.; Wang, Y.; Meng, H.; Yan, D.; Jiang, B.; Wei, Z.; Zhan, C. *Dyes Pigm.* **2018,** *153,* 1–9. doi:10.1016/j.dyepig.2018.02.003
45. Li, Y.; Meng, H.; Li, Y.; Pang, B.; Luo, G.; Huang, J. *New J. Chem.* **2018,** *42,* 18961–18968. doi:10.1039/c8nj04453h
46. Quinn, J.; Guo, C.; Ko, L.; Sun, B.; He, Y.; Li, Y. *RSC Adv.* **2016,** *6,* 22043–22051. doi:10.1039/c5ra26227e
47. Yan, H.; Chen, J.; Zhou, K.; Tang, Y.; Meng, X.; Xu, X.; Ma, W. *Adv. Energy Mater.* **2018,** *8,* 1703672. doi:10.1002/aenm.201703672
48. Li, X.-C.; Wang, C.-Y.; Wan, Y.; Lai, W.-Y.; Zhao, L.; Yin, M.-F.; Huang, W. *Chem. Commun.* **2016,** *52,* 2748–2751. doi:10.1039/c5cc09752e

License and Terms

BEILSTEIN JOURNAL OF ORGANIC CHEMISTRY

Thermally activated delayed fluorescence (TADF) emitters: sensing and boosting spin-flipping by aggregation

Ashish Kumar Mazumdar, Gyana Prakash Nanda, Nisha Yadav, Upasana Deori, Upasha Acharyya, Bahadur Sk and Pachaiyappan Rajamalli*

Full Research Paper

Open Access

Address:
Materials Research Centre, Indian Institute of Science, C. V. Raman Road, Bangalore, Karnataka, 560012, India

Email:
Pachaiyappan Rajamalli* - rajamalli@iisc.ac.in

* Corresponding author

Keywords:
intramolecular charge transfer; molecular aggregates; sensing; thermally activated delayed fluorescence (TADF)

Beilstein J. Org. Chem. **2022,** *18,* 1177–1187.
https://doi.org/10.3762/bjoc.18.122

Received: 20 March 2022
Accepted: 19 August 2022
Published: 08 September 2022

This article is part of the thematic issue "Organic TADF materials design".

Guest Editor: E. Zysman-Colman

Abstract

Metal-free organic emitters with thermally activated delayed fluorescence (TADF) characteristics are emerging due to the potential applications in optoelectronic devices, time-resolved luminescence imaging, and solid-phase sensing. Herein, we synthesized two (4-bromobenzoyl)pyridine (BPy)-based donor–acceptor (D–A) compounds with varying donor size and strength: the emitter BPy-*p*TC with *tert*-butylcarbazole (TC) as the donor and BPy-*p*3C with bulky tricarbazole (3C) as the donor unit. Both BPy-*p*TC and BPy-*p*3C exhibited prominent emission with TADF properties in solution and in the solid phase. The stronger excited-state charge transfer was obtained for BPy-*p*3C due to the bulkier donor, leading to a more twisted D–A geometry than that of BPy-*p*TC. Hence, BPy-*p*3C exhibited aggregation-induced enhanced emission (AIEE) in a THF/water mixture. Interestingly, the singlet–triplet energy gap (ΔE_{ST}) was reduced for both compounds in the aggregated state as compared to toluene solution. Consequently, a faster reverse intersystem crossing rate (k_{RISC}) was obtained in the aggregated state, facilitating photon upconversion, leading to enhanced delayed fluorescence. Further, the lone-pair electrons of the pyridinyl nitrogen atom were found to be sensitive to acidic protons. Hence, the exposure to acid and base vapors using trifluoroacetic acid (TFA) and triethylamine (TEA) led to solid-phase fluorescence switching with fatigue resistance. The current study demonstrates the role of the donor strength and size in tuning ΔE_{ST} in the aggregated state as well as the relevance for fluorescence-based acid–base sensing.

Introduction

Metal-free organic solid-state emitters have gained increasing interest in recent years due to the potential applications in optoelectronic devices [1-4], solid-phase sensing [5], bioimaging [6,7], security [8], and storage devices [9]. The optical and electrochemical properties of the organic emitters can be tuned by external stimuli, such as mechanical force,

heat, solvent, acid and base fumes, etc. [10,11]. However, the fluorescence quantum yield of such emitters in the solid state is relatively low due to the aggregation-caused quenching (ACQ) effect [12-14] and limits practical applications. Hence, metal-free emitters with high photoluminescence quantum yield (PLQY) in solution and in the solid state and with multicolor tunability by external stimuli are crucial for task-specific applications.

Recently, donor–acceptor (D–A)-based organic emitters have shown tunable optical and electrochemical properties due to alteration of the intermolecular charge-transfer (ICT) interactions [15]. Several molecular designs were proposed to adjust the ICT interactions through covalent D–A linking. The separation of the highest occupied molecular orbital (HOMO) and the lowest unoccupied molecular orbital (LUMO) of the donor and acceptor molecules leads to a reduction of the singlet–triplet energy gap (ΔE_{ST}) [16,17]. The low ΔE_{ST} facilitates the exciton upconversion through reverse intersystem crossing (RISC) [2], which is commonly known as thermally activated delayed fluorescence (TADF) [16]. Theoretically, this has up to 100% internal quantum efficiency and could replace heavy metal-based emitters in organic light-emitting diode (OLED) devices [18]. Nevertheless, many TADF emitters suffer from quenching of the emission due to the aggregation-caused quenching effect [19,20]. The strong π–π-stacking interactions in the solid or aggregated state may lead to emission quenching. Therefore, an appropriate molecular design to suppress π–π stacking should help to obtain a strong emission in solution as well as in the solid state.

Solid-state organic emitters with reversible fluorescence switching are emerging for the sensing of pollutant acid vapor [21-23]. However, quickly detecting organic acid vapor at ambient conditions is challenging for solid-state detectors. Therefore, developing a solid-state emitter with reversible switching of the optical properties by external stimuli, such as acid and base vapors, is important. As per the recent literature, such sensors are being developed mainly by focusing on photophysical processes, such as photoinduced electron transfer (PET), excited-state intramolecular proton transfer (ESIPT), fluorescence resonance energy transfer (FRET), etc. [21,22,24,25]. Several literature reports have also demonstrated the switching of fluorescence in designing heteroatom-containing (N, O, S, etc.) chromophores [26]. The lone-pair electrons of heteroatoms can possess a certain degree of basicity, which results in sensitivity to acid. Consequently, the lone pair may be protonated and deprotonated by consecutively adding acid and base. The disruption of the molecular conjugation or ICT interactions upon protonation or deprotonation would lead to switching of the optical properties. While there are many reports on acid–based sensors, TADF emitter-based sensors are rare in the literature.

In this context, we chose the D–A molecular design to demonstrate the solid-phase acid–base sensing process and to determine the RISC rate (k_{RISC}). The selection of different donors with varying donor strength and size should help to understand the charge transfer (CT) interactions and D–A twist. Controlling the D–A twisting by varying the donor unit should be beneficial for suppressing nonradiative deactivation channels, leading to aggregated- or solid-state emission properties. To this end, we chose *tert*-butylcarbazole (TC) and bulky tricarbazole (3C), respectively, as donor unit in combination with a (4-bromobenzoyl)pyridine (BPy) acceptor core to demonstrate ΔE_{ST} tuning in solution and in an aggregated state, including the aggregation-induced enhanced emission (AIEE) characteristics. Further, solid-phase fluorescence switching by alternatingly adding acid and base vapors demonstrated the sensing ability. Therefore, the current study deciphers the role of molecular design and donor size in tuning ΔE_{ST} in an aggregated state and in fluorescence switching by acid–base addition.

Results and Discussion

Design and synthesis

Several BPy derivatives have been reported to lower ΔE_{ST} in D–A pairs to promote spin upconversion from the low-lying triplet excited state to the singlet state via RISC [17,27]. Heteroatom lone-pair electrons are sensitive to acid and, once protonated, to base, which would facilitate the tuning of optical properties in such media [21,22]. Herein, (4-(3,6-di-*tert*-butyl-9*H*-carbazol-9-yl)phenyl)(pyridin-4-yl)methanone (BPy-*p*TC) and (4-(9'*H*-[9,3':6',9''-tercarbazol]-9'-yl)phenyl)(pyridin-4-yl)methanone (BPy-*p*3C) were synthesized via Ullmann coupling following the reported protocol [28]. These two TADF emitters have already been synthesized and device fabrication had been demonstrated. However, detailed photophysical investigations in the aggregated state have not yet been performed [28]. The acceptor core BPy, coupled with carbazole derivatives, produced BPy-*p*TC and BPy-*p*3C, respectively (Scheme 1). The detailed synthetic procedures and characterization data are given in the Experimental section and in Schemes S1 and S2 in Supporting Information File 1. Both compounds were further purified by temperature-gradient vacuum sublimation and characterized by ^{1}H and ^{13}C NMR spectroscopy (Figures S9–S12, Supporting Information File 1) as well as high-resolution mass spectrometry.

Photophysical studies and DFT calculations

The UV–vis absorption and emission spectra of BPy-*p*TC and BPy-*p*3C were recorded in solvents with varying polarity (Figure 1 and Table 1). BPy-*p*TC exhibited prominent absorp-

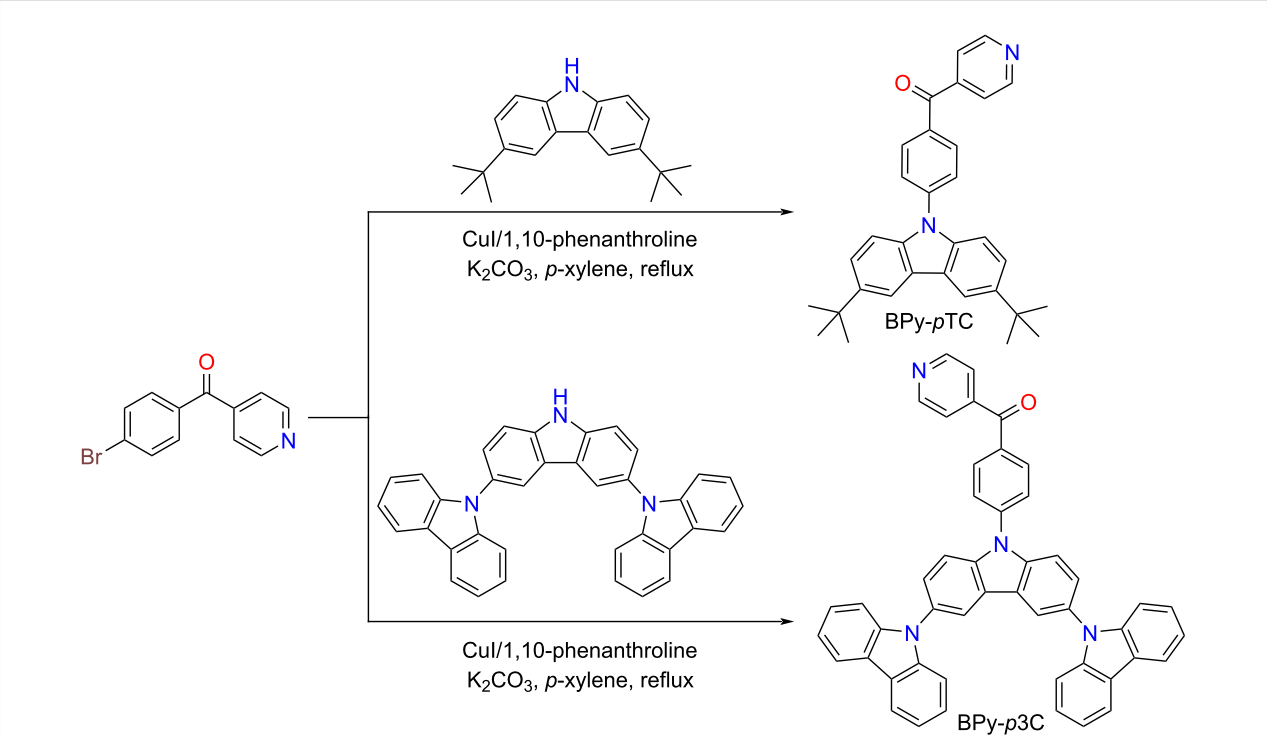

Scheme 1: Synthetic schemes of BPy-*p*TC and BPy-*p*3C.

tion bands at λ_{abs} = 337, 355, and 383 nm. The peaks at λ_{abs} = 337 and 335 nm were due to the π–π* and n–π* transitions [29], whereas the broad peak at λ_{abs} = 383 nm was due to the ICT transitions. Similarly, three peaks centered at λ_{abs} = 336, 350, and 368 nm were observed for BPy-*p*3C. The ICT band of BPy-*p*3C (λ_{abs} = 368 nm) was blue-shifted as compared to BPy-*p*TC (λ_{abs} = 383 nm) due to the weaker ground state CT interactions. As a result, a stronger molar extinction coefficient was obtained for the CT band in BPy-*p*TC ($\varepsilon_{373\ nm}$ = 17310 $M^{-1}{\cdot}cm^{-1}$) as compared to BPy-*p*3C ($\varepsilon_{365\ nm}$ = 14690 $M^{-1}{\cdot}cm^{-1}$).

Computational calculations were performed to understand the ground state electronic communication between the donor and acceptor in BPy-*p*TC and BPy-*p*3C using the Gaussian 16 program package (Figure S1 as well as Tables S1 and S2 in Supporting Information File 1). The LUMO of both compounds was predominantly located on the acceptor core, whereas the HOMO was distributed mainly over the donor unit for both compounds and extended to the adjacent phenyl π-spacer ring only for BPy-*p*TC (Figure S1, Supporting Information File 1). As a consequence, a higher oscillator strength (f = 0.213) was obtained for BPy-*p*TC as compared to BPy-*p*3C (f = 0.073, Table S1, Supporting Information File 1). Additionally, a 48° and 51° (59° for the second donor and overall D–A dihedral = 97°) D–A dihedral angle was obtained for BPy-*p*TC and BPy-*p*3C, respectively (Figure S1, Supporting Information File 1). Therefore, the coplanarity between the D–A linkage in BPy-*p*TC facilitated the prominent ground-state communication from the donor to the acceptor core, as compared to the twisted BPy-*p*3C (Figure S1, Supporting Information File 1) [30].

The steady-state emission of both BPy-*p*TC and BPy-*p*3C was recorded in different polar media (Figure 1c and Figure 1d). The BPy-*p*TC emission lay in the cyan region, and the peak was centered at λ_{em} = 476 nm in toluene (Figure 1b). The emission spectra of BPy-*p*TC were red-shifted in polar media, and the emission maxima changed from λ_{em} = 476 nm in toluene to λ_{em} = 497 nm in THF and to λ_{em} = 545 nm in DCM (Figure 1c). Similarly, blue emission was observed in toluene at λ_{em} = 488 nm for BPy-*p*3C, and it red-shifted to λ_{em} = 530 nm in THF and to λ_{em} = 582 nm in polar DCM (Figure 1d). As compared to the absorption spectra, the significant solvatochromic shifts in the fluorescence spectra suggested the presence of a highly dipolar excited state with a stronger ICT character, in contrast to the ground state of the molecule. But the Stokes shift of BPy-*p*3C ($\overline{\Delta\upsilon}$ = 6640 cm^{-1} in toluene and $\overline{\Delta\upsilon}$ = 9991 cm^{-1} in DCM) was always higher than that of BPy-*p*TC ($\overline{\Delta\upsilon}$ = 5145 cm^{-1} in toluene and $\overline{\Delta\upsilon}$ = 7761 cm^{-1} in DCM) in all polar media, indicating a highly dipolar excited state (Figure 1c and Figure 1d as well as Tables S3 and S4 in

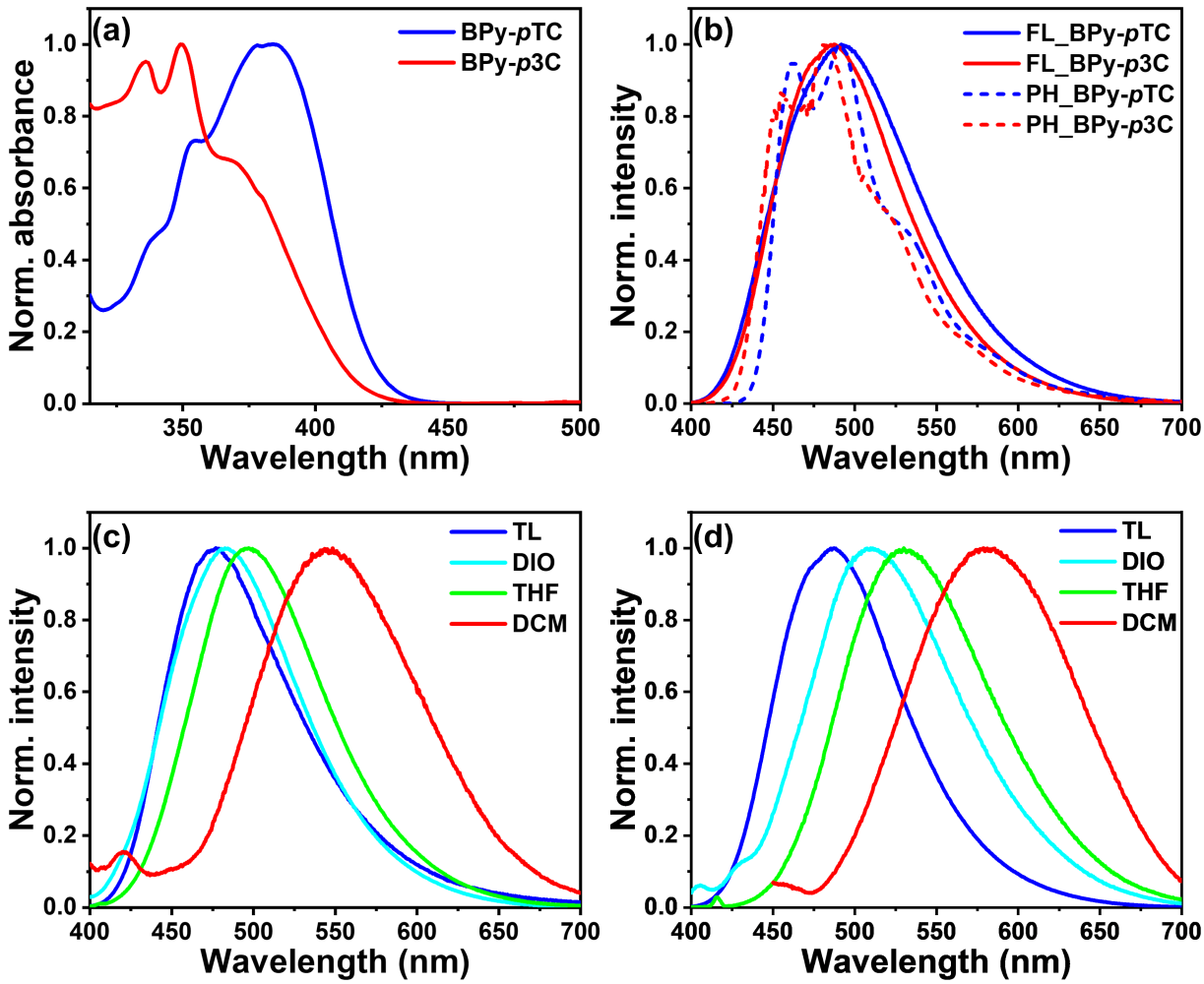

Figure 1: (a) Normalized absorption spectra of BPy-*p*TC and BPy-*p*3C in toluene at room temperature; (b) normalized fluorescence (λ_{ex} = 375 nm, 10 μM in toluene) spectra at ambient temperature and phosphorescence spectra (λ_{ex} = 375 nm, 10 μM) of BPy-*p*TC and BPy-*p*3C at 77 K; emission spectra (λ_{ex} = 375 nm) of BPy-*p*TC (c) and BPy-*p*3C (d) in various polar solvents. (TL: toluene, DIO: 1,4-dioxane, THF: tetrahydrofuran, DCM: dichloromethane).

Table 1: Photophysical properties of BPy-*p*TC and BPy-*p*3C.[a]

compound	λ_{em} (nm)	τ^{PF} (ns)	τ^{DF} (μs)	Φ_{total} (%)	ΔE_{ST} (eV)
BPy-*p*TC	476	6.5	0.5	19	0.121
BPy-*p*3C	488	5.1	0.4	26	0.047

[a]Measured in degassed toluene (10 μM).

Supporting Information File 1). The large Stokes shift and spectral broadening indicated a highly polarized ICT state in both compounds (Figure 1c and Figure 1d as well as Tables S3 and S4 in Supporting Information File 1) [30]. The excited-state CT characteristics were further probed using the Lippert–Mataga plot for both the compounds (Figure S2 and Tables S3–S5 in Supporting Information File 1) [29]. A larger Stokes shift and transient dipole ($\mu_E - \mu_G$) than in BPy-*p*TC were observed in BPy-*p*3C (Table S5, Supporting Information File 1). This indicated the relatively stronger excited-state CT interactions in BPy-*p*3C (Figure 1c and Figure 1d as well as Tables S3–S5 in Supporting Information File 1).

The phosphorescence spectra of BPy-*p*TC and BPy-*p*3C were recorded in toluene at 77 K (Figure 1b). The structural phosphorescence bands were obtained for both compounds. The nature of the phosphorescence bands indicated the locally excited (^{3}LE) character of the T_1 state. The onset of the fluorescence spectrum (energy of S_1) in toluene at room temperature and the onset of the phosphorescence spectrum (energy of T_1) in toluene at 77 K was chosen to estimate the ΔE_{ST} values of the emitters (Figure 1b) [31]. A smaller singlet–triplet splitting was observed for BPy-*p*3C (ΔE_{ST} = 0.047 eV) as compared to BPy-*p*TC (ΔE_{ST} = 0.121 eV) due to the twisted molecular geometry (Figure 1 and Table 1). The small ΔE_{ST} values indicated a possible RISC process from the T_1 to the S_1 state for both the compounds. The photophysical properties of both the emitters in toluene are summarized in Table 1.

Time-resolved spectroscopy

Further, the fluorescence lifetimes on the nanosecond and microsecond timescales of both emitters were recorded in degassed THF to understand the photon upconversion process (Figure 2 and Tables S6 and S7 in Supporting Information File 1). Emission decay on the nanosecond and microsecond timescales was obtained for BPy-*p*TC, with decay lifetimes of 6.2 ns and 5.8 µs, respectively (Figure 2a as well as Table S6 in Supporting Information File 1). In comparison, a biexponential fluorescence decay with average lifetimes of τ_{avg} = 3.5 ns and 6.6 ns was obtained for BPy-*p*3C (Figure 2b as well as Table S7 in Supporting Information File 1). The short component was due to the prompt fluorescence (PF), and the long component was the delayed fluorescence (DF) [32]. Hence, both emitters displayed prominent DF due to the small ΔE_{ST}, facilitating the photon upconversion from the T_1 to the S_1 state through an RISC process.

Aggregation-induced enhanced emission (AIEE)

In order to determine the molecular aggregate formation of BPy-*p*TC and BPy-*p*3C and the impact on the optical properties, we carried out aggregation studies in THF/water mixtures (Figure 3) [33]. BPy-*p*TC emits in the blue-green region at λ_{em} = 497 nm in THF with a PLQY of 12.7% (Figure 3a). The emission intensity was reduced to near 0 upon increasing the water fraction from 10 to 70 vol % in the THF solution of BPy-*p*TC (Figure 3a and Figure 3c). The formation of a dark twisted intramolecular CT state led to fluorescence quenching in the highly polar water/THF mixture (10–70 vol % water, Figure 3a, c, and e) [34-36]. It again started glowing when the water fraction was increased beyond 80 vol % (Figure 3a, c, and e). The formation of molecular aggregates in >80 vol % water/THF mixtures led to the regaining of fluorescence in BPy-*p*TC (Figure 3a, c, e, and f). A slight blue shift was also observed in 80–90 vol % water/THF mixtures of BPy-*p*TC due to restriction of D–A rotation in the aggregated state, which led to diminished CT [34]. The nanoaggregates (in 90 vol % water/THF) of BPy-*p*TC were characterized using scanning electron microscopy (SEM). The SEM image showed the spherical nanoaggregates of BPy-*p*TC, with 95 nm diameter (Figure 3f). The BPy-*p*3C compound emitted in the green region at λ_{em} = 530 nm in THF, with a PLQY of 3.6% (Figure 3a). Similar to BPy-*p*TC, for BPy-*p*3C, a dark state in 10–70 vol % water/THF mixtures and emissive aggregates in 80–90 vol % water/THF mixtures were obtained (Figure 3b, d, and e). Interestingly, AIEE was obtained only for BPy-*p*3C in a 90 vol % water/THF mixture (Figure 3e).

The bulky donor group in BPy-*p*3C led to facile D–A rotation in solution. As a result, we observed the twisted molecular geometry and a lower PLQY of 3.6% as compared to rigid BPy-

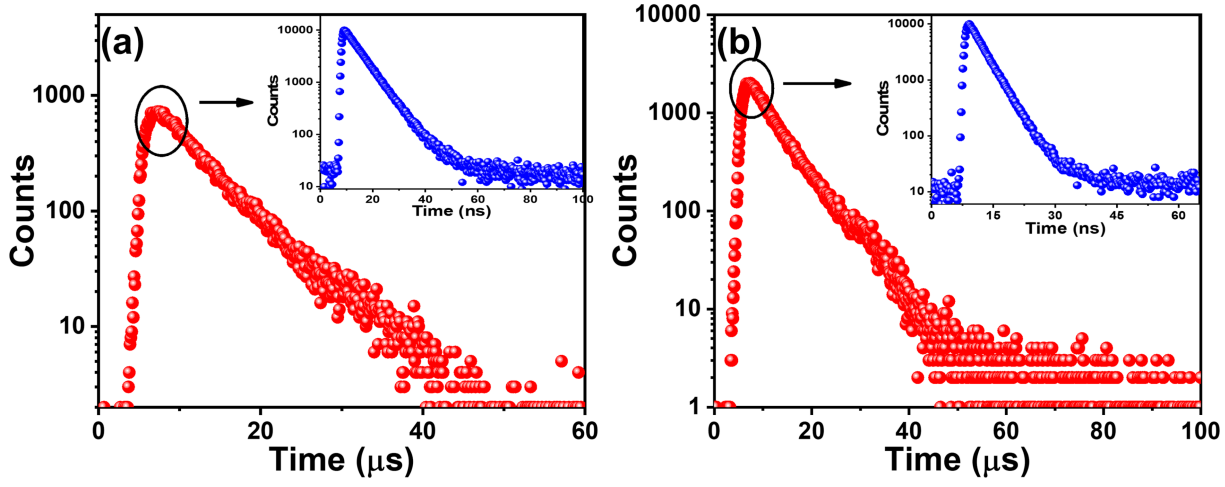

Figure 2: Transient photoluminescence decay (λ_{ex} = 375 nm) of (a) BPy-*p*TC and (b) BPy-*p*3C in degassed THF (10 µM) at room temperature.

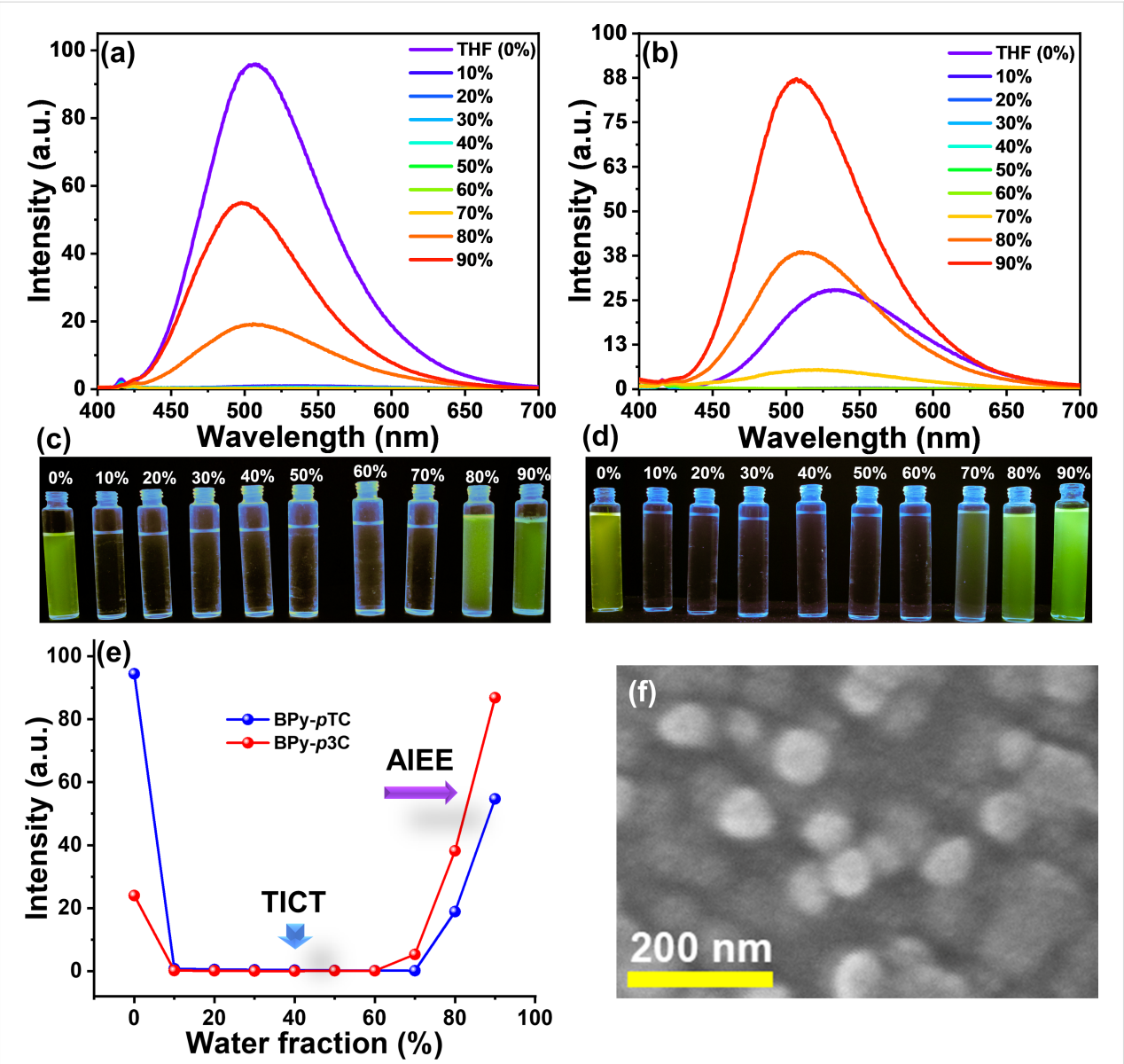

Figure 3: AIEE studies: Emission spectra (λ_{ex} = 375 nm, 10 μM) of (a) BPy-*p*TC and (d) BPy-*p*3C in THF with increasing water fraction (in vol %) at room temperature. Digital photographs of (c) BPy-*p*TC and (d) BPy-*p*3C in THF/water solutions under exposure to a UV lamp (λ_{ex} = 365 nm). (e) Plot of PL intensity vs water fraction of BPy-*p*TC and BPy-*p*3C depicting the AIEE phenomenon in BPy-*p*3C. (f) SEM image of BPy-*p*TC aggregates formed in a 90 vol % water/THF mixture.

*p*TC (PLQY = 12.7%) in THF solution. In contrast to the THF solution, BPy-*p*3C showed enhanced PLQY from 3.6% to 9.8% in an aggregated state, while BPy-*p*TC showed reduced PLQY from 12.7% in THF solution to 7.0% in the aggregated state. The enhanced emission in the aggregated state of BPy-*p*3C as compared to the THF solution was due to the restricted D–A rotation in the aggregated state [21]. As revealed from the photophysical studies and DFT calculations, BPy-*p*3C has a twisted molecular geometry with a stronger excited-state ICT than BPy-*p*TC. As a consequence, it facilitates nonradiative deactivation pathways in solution due to molecular vibrations and facile D–A rotation, as compared to rigid BPy-*p*TC (strong ground-state CT interactions render the D–A complex rigid). In comparison, due to the ground-state D–A communication on the basis of a +R effect, the weak excited-state CT interactions and rigid molecular geometry in BPy-*p*TC led to the regain of fluorescence in the aggregated state [30]. However, the fluorescence intensity of aggregates of BPy-*p*TC did not reach beyond the native THF solution. Another factor that may have been responsible for this were the π–π-stacking interactions in the aggregated or solid phase of BPy-*p*TC as compared to twisted BPy-*p*3C [36].

To determine the effect of aggregation on the spin-flipping process (indicated by k_{RISC}) from the low-lying triplet state T_1 to the singlet excited state S_1, we recorded the fluorescence and phosphorescence spectra of aggregates (90 vol % water/THF) at room temperature and 77 K, respectively (Figure 4). The structural phosphorescence band was obtained from the aggregates in 90 vol % water/THF mixtures (Figure 4). Additionally, the phosphorescence spectra of both compounds were recorded in THF at 77 K (Figure S3 in Supporting Information File 1). The retention of the structural phosphorescence band in THF indicates its origin from the locally excited triplet state ^{3}LE. The ΔE_{ST} values calculated based on the onset of the fluorescence and the phosphorescence spectra of BPy-*p*TC and BPy-*p*3C in 90 vol % water/THF were 0.06 and −0.047 eV, respectively (Figure 4). The ΔE_{ST} values were lower in the aggregated state than in solution for both compounds (ΔE_{ST} in toluene for BPy-*p*TC and BPy-*p*3C = 0.121 and 0.047 eV, respectively), which indicated aggregation-induced RISC boosting. BPy-*p*3C showed a negative ΔE_{ST} value because the phosphorescence emission came from the locally excited triplet states (^{3}LE-structured emission), not from the ^{3}CT state [37]. This low ΔE_{ST} value facilitates fast spin-flipping in the aggregated state. Consequently, a fast k_{RISC} rate ($0.74{\cdot}10^5$ s^{-1} for BPy-*p*TC and $2.06{\cdot}10^5$ s^{-1} for BPy-*p*3C) was obtained in the aggregated state (Table 2). Interestingly, a higher reduction of ΔE_{ST} as compared to BPy-*p*TC was obtained for the aggregates of BPy-*p*3C. This could have been due to the locking of the twisted molecular geometry in the aggregated state and more dipolar excited states in the highly polar water/THF mixtures.

Further, the PF and DF lifetimes of the aggregates of BPy-*p*TC and BPy-*p*3C were measured in degassed solutions (Figure 5 and Table 2). We found an over 1.5- and 3-fold enhancement of the PF and DF lifetimes, respectively, for BPy-*p*TC in the aggregated state as compared to the THF solutions (Figure 5a and Table 2). However, only the PF lifetime was enhanced in BPy-*p*3C (3.5-fold), and no significant change was obtained in the DF lifetime of the aggregates (Figure 5b and Table 2). Therefore, it is evident that the aggregation helped to suppress the fluorescence quenching as well as to boost the DF by reducing the ΔE_{ST} in BPy-*p*TC. At the same time, the significant enhancement of the PF lifetime was due to the molecular rigidification and restriction of D–A rotation in BPy-*p*3C aggre-

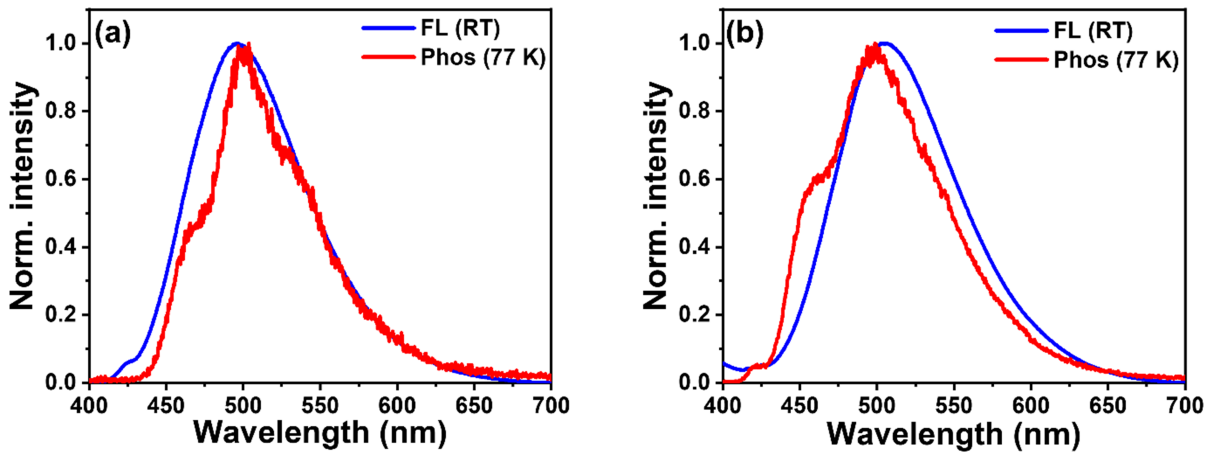

Figure 4: Normalized fluorescence at room temperature and phosphorescence spectra at 77 K (λ_{ex} = 375 nm, 10 μM) of (a) BPy-*p*TC and (b) BPy-*p*3C aggregates in 90 vol % water/THF mixture.

Table 2: Photophysical properties of BPy-*p*TC and BPy-*p*3C aggregates.

compound	sample	λ_{em}[a] (nm)	ΔE_{ST}[a] (eV)	τ^{PF} (ns)	τ^{DF} (μs)	Φ_{total} (%)	Φ_{PF} (%)	Φ_{DF} (%)	k_r (10^7 s^{-1})	k_{ISC} (10^7 s^{-1})	k_{RISC} (10^5 s^{-1})	$k_{nr,S}$ (10^7 s^{-1})
BPy-*p*TC	90 vol % water/THF	496	0.06	9.0	19.1	7.0	4.8	2.2	0.5	0.36	0.74	6.9
BPy-*p*3C	90 vol % water/THF	505	−0.047	19.2	6.8	9.8	6.8	3.3	0.4	0.18	2.06	3.2

[a]Measured in 90 vol % water/THF mixture.

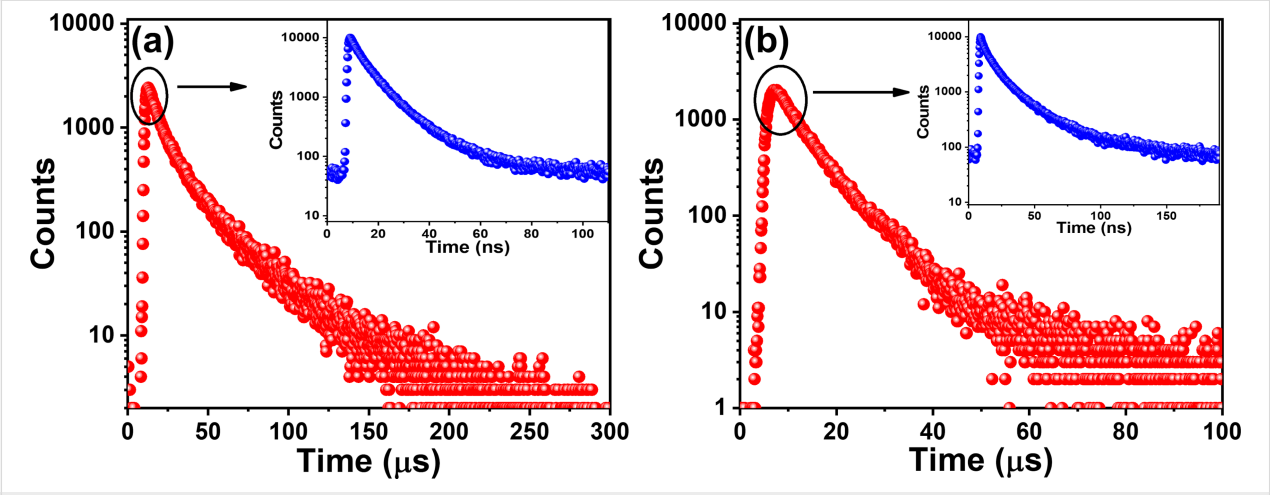

Figure 5: Transient photoluminescence decay (λ_{ex} = 375 nm, 20 μM) of (a) BPy-*p*TC and (b) BPy-*p*3C aggregates in 90 vol % water/THF mixture.

gates. Thus, a judicious choice of D–A molecular architecture is necessary to tune the solid- or aggregated-state optical properties for triplet harvesting.

Fluorescence switching

The lone-pair electrons of heteroatoms, such as oxygen and nitrogen, are susceptible to acidic protons [22]. BPy-*p*TC and BPy-*p*3C exhibit lone-pair electrons at the pyridinyl nitrogen atom and show prominent emission in the solid and aggregated states. We therefore demonstrated the switching of fluorescence using acid and base vapors in neat film (Figure 6a and Figure 6c). Both emitters exhibited switching of the fluorescence responses upon exposure to acidic and basic fumes on neat film (Figure 6a and Figure 6c). The intense green emission of the BPy-*p*TC film turned dark upon exposure to trifluoroacetic acid (TFA) vapor for 4 s (Figure 6a). The green fluorescence reappeared after neutralization with triethylamine (TEA) vapor for 6 s (Figure 6a). The reversible color switching was upheld with fatigue resistance for multiple cycles. Similarly, the film of BPy-*p*3C showed reversible changes of the fluorescence from green to dark upon successive exposure to TFA and TEA vapors (Figure 6c).

To understand the effect of an acidic solution on the optical properties, we carried out the same experiment in toluene solution (Figure 6b and Figure 6d). The protonation of the pyridinyl nitrogen atom upon addition of TFA quenched the fluorescence of both compounds (Figure 6b and Figure 6d). In turn, neutralization of the toluene solution by TEA or KOH addition led to the regain of fluorescence (Figure 6b and Figure 6d). Further, the Stern–Volmer plots were analyzed for both compounds to obtain the quenching and recovery constants (Figures S4 and S5 in Supporting Information File 1). The linear fitted Stern–Volmer plots for quenching and recovery were obtained for both compounds upon addition of acid and base. Thereby, the protonation–deprotonation events were confirmed using absorption spectroscopy (Figure S6, Supporting Information File 1). The new peak at λ_{abs} = 425 nm in the absorption spectrum of BPy-*p*TC upon adding TFA, indicated the protonation of the pyridinyl nitrogen atom (Figure S6a, Supporting Information File 1). This enhanced the electron-deficient character of the BPy acceptor core and the ground-state communication between the donor and acceptor units. As a result, the red-shifted CT absorption band in the acidic medium was obtained (Figure S6a in Supporting Information File 1). The absorption spectra upon addition of TEA again matched with the absorption spectra in toluene (Figure S6a, Supporting Information File 1).

Further, TDDFT calculations for a protonated pyridinyl nitrogen atom (N–H) and carbonyl oxygen atom (CO–H) were performed in comparison to neutral BPy-*p*TC to determine the protonation site (Figure S7 in Supporting Information File 1). The computed absorption band of BPy-*p*TC and protonated pyridinyl resembled the change observed experimentally (Figures S6 and S7 in Supporting Information File 1). Additionally, the ^{1}H NMR study upon the addition of TFA in BPy-*p*TC suggested protonation of the pyridinyl nitrogen atom (Figure S8, Supporting Information File 1). Thus, the facile protonation of the pyridinyl nitrogen atom affected the optical properties of both compounds. The reversible change of absorption and emission by successive addition of acid and base in solution as well as in the solid state indicated that both compounds are suitable for acid sensing in solution and in the solid phase. Reversible fluorescence for thin emitter films was observed in the presence of TFA and TEA. Essentially, quenching occurs in the presence of acid and regaining of the fluorescence intensity happens under basic conditions (Figure 7).

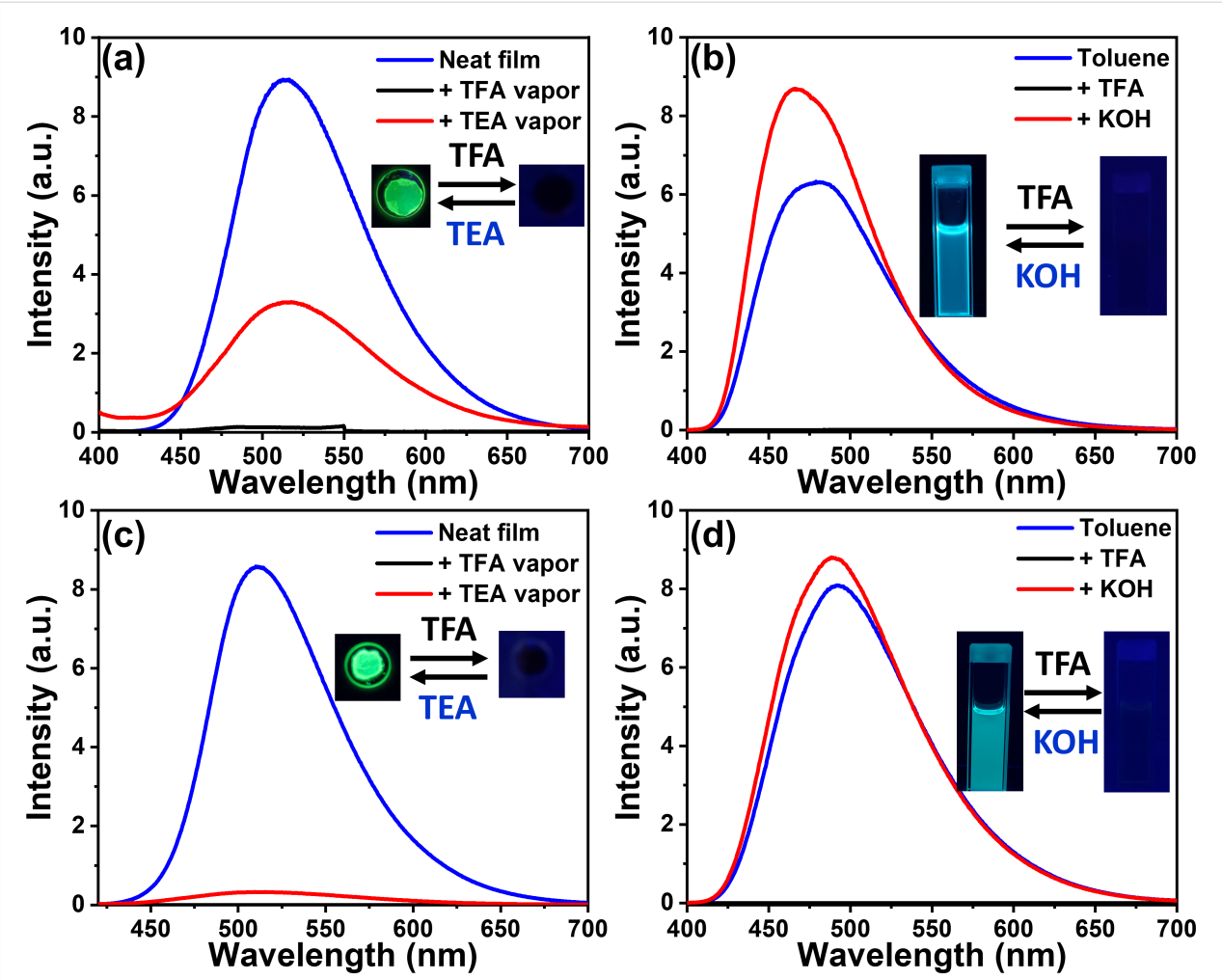

Figure 6: Fluorescence switching by acid and base fumes exposure: Emission spectra (λ_{ex} = 375 nm) of (a) BPy-*p*TC and (c) BPy-*p*3C in neat film upon exposure to TFA and TEA vapor at room temperature. Fluorescence switching by addition of TFA and KOH to (b) BPy-*p*TC and (d) BPy-*p*3C in toluene solution.

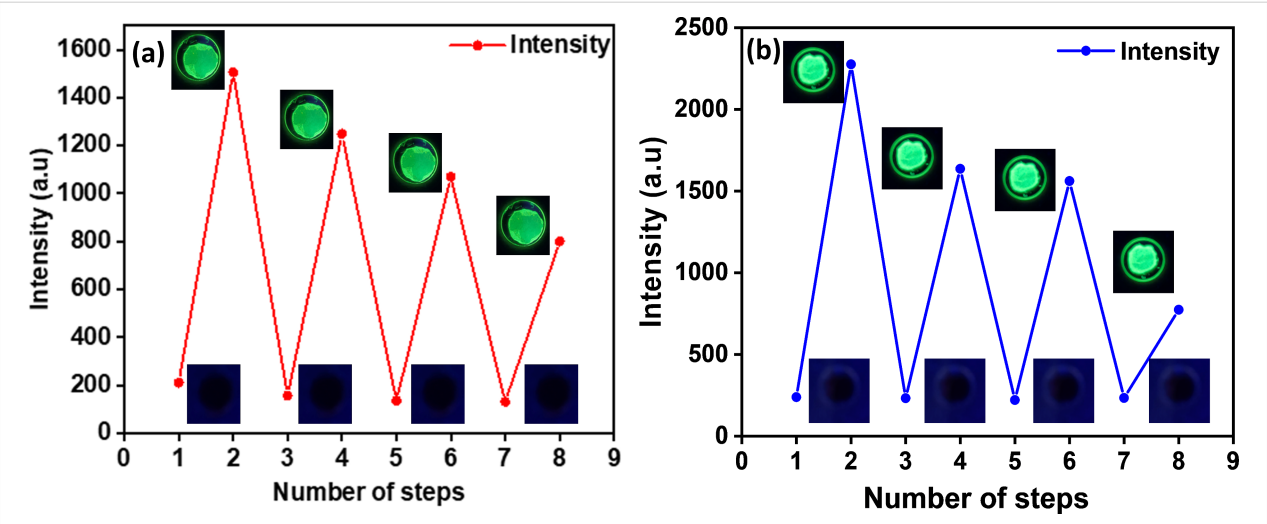

Figure 7: Fluorescence intensity vs number of exposures for (a) BPy-p3C and (b) BPy-pTC thin films upon exposure to TFA and TEA vapors.

Conclusion

In summary, we designed and synthesized two D–A-based TADF emitters, BPy-*p*TC and BPy-*p*3C. Both emitters showed excited-state ICT characteristics, leading to positive solvatochromism in solution. The Lippert–Mataga plot and DFT calculations indicated that BPy-*p*3C had more excited-state CT properties than BPy-*p*TC due to the bulkier donor group. Both compounds displayed strong emission in the aggregated state in a highly polar medium (80–90 vol % water/THF mixtures). As compared to the native solution, BPy-*p*3C showed AIEE. Moreover, as compared to the solution, ΔE_{ST} was reduced in the aggregated form. Consequently, a fast RISC rate was obtained for the aggregates of both compounds. Further, these two TADF emitters were used to demonstrate solid-state fluorescence switching upon exposure to TFA and TEA vapors. The current study helps to understand the enhancement of DF in the aggregated state, which is important for the fabrication of efficient OLED devices and reversible switching of fluorescence by acid–base exposure.

Supporting Information

Supporting Information File 1

General information, synthesis and characterization data including NMR spectra, computational details, UV–vis data, Lippert–Mataga plot, and acid–base switching.
[https://www.beilstein-journals.org/bjoc/content/supplementary/1860-5397-18-122-S1.pdf]

Funding

A. K. M. is grateful to the Prime Minister's Research Fellowship (PMRF), Ministry of Education, Government of India (Application No: PMRF-2122-3210) for fellowship support, and G. P. N. thanks the Council of Scientific & Industrial Research (CSIR) India for the Junior Research Fellowship (JRF). Bahadur thanks the Indian Institute of Science (IISc) Bangalore, India, for C. V. Raman Fellowship. U. D. and N. Y. thank IISc for doctoral fellowship. P. R. thanks IISc for generous financial support and the Science & Engineering Research Board (SERB), India, for the SERB-Power Grant (SPG, Grant No: SPG/2020/000107). P. R. also acknowledges Rekha Rao Young Investigator award (2022-24) for the financial support.

ORCID® iDs

Ashish Kumar Mazumdar - https://orcid.org/0000-0001-6627-0108
Gyana Prakash Nanda - https://orcid.org/0000-0002-4592-5758
Nisha Yadav - https://orcid.org/0000-0003-2796-6086
Upasana Deori - https://orcid.org/0000-0002-7271-7559
Upasha Acharyya - https://orcid.org/0000-0002-5070-2428
Bahadur Sk - https://orcid.org/0000-0002-7098-5429
Pachaiyappan Rajamalli - https://orcid.org/0000-0001-8079-0425

References

1. Liu, Y.; Li, C.; Ren, Z.; Yan, S.; Bryce, M. R. *Nat. Rev. Mater.* **2018,** *3,* 18020. doi:10.1038/natrevmats.2018.20
2. Data, P.; Takeda, Y. *Chem. – Asian J.* **2019,** *14,* 1613–1636. doi:10.1002/asia.201801791
3. Rajamalli, P.; Senthilkumar, N.; Huang, P.-Y.; Ren-Wu, C.-C.; Lin, H.-W.; Cheng, C.-H. *J. Am. Chem. Soc.* **2017,** *139,* 10948–10951. doi:10.1021/jacs.7b03848
4. Wong, M. Y.; Zysman-Colman, E. *Adv. Mater. (Weinheim, Ger.)* **2017,** *29,* 1605444. doi:10.1002/adma.201605444
5. Zhou, Y.; Qin, W.; Du, C.; Gao, H.; Zhu, F.; Liang, G. *Angew. Chem., Int. Ed.* **2019,** *58,* 12102–12106. doi:10.1002/anie.201906312
6. Xiong, X.; Song, F.; Wang, J.; Zhang, Y.; Xue, Y.; Sun, L.; Jiang, N.; Gao, P.; Tian, L.; Peng, X. *J. Am. Chem. Soc.* **2014,** *136,* 9590–9597. doi:10.1021/ja502292p
7. Zhang, K. Y.; Yu, Q.; Wei, H.; Liu, S.; Zhao, Q.; Huang, W. *Chem. Rev.* **2018,** *118,* 1770–1839. doi:10.1021/acs.chemrev.7b00425
8. Sk, B.; Sharma, S.; James, A.; Kundu, S.; Patra, A. *J. Mater. Chem. C* **2020,** *8,* 12943–12950. doi:10.1039/d0tc02520h
9. Cafferty, B. J.; Ten, A. S.; Fink, M. J.; Morey, S.; Preston, D. J.; Mrksich, M.; Whitesides, G. M. *ACS Cent. Sci.* **2019,** *5,* 911–916. doi:10.1021/acscentsci.9b00210
10. Paisley, N. R.; Tonge, C. M.; Hudson, Z. M. *Front. Chem. (Lausanne, Switz.)* **2020,** *8,* 229. doi:10.3389/fchem.2020.00229
11. Huang, L.; Qian, C.; Ma, Z. *Chem. – Eur. J.* **2020,** *26,* 11914–11930. doi:10.1002/chem.202000526
12. Förster, T.; Kasper, M. *Z. Phys. Chem.* **1954,** *1,* 275–277. doi:10.1524/zpch.1954.1.5_6.275
13. Ma, X.; Sun, R.; Cheng, J.; Liu, J.; Gou, F.; Xiang, H.; Zhou, X. *J. Chem. Educ.* **2016,** *93,* 345–350. doi:10.1021/acs.jchemed.5b00483
14. Li, Q.; Li, Z. *Adv. Sci.* **2017,** *4,* 1600484. doi:10.1002/advs.201600484
15. Sasaki, S.; Drummen, G. P. C.; Konishi, G.-i. *J. Mater. Chem. C* **2016,** *4,* 2731–2743. doi:10.1039/c5tc03933a
16. Uoyama, H.; Goushi, K.; Shizu, K.; Nomura, H.; Adachi, C. *Nature* **2012,** *492,* 234–238. doi:10.1038/nature11687
17. Rajamalli, P.; Thangaraji, V.; Senthilkumar, N.; Ren-Wu, C.-C.; Lin, H.-W.; Cheng, C.-H. *J. Mater. Chem. C* **2017,** *5,* 2919–2926. doi:10.1039/c7tc00457e
18. Tao, Y.; Yuan, K.; Chen, T.; Xu, P.; Li, H.; Chen, R.; Zheng, C.; Zhang, L.; Huang, W. *Adv. Mater. (Weinheim, Ger.)* **2014,** *26,* 7931–7958. doi:10.1002/adma.201402532
19. Tsujimoto, H.; Ha, D.-G.; Markopoulos, G.; Chae, H. S.; Baldo, M. A.; Swager, T. M. *J. Am. Chem. Soc.* **2017,** *139,* 4894–4900. doi:10.1021/jacs.7b00873
20. Chen, H.; Liu, H.; Xiong, Y.; He, J.; Zhao, Z.; Tang, B. Z. *Mater. Chem. Front.* **2022,** *6,* 924–932. doi:10.1039/d1qm01625c
21. Yang, Z.; Qin, W.; Lam, J. W. Y.; Chen, S.; Sung, H. H. Y.; Williams, I. D.; Tang, B. Z. *Chem. Sci.* **2013,** *4,* 3725–3730. doi:10.1039/c3sc50648g
22. Steinegger, A.; Wolfbeis, O. S.; Borisov, S. M. *Chem. Rev.* **2020,** *120,* 12357–12489. doi:10.1021/acs.chemrev.0c00451

23. Fan, S.; Dennison, G. H.; FitzGerald, N.; Burn, P. L.; Gentle, I. R.; Shaw, P. E. *Commun. Chem.* **2021,** *4,* 45. doi:10.1038/s42004-021-00482-6
24. Chen, L.; Fu, P.-Y.; Wang, H.-P.; Pan, M. *Adv. Opt. Mater.* **2021,** *9,* 2001952. doi:10.1002/adom.202001952
25. Zhang, Q.; Yang, L.; Han, Y.; Wang, Z.; Li, H.; Sun, S.; Xu, Y. *Chem. Eng. J.* **2022,** *428,* 130986. doi:10.1016/j.cej.2021.130986
26. Putra, A. U.; Çakmaz, D.; Seferoğlu, N.; Barsella, A.; Seferoğlu, Z. *Beilstein J. Org. Chem.* **2020,** *16,* 2282–2296. doi:10.3762/bjoc.16.189
27. Rajamalli, P.; Senthilkumar, N.; Gandeepan, P.; Ren-Wu, C.-Z.; Lin, H.-W.; Cheng, C.-H. *J. Mater. Chem. C* **2016,** *4,* 900–904. doi:10.1039/c5tc03943f
28. Rajamalli, P.; Senthilkumar, N.; Gandeepan, P.; Ren-Wu, C.-C.; Lin, H.-W.; Cheng, C.-H. *ACS Appl. Mater. Interfaces* **2016,** *8,* 27026–27034. doi:10.1021/acsami.6b10678
29. Lakowicz, J. R., Ed. *Principles of fluorescence spectroscopy,* 3rd ed.; Springer Science and Business Media: New York, NY, USA, 2006. doi:10.1007/978-0-387-46312-4
30. Sk, B.; Khodia, S.; Patra, A. *Chem. Commun.* **2018,** *54,* 1786–1789. doi:10.1039/c7cc09261j
31. Ward, J. S.; Kukhta, N. A.; dos Santos, P. L.; Congrave, D. G.; Batsanov, A. S.; Monkman, A. P.; Bryce, M. R. *Chem. Mater.* **2019,** *31,* 6684–6695. doi:10.1021/acs.chemmater.9b01184
32. Sk, B.; Ravindran, E.; Deori, U.; Yadav, N.; Nanda, G. P.; Rajamalli, P. *J. Mater. Chem. C* **2022,** *10,* 4886–4893. doi:10.1039/d1tc05027c
33. Thulaseedharan Nair Sailaja, S.; Maisuls, I.; Kösters, J.; Hepp, A.; Faust, A.; Voskuhl, J.; Strassert, C. A. *Beilstein J. Org. Chem.* **2020,** *16,* 2960–2970. doi:10.3762/bjoc.16.246
34. Wang, J.; Zhang, J.; Jiang, C.; Yao, C.; Xi, X. *ACS Appl. Mater. Interfaces* **2021,** *13,* 57713–57724. doi:10.1021/acsami.1c17449
35. Wang, Y.-F.; Liu, X.; Zhu, Y.; Li, M.; Chen, C.-F. *J. Mater. Chem. C* **2022,** *10,* 4805–4812. doi:10.1039/d1tc04893g
36. Wang, J.; Yang, Y.; Jiang, C.; He, M.; Yao, C.; Zhang, J. *J. Mater. Chem. C* **2022,** *10,* 3163–3171. doi:10.1039/d1tc05497j
37. Noda, H.; Nakanotani, H.; Adachi, C. *Sci. Adv.* **2018,** *4,* eaao6910. doi:10.1126/sciadv.aao6910

License and Terms

BEILSTEIN JOURNAL OF ORGANIC CHEMISTRY

Ionic multiresonant thermally activated delayed fluorescence emitters for light emitting electrochemical cells

Merve Karaman[1,2], Abhishek Kumar Gupta[2,3], Subeesh Madayanad Suresh[2], Tomas Matulaitis[2], Lorenzo Mardegan[4], Daniel Tordera[*4], Henk J. Bolink[4], Sen Wu[2], Stuart Warriner[5], Ifor D. Samuel[3] and Eli Zysman-Colman[*2]

Full Research Paper

Open Access

Address:
[1]Department of Material Science and Engineering, Faculty of Engineering and Architecture, Izmir Katip, Celebi University, Cigli, 35620-Izmir, Turkey, [2]Organic Semiconductor Centre, EaStCHEM School of Chemistry, University of St Andrews, St Andrews, UK, KY16 9ST, [3]Organic Semiconductor Centre, SUPA School of Physics and Astronomy, University of St Andrews, St Andrews KY16 9SS, UK, [4]Instituto de Ciencia Molecular (ICMol), Universidad de Valencia, C/Catedrático J. Beltrán 2, 46980 Paterna (Valencia), Spain and [5]School of Chemistry, University of Leeds, Woodhouse Lane, Leeds, UK

Email:
Daniel Tordera[*] - daniel.tordera@uv.es; Eli Zysman-Colman[*] - eli.zysman-colman@st-andrews.ac.uk

* Corresponding author

Keywords:
electroluminescence; light-emitting electrochemical cells; multiresonance; purely organic emitters; thermally activated delayed fluorescence

Beilstein J. Org. Chem. **2022,** *18,* 1311–1321.
https://doi.org/10.3762/bjoc.18.136

Received: 24 June 2022
Accepted: 08 September 2022
Published: 22 September 2022

This article is part of the thematic issue "Organic TADF materials design".

Associate Editor: P. J. Skabara

Abstract

We designed and synthesized two new ionic thermally activated delayed fluorescent (TADF) emitters that are charged analogues of a known multiresonant TADF (MR-TADF) compound, **DiKTa**. The emission of the charged derivatives is red-shifted compared to the parent compound. For instance, **DiKTa-OBuIm** emits in the green (λ_{PL} = 499 nm, 1 wt % in mCP) while **DiKTa-DPA-OBuIm** emits in the red (λ_{PL} = 577 nm, 1 wt % in mCP). In 1 wt % mCP films, both emitters showed good photoluminescence quantum yields of 71% and 61%, and delayed lifetimes of 316.6 µs and 241.7 µs, respectively, for **DiKTa-OBuIm** and **DiKTa-DPA-OBuIm**, leading to reverse intersystem crossing rates of 2.85×10^3 s^{-1} and 3.04×10^3 s^{-1}. Light-emitting electrochemical cells were prepared using both **DiKTa-OBuIm** and **DiKTa-DPA-OBuIm** as active emitters showing green (λ_{max} = 534 nm) and red (λ_{max} = 656 nm) emission, respectively.

Introduction

Light-emitting electrochemical cells (LEECs) are thin film light-emitting devices typically consisting of an emissive layer containing ionic species that facilitate charge transport and an emissive semiconductor material. The emissive layer is sandwiched between two air-stable electrodes [1]. Upon application of an external bias the ions in the active layer migrate to the corresponding electrodes, resulting in the formation of electrical double layers (EDLs) at the interface of the electrodes. The EDLs facilitate charge injection into the emissive layer regardless of the energy levels of the electroactive species and work function of the electrodes. Injection of electrons and holes creates oxidized and reduced species near the anode and cathode, respectively. These oxidized and reduced species are stabilized by the ions to form a p-i-n junction in the bulk of the emissive layer and emission takes place within the intrinsic region [2-6].

Two families of widely investigated emitters for LEECs are ionic transition metal complexes (iTMCs) [7-10] and conjugated polymers (CPs) [4]. From the early use of ruthenium(II) complexes, a significant amount of research has focussed on developing high-performance iTMC-based LEECs [11,12], with iridium(III) complexes typically showing the greatest potential. A detracting feature of many iTMC LEECs is the use of scarce noble metal complexes. Despite the enormous number of low molecular weight organic emitters designed for use in organic light-emitting diodes (OLEDs), relatively little attention has been devoted to the design of ionic small molecule (SM) [13] organic emitters for LEECs. The majority of the reported SM emitters for LEECs are fluorescent in nature and so the internal quantum efficiency (IQE) of the device is limited to 25% [13]. Thermally activated delayed fluorescent (TADF) emitters are one class of purely organic materials that can harvest triplet excitons in electroluminescent (EL) devices through a triplet to singlet reverse intersystem crossing (RISC) upconversion process [14]. Indeed, OLEDs using TADF emitters can achieve up to 100% IQE, comparable to devices using phosphorescent emitters [15].

Purely organic TADF emitters have not been widely investigated for use in LEECs. We reported the first organic TADF LEEC, **I** (Figure 1a, original compound **2** in [16]), in 2015 by adapting the structure of the known TADF emitter 2CzPN with imidazolium groups [16,17] (Figure 1a). The LEEC devices showed a maximum external quantum efficiency (EQE_{max}) of 0.39%, a maximum brightness (B_{max}) of 13 cd m^{-2}, and a peak electroluminescence (λ_{EL}) at 538 nm. The device performance suffered when the emissive layer was doped with an ionic liquid (EQE_{max} = 0.12%, B_{max} = 10 cd m^{-2}), which was incorporated to increase charge mobility within the emissive layer. We later showed that this emitter could act as host material in combination with a cyanine dye emitter [18]. The EQE_{max} for this host–guest device was higher than for the non-doped device, at 2.0% demonstrated 100% exciton utilization efficiency in the device and efficient energy transfer from the host to the guest cyanine emitter. Deep blue emission in LEECs is challenging. We also reported a blue-emitting LEEC employing a cationic sulfone-based donor–acceptor TADF emitter, **imCzDPS** (λ_{PL} = 440 nm, Φ_{PL} = 44%, neat film) [19]. The EL of the LEEC was red-shifted at λ_{EL} of 470 nm compared to the PL. Following these initial reports Edman and co-workers demonstrated how neutral TADF small molecules [20], polymers [21], and dendrimers [22] could be employed in LEECs where the emissive layer also contained an inorganic salt and a conducting polymer. Recently, a step-change in device performance were achieved by He et al. who employed a cationic TADF compound that possesses low-lying through-space and through-bond charge transfer excited states [23]. The LEEC showed a green EL with a peak brightness of 572 cd m^{-2} and an EQE_{max} of 6.8% at 4.0 V. The half-life of their device reached 218 h at a brightness of 162 cd m^{-2}. Recently, Su et al. reported two ionic TADF emitters incorporating a pyridinium moiety, **Pym-CZ** and **Pym-tBuCZ** as the acceptor and carbazole or *tert*-butylcarbazole as donor groups [24]. **Pym-CZ** showed red emission in dichloromethane (λ_{PL} = 691 nm, Φ_{PL} = 43%) and in the neat film (λ_{PL} = 583 nm, Φ_{PL} = 15%). The emission is further red-shifted and attenuated in **Pym-tBuCZ** in dichloromethane (λ_{PL} = 740 nm, Φ_{PL} = 8%) and in the neat film (λ_{PL} = 593 nm, Φ_{PL} = 6%). The LEECs with **Pym-CZ** (λ_{EL} = 599 nm, B_{max} = 8.69 cd m^{-2}, EQE_{max} = 0.91%) and **Pym-tBuCZ** (λ_{EL} = 618 nm, B_{max} = 1.96 cd m^{-2}, EQE_{max} = 0.05%) are the first examples of orange-red devices employing purely organic intrinsically ionic TADF emitters. Though these reports hint at the potential of TADF emitters in LEECs, the emission in these devices is typically broad, reflective of the charge transfer (CT) character of the emission, and so colour purity suffers.

Narrowband emission has, however, been demonstrated in multiresonant TADF (MR-TADF) materials. MR-TADF compounds, first introduced by Hatakeyama and co-workers, are typically p- and n-doped nanographenes [25,26]. OLEDs using MR-TADF emitters can simultaneously achieve narrowband emission and very high EQE_{max}. Inspired by our recent work on neutral MR-TADF emitters for OLEDs [27,28], we designed two charged analogues of **DiKTa** [29] (Figure 1b), to make them amenable for use as emitters in LEECs, **DiKTa-OBuIm** and **DiKTa-DPA-OBuIm** (Figure 1c). In 1 wt % doped mCP films, **DiKTa-OBuIm** emits in the green region (λ_{PL} = 499 nm, Φ_{PL} = 71%, 1 wt % in mCP) and **DiKTa-DPA-OBuIm** is a red emitter (λ_{PL} = 577 nm, Φ_{PL} = 61%, 1 wt % in mCP). The pres-

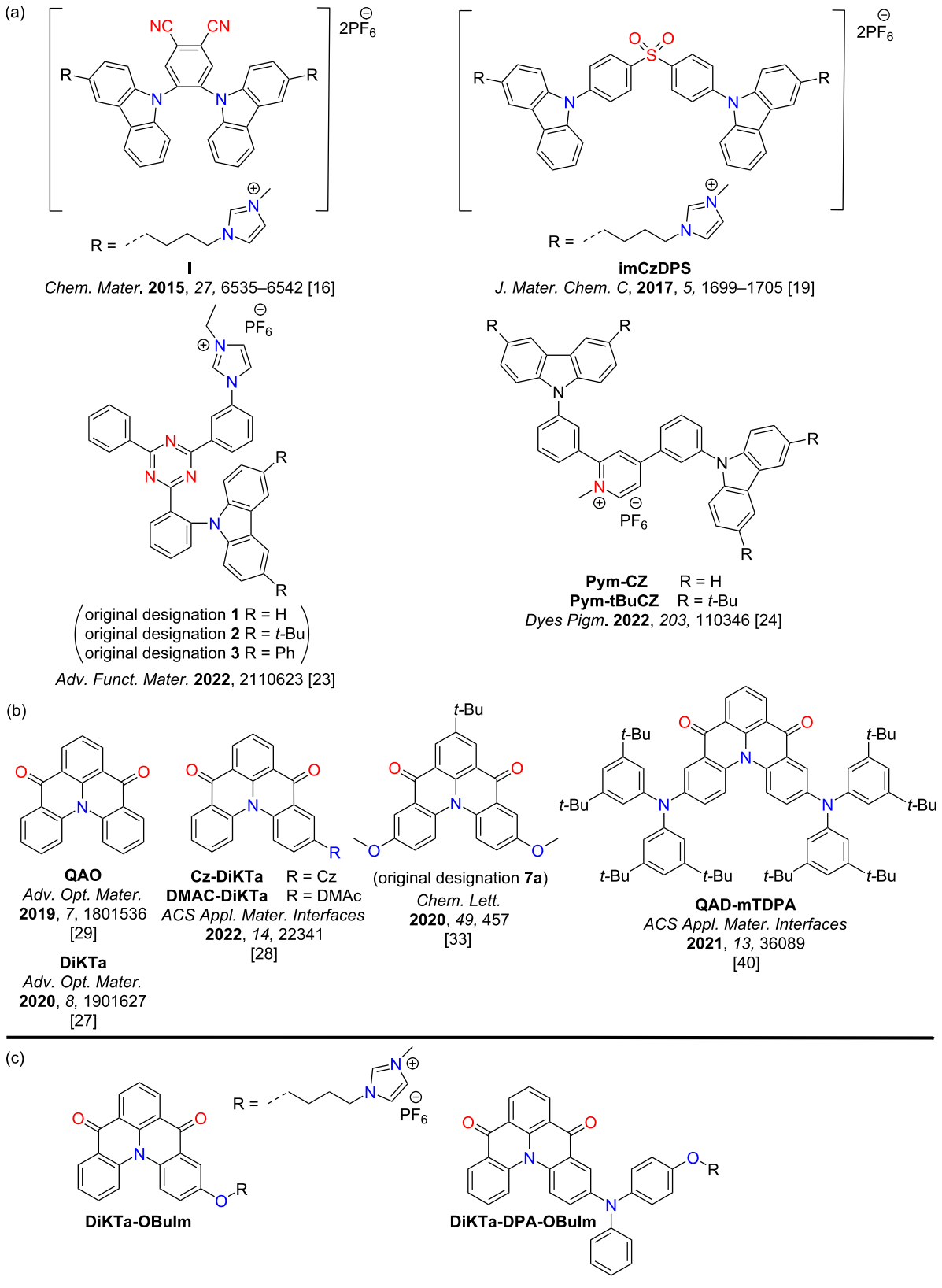

Figure 1: Chemical structures of (a) reported ionic TADF emitters for LEECs, (b) the MR-TADF emitter **DiKTa** and selected derivatives, and (c) the ionic emitters in this work.

ence of the DPA group in **DiKTa-DPA-OBuIm** transforms this compound from one that is MR-TADF to one that is better described as a donor–acceptor TADF, which is reflected in the red-shifted and broadened emission [28].

Results and Discussion

DiKTa-OBuIm was obtained in three steps (Scheme 1) in 23% overall yield. First, hydrolysis of **1**, in situ conversion to the acyl chloride and subsequent Lewis acid-promoted Friedel–Crafts acylation reaction produced compound **2** (Scheme 1), where the $AlCl_3$ was also responsible for the demethylation. Compound **2** was then subjected to monoalkylation with 1,4-dibromobutane in moderate yield, followed by a second alkylation step with 1-methylimidazole in very good yield. **DiKTa-OBuIm** was isolated as its hexafluorophosphate salt following anion metathesis with NH_4PF_6. **DiKTa-DPA-OBuIm** was obtained also in three steps at 35% overall yield from compound **4** using a similar synthetic strategy, which itself was synthesized from **Br-DiKTa** [28] following a Buchwald–Hartwig coupling. Details of the synthesis are found in Supporting Information File 1. The identity and purity of the molecules were verified using a combination of ^1H and

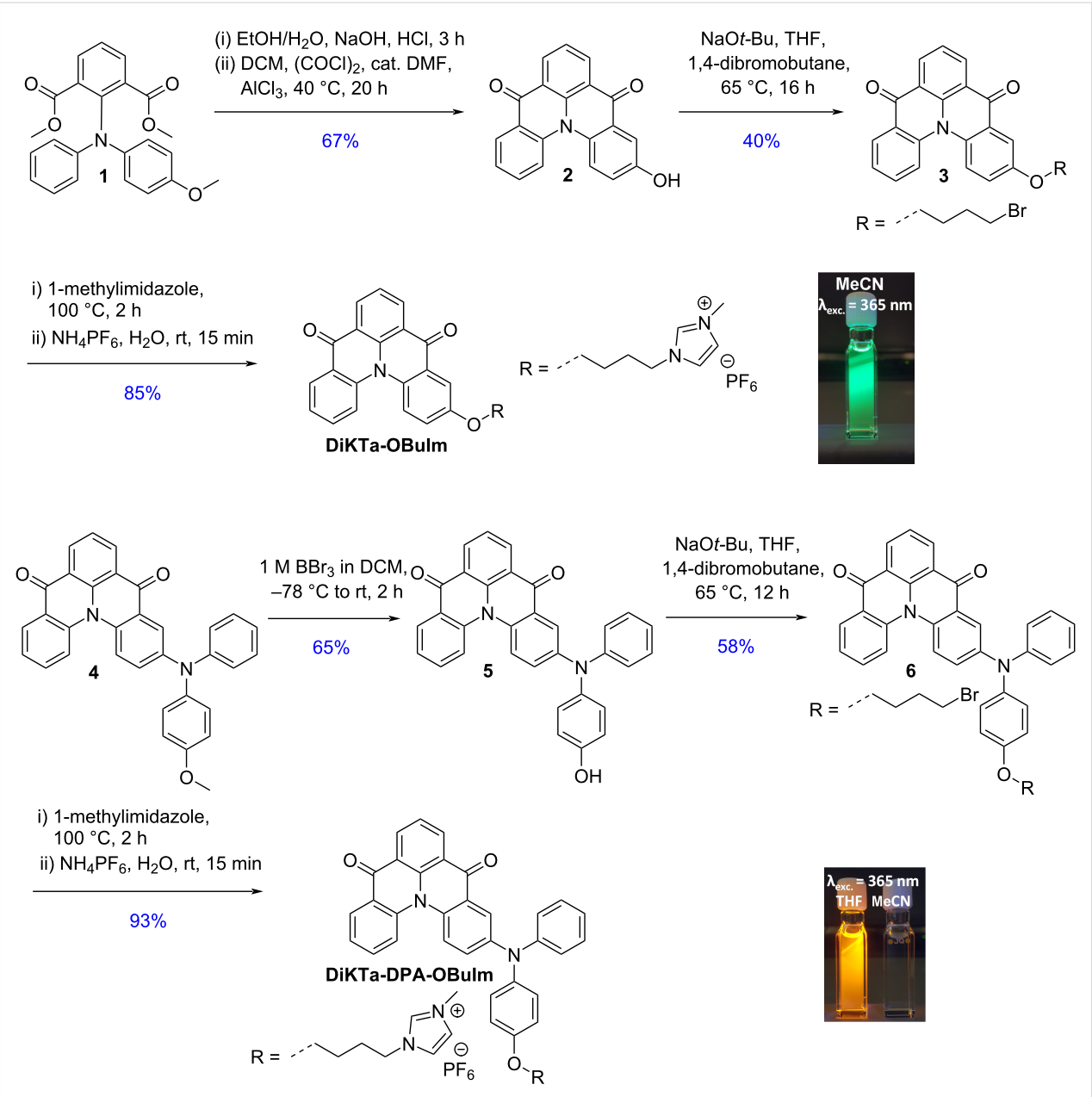

Scheme 1: Synthesis of **DiKTa-OBuIm** and **DiKTa-DPA-OBuIm**.

^{13}C NMR spectroscopy, high resolution mass spectrometry (HRMS) (Figures **S1–S24** in Supporting Information File 1), and melting point analysis.

We modelled the electron density distribution in **DiKTa-OBuIm** and **DiKTa-DPA-OBuIm** using density functional theory (DFT) calculations in the ground state, at the PBE0/6-31G(d,p) level of theory in the gas phase (Figure 2a). The calculations were based on model systems, **DiKTa-OMe** and **DiKTa-DPA-OMe**, respectively, wherein we replaced the imidazolium side chain of **DiKTa-OBuIm** and **DiKTa-DPA-OBuIm**, respectively, with a methyl group [30]. Compared to **DiKTa** (HOMO = −6.20 eV, LUMO = −2.23 eV, ΔE_g = 3.97 eV), both emitters possess a smaller HOMO–LUMO gap. The HOMO is more strongly affected by the incorporation of donor units [28]. For instance, in the case of **Cz-DiKTa** and **DMAC-DiKTa** the HOMO is destabilized by 0.47 eV and 0.94 eV, respectively, compared to **DiKTa** [28]. The lowest unoccupied molecular orbital (LUMO) for both compounds is localized on the **DiKTa** core (Figure S25 in Supporting Information File 1). This orbital is only slightly stabilized in **DiKTa-DPA-OMe** due to the presence of the more strongly electron-donating DPA group. The highest occupied molecular orbital (HOMO) in **DiKTa-OMe** is also localized on the **DiKTa** core and the electron density distribution of this molecule is reminiscent of that of a MR-TADF compound and is nearly identical to that of the parent emitter, **DiKTa** [27] (Figure S25 in Supporting Information File 1). There is a very large change in both the electron density distribution and the HOMO energy between the two emitters. For **DiKTa-DPA-OMe**, the HOMO is mainly localized on the DPA unit but with some delocalization onto the **DiKTa** core, resulting in a destabilization of this orbital from −5.91 eV in **DiKTa-OMe** to −5.19 eV in **DiKTa-DPA-OMe**. The HOMO–LUMO gap, ΔE_g, thus decreases to 3.08 eV compared to that of **DiKTa-OMe** (3.74 eV). The excited states were modelled using spin-component scaling second-order approximate coupled-cluster (SCS-CC2) in tandem with the cc-pVDZ basis set (Table S1 in Supporting Information File 1). Figure 2b shows the difference density plots for singlet (S) and triplet (T) excited states for **DiKTa-OMe** and **DiKTa-DPA-OMe**. Compared to **DiKTa** (S_1 = 3.45 eV, T_1 = 3.18 eV, f = 0.20, ΔE_{ST} = 0.27 eV) [28], the lowest-lying singlet (S_1) and triplet (T_1) states are stabilized in the case of **DiKTa-OMe**, while the singlet–triplet energy gap, ΔE_{ST}, remained the same at 0.27 eV. The nature of S_1 and T_1 resemble to those of its parent **DiKTa** and so this compound is

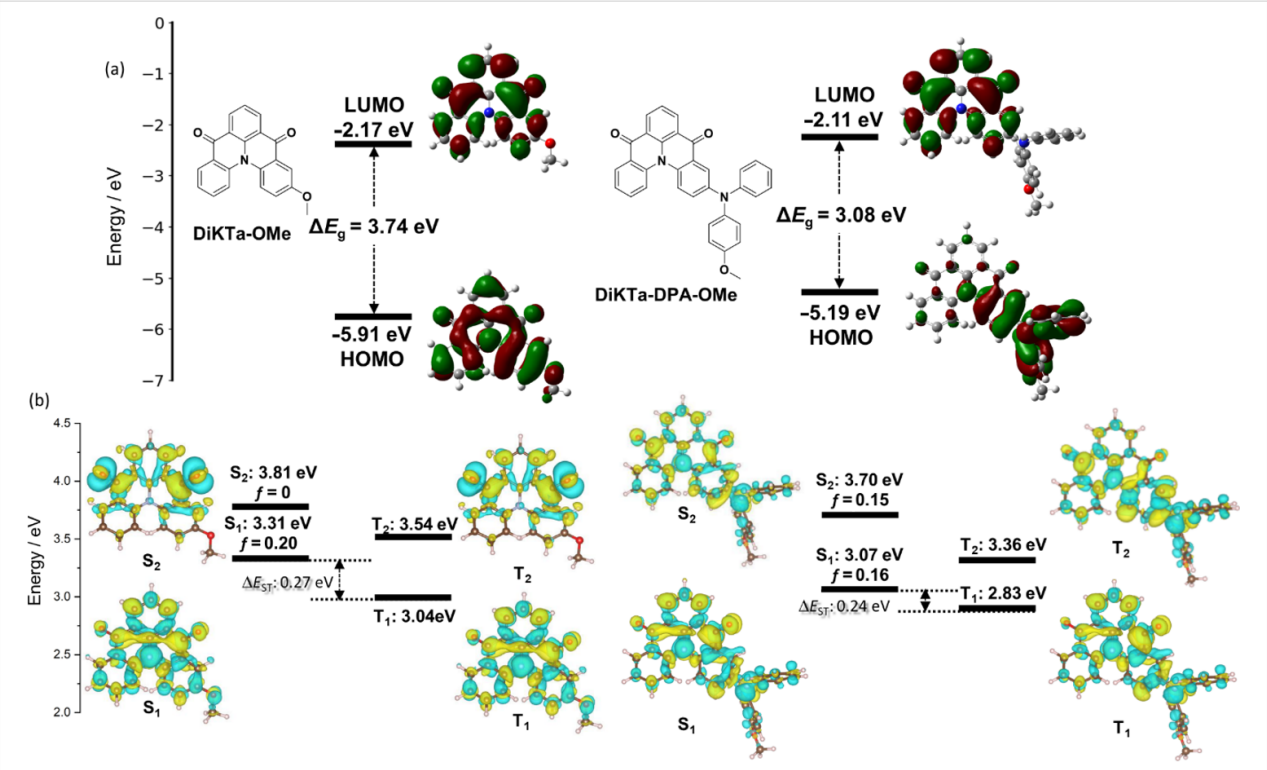

Figure 2: (a) HOMO and LUMO electron density distribution and orbital energies of **DiKTa-OMe** and **DiKTa-DPA-OMe** calculated at the PBE0/6-31G(d,p) level of theory in the gas phase, isovalue = 0.02; (b) difference density plots and energies for the two lowest-lying singlet and triplet excited states for **DiKTa-OMe** and **DiKTa-DPA-OMe** calculated at SCS-CC2/cc-pVDZ in the gas phase (isovalue = 0.001). The blue color represents an area of decreased electron density, and yellow represents an increased electron density between the ground and excited states; *f* denotes the oscillator strength for the transition to the excited singlet state.

likely to behave as a MR-TADF emitter. The nature of the S_2 state is n–π* in **DiKTa-OMe**. The excited state picture of **DiKTa-DPA-OMe** is different to that of other reported D–A-type systems containing **DiKTa** as the acceptor [28]. Long range charge transfer is not apparent here and instead the coupled cluster calculations predict a compound that is MR-TADF but where the electron density distribution is delocalized over the entire molecule. Compared to **DiKTa-OMe**, both S_1 and T_1 of **DiKTa-DPA-OMe** are stabilized to 3.07 eV and 2.83 eV, respectively. The ΔE_{ST} decreases to 0.24 eV and there is no intermediate triplet state. The trend of stabilized S_1 and T_1 states when a donor group decorates the **DiKTa** core (S_1 = 3.45 eV, T_1 = 3.18 eV) has been previously observed in reported emitters such as **Cz-DiKTa** (S_1 = 3.35 eV, T_1 = 3.09 eV) and **DMAC-DiKTa** (S_1 = 3.43 eV, T_1 = 3.17 eV) [28]. We also calculated the charge transfer character of each excited state, focussing on the distance of charge transfer (D_{CT}). When considering the S_1 excited state, there is an increase in CT character moving from **DiKTa**, **DiKTa-OMe**, and **DiKTa-DPA-OMe** (D_{CT} = 1.45 Å, 1.81 Å, and 3.34 Å, respectively) reflected in the increased donor strength.

The electrochemical properties of **DiKTa-OBuIm** and **DiKTa-DPA-OBuIm** were investigated by cyclic voltammetry (CV) and differential pulse voltammetry (DPV) in acetonitrile with 0.1 M tetra-*n*-butylammonium hexafluorophosphate as the supporting electrolyte (Figure 3a and Table S2 in Supporting Information File 1). The oxidation and reduction of both emitters showed good reversibility, which is beneficial for better performance in LEEC devices [31]. The oxidation potentials, E_{ox}, determined from the peak value of the first DPV curve are 1.05 V and 0.44 V for **DiKTa-OBuIm** and **DiKTa-DPA-OBuIm**, respectively, which correspond to HOMO energy levels of −5.85 eV and −5.24 eV, respectively. The trend of a destabilized HOMO energy level from **DiKTa-OBuIm** to **DiKTa-DPA-OBuIm** is predicted by DFT calculations. **DiKTa** possesses an oxidation potential of 1.66 V and an associated HOMO energy level of −5.93 eV. The reduction potentials, E_{red}, are −1.67 V and −1.61 V, respectively, for **DiKTa-OBuIm** and **DiKTa-DPA-OBuIm**. The corresponding LUMO levels are −3.13 eV and −3.18 eV for **DiKTa-OBuIm** and **DiKTa-DPA-OBuIm**, respectively. The LUMO values of both emitters match that of **DiKTa** (−3.11 eV), which suggests that reduction occurs on the **DiKTa** core in both compounds, a contention corroborated by the DFT calculations. The electrochemical gap reduced from 2.72 V in **DiKTa-OBuIm** to 2.06 V in **DiKTa-DPA-OBuIm**, a trend that is in line with the DFT calculations.

Figure 3b shows the solution-state photophysical properties of **DiKTa-OBuIm** and **DiKTa-DPA-OBuIm** in acetonitrile and the data are compiled in Table 1. The lowest energy absorption band for **DiKTa-OBuIm** at 453 nm ($\varepsilon = 17 \times 10^3$ M^{-1} cm^{-1}) is red-shifted and slightly more intense than that of the parent **DiKTa** at 436 nm, ($\varepsilon = 14 \times 10^3$ M^{-1} cm^{-1}) [27] owing to the increased conjugation in **DiKTa-OBuIm**. For the emitter **7a** (Figure 1b) [33] reported by Yan et al. the red-shift of the lowest energy absorption band was more pronounced than that in **DiKTa-OBuIm**. This band is assigned to a short-range charge transfer transition (SRCT) that is a hallmark characteristic in MR-TADF compounds [28]. The Stokes shift is 54 nm (2361 cm^{-1}) for **DiKTa-OBuIm**. The lowest energy absorption band in **DiKTa-DPA-OBuIm** is red-shifted and less intense ($\varepsilon = 6 \times 10^3$ M^{-1} cm^{-1}) compared to **DiKTa-OBuIm**, in line

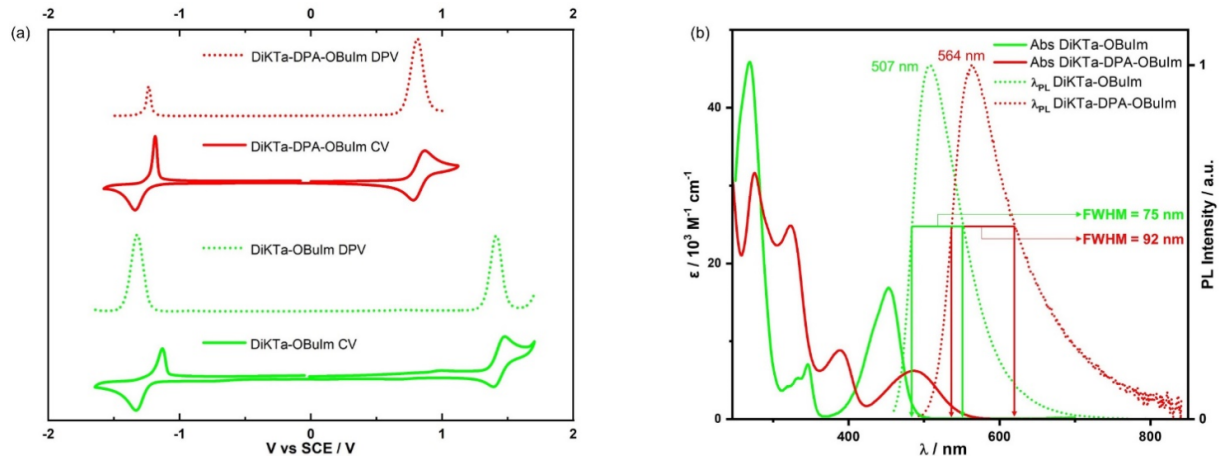

Figure 3: (a) Cyclic and differential pulse voltammograms measured in degassed MeCN with 0.1 M [*n*-Bu_4N]PF_6 as the supporting electrolyte and Fc^+/Fc as the internal reference (0.38 V vs SCE) [32]. Scan rate = 100 mV s^{-1}; (b) solution-state photophysical measurements: absorption and steady-state emission spectra at 300 K measured in MeCN. λ_{exc} = 453 nm for **DiKTa-OBuIm** and λ_{exc} = 488 nm for **DiKTa-DPA-OBuIm**.

Table 1: Photophysical properties of **DiKTa-OBuIm** and **DiKTa-DPA-OBuIm**.

Compound	Medium	λ_{Abs}[a] [nm]	λ_{PL}[b] [nm]	FWHM[c] [nm]	E_{S1}[d] [eV]	E_{T1}[d] [eV]	ΔE_{ST}[e] [eV]
DiKTa-OBuIm	sol.[f]	453 (17)	507	75	2.66	2.41	0.25
	film[g]	–	500	66	2.65	2.45	0.20
DiKTa-DPA-OBuIm	sol.[f]	488 (6)	563	92	–	–	–
	film[g]	–	578	95	2.40	2.21	0.19
	Φ_{PL}[h] [%]	τ_p[i] [ns]	τ_d[i] [µs]	k_{ISC}[j] [s^{-1}] ($\times 10^7$)	k_{RISC}[j] [s^{-1}] ($\times 10^3$)	k_{s_r}[j] [s^{-1}] ($\times 10^7$)	k_{s_nr}[j] [s^{-1}] ($\times 10^7$)
DiKTa-OBuIm	48[a]	14.3[a]	–	–	–	–	–
	71 (57)[b]	8.7[b]	316.6[b]	3.59 ± 1.3	2.85 ± 1.1	6.60	2.69
DiKTa-DPA-OBuIm	11[a]	12.7[a]	–	–	–	–	–
	61 (53)[b]	14.1[b]	241.7[b]	2.21 ± 1.2	3.04 ± 1.7	3.78	2.38

[a]Lowest energy absorbance band, absorptivity (ε) in parentheses (/ × 10^3 M^{-1} s^{-1}). [b]Steady-state emission maximum at 300 K; λ_{exc} = 340 nm. [c]Full width at half maximum of the emission peak. [d]S_1 and T_1 energies were obtained from the onsets of the respective prompt fluorescence (delay: 1 ns; gate time: 100 ns) and phosphorescence spectra (delay: 1 ms; gate time: 9 ms) at 77 K; λ_{exc} = 343 nm. [e]$\Delta E_{ST} = E(S_1) - E(T_1)$. [f]In MeCN solutions ($10^{-6}$ M). [g]Measured in spin-coated thin films consisting of 1.0 wt % emitter in mCP; λ_{exc} = 340 nm. [h]Φ_{PL} in solutions were measured by the relative method using quinine sulfate as a standard (Φ_r = 54.6% in 1 N H_2SO_4) [38], while absolute Φ_{PL} of thin films were measured using an integrating sphere; λ_{exc} = 340 nm under nitrogen and the values in parentheses are in the presence of O_2. [i]Prompt and delayed lifetimes in solutions and thin films obtained by TCSPC and MCS, λ_{exc} = 379 nm. [j]Intersystem and reverse intersystem crossing rates were calculated using the steady-state approximation method as described in literature [39].

with its decreased oscillator strength (vide supra). According to the calculations (vide supra), the S_1 excited state is also SRCT, but with larger long-range charge transfer (LRCT) content. Owing to the relative flexibility around the DPA donor unit, the Stokes shift is larger at 75 nm (2761 cm^{-1}). **DiKTa-OBuIm** and **DiKTa-DPA-OBuIm** exhibited broad green (λ_{PL} = 507 nm, FWHM = 75 nm) and red (λ_{PL} = 563 nm, FWHM = 92 nm) emissions in MeCN, respectively, which is larger than **DiKTa** (46 nm in MeCN) [27] in line with the greater LRCT character for these emitters; this observation has been noted for other donor decorated MR-TADF emitters [34-36]. The photoluminescence quantum yield, Φ_{PL}, in MeCN for **DiKTa-OBuIm** is 48% which decreases in air to 34%. The emission is much weaker in **DiKTa-DPA-OBuIm**, reflecting both the smaller oscillator strength of the transition to S_1 and the greater non-radiative decay due to the energy gap law (Φ_{PL} = 11% and 7% under vacuum and in air, respectively) in MeCN [37]. The S_1 and T_1 levels were measured from the onsets of fluorescence (2.66 eV) and phosphorescence spectra (2.41 eV) in 2-MeTHF glass at 77 K (Figure S26, Supporting Information File 1). **DiKTa-OBuIm** possesses a ΔE_{ST} of 0.25 eV. Unfortunately, **DiKTa-DPA-OBuIm** was insoluble in 2-MeTHF and so the measurement could not be made. No delayed component was observed in MeCN solution under vacuum for either of the compounds (Figure S27 in Supporting Information File 1).

The thin film PL behavior of both emitters was then assessed in 1 wt % doped film in 1,3-di-9-carbazolylbenzene (mCP) (Figure 4). At this doping concentration, the photophysical

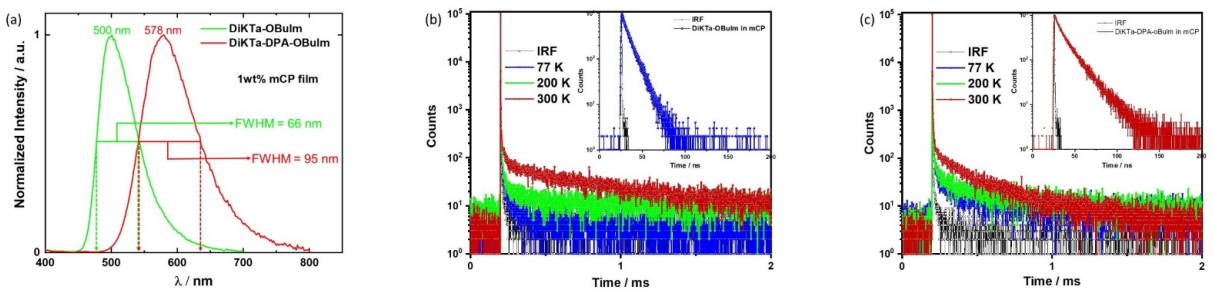

Figure 4: (a) Steady-state emission spectra of **DiKTa-OBuIm** and **DiKTa-DPA-OBuIm** in 1 wt % doped mCP films, $\lambda_{exc.}$ = 340 nm; (b) temperature-dependent time resolved PL decays of **DiKTa-OBuIm** in 1 wt % doped mCP films. Inset: prompt PL decay of **DiKTa-OBuIm;** (c) temperature-dependent time resolved PL decays of **DiKTa-DPA-OBuIm** in 1 wt % doped mCP films. Inset: prompt PL decay of **DiKTa-DPA-OBuIm**, $\lambda_{exc.}$ = 379 nm.

properties should reflect monomolecular entities. Emission was observed at 500 nm (FWHM = 66 nm) and 578 nm (FWHM = 95 nm) for **DiKTa-OBuIm** and **DiKTa-DPA-OBuIm**, respectively. The emission spectrum of **DiKTa-OBuIm** is slightly blue-shifted and narrower than that in MeCN, which is expected due to the higher polarity of the solvent than mCP. Surprisingly, for **DiKTa-DPA-OBuIm** the emission is red-shifted by 14 nm, and with negligible change in the FWHM. This suggests that the conformation of the emitter in the solid state is slightly more conjugated than that in solution or that there are specific host–guest interactions with the DPA unit that perturbs the energy of the excited state. The emission is broader than that of a structurally similar emitter, **QAD-mTDPA**, a derivative of **DiKTa** containing two DPA substituents, reported by Zhang et al. [40] The structure of **QAD-mTDPA** (λ_{PL} = 587 nm, FWHM = 62 nm, Φ_{PL} = 97%, ΔE_{ST} = 0.33 eV, τ_D = 269 μs, 1.5 wt % CBP) is shown in Figure 1b. Both emitters showed red-shifted and broadened emission compared to that of **DiKTa** (λ_{PL} = 466 nm, FWHM = 40 nm, Φ_{PL} = 70%, ΔE_{ST} = 0.20 eV, τ_D = 168 μs, 2 wt % mCP) in the same host [28]. Both emitters exhibited high Φ_{PL} values in the mCP film at 71% and 61% under nitrogen, and these reduced to 57% and 53% in air for **DiKTa-OBuIm** and **DiKTa-DPA-OBuIm**, respectively. As neat thin films, the emission for both compounds are red-shifted and significantly quenched (Figure S28 in Supporting Information File 1); indeed, the Φ_{PL} for the neat film of **DiKTa-OBuIm** is only 9% while we could not ascertain a reliable value for **DiKTa-DPA-OBuIm**. Severe aggregation-caused quenching of the emission in the neat film was also observed for **DiKTa** (Φ_{PL} = 11%, under N_2) [27]. The S_1 and T_1 levels were measured from the onsets of fluorescence and phosphorescence spectra in the 1 wt % doped mCP film at 77 K (Figure S29 in Supporting Information File 1). The corresponding ΔE_{ST} values are 0.20 eV and 0.19 eV, respectively, for **DiKTa-OBuIm** and **DiKTa-DPA-OBuIm**, which are nearly same to that reported for **DiKTa** (ΔE_{ST} = 0.20 eV) [28]. Experimental ΔE_{ST} values are smaller than those computationally predicted (0.27 eV and 0.24 eV, respectively for **DiKTa-OBuIm** and **DiKTa-DPA-OBuIm**). However, the trend of decreasing ΔE_{ST} is in line to the findings from DFT. The temperature dependent time-resolved PL decays in the 1 wt % doped mCP films are presented in Figure 4b and c. Both emitters show prompt and delayed emission components with an enhancement of the delayed emission with increasing temperature, a feature of TADF. Unlike the delayed emission lifetime of **DiKTa** (15 μs in 3.5 wt % mCP, 23 μs in PhMe) [27], and its derivatives such as **Cz-DiKTa** (τ_D = 196 μs, 2 wt % mCP), **DMAC-DiKTa** (τ_D = 6.6 μs, 2 wt % mCP), and **QAD-mTDPA** (τ_D = 168 μs, in 2 wt % mCP) in Figure 1b [28,40], the delayed lifetimes from **DiKTa-OBuIm** and **DiKTa-DPA-OBuIm** are long at 317 μs and 242 μs, respectively. RISC rate constants, k_{RISC}, were calculated for both emitters, which are 2.85×10^3 s^{-1} and 3.04×10^3 s^{-1}, respectively for **DiKTa-OBuIm** and **DiKTa-DPA-OBuIm**, compared to that of **DiKTa** (4.6×10^4 s^{-1}) in toluene [27,39].

Light-emitting electrochemical cells

LEECs were fabricated using **DiKTa-OBuIm** and **DiKTa-DPA-OBuIm** as emitters. The device stack was the following: ITO/PEDOT:PSS/emitter/Al (where ITO is indium tin oxide; PEDOT:PSS is poly(3,4-ethylenedioxythiophene):poly(styrenesulfonate)). The PEDOT:PSS and the emitter layers were prepared from solution and the device was finished with an evaporated Al top contact. Details of the LEEC fabrication can be found in the General Methods section of Supporting Information File 1. Driven by their promising Φ_{PL} LEEC devices using **DiKTa-OBuIm** and **DiKTa-DPA-OBuIm** as 1 wt % doped films in mCP as the emitter layer were prepared. The devices showed no turn-on, both in lifetime measurements and in current density and luminance versus voltage sweeps (*JVL*) up to 8 V. Most likely the low content of ionic species in the neutral matrix hindered the required ionic transport for LEEC operation. To solve this, we fabricated devices adding an ionic liquid (lithium hexafluorophosphate ($LiPF_6$) or 1-butyl-3-methylimidazolium hexafluorophosphate ($BMIM:PF_6$) in a 4 to 1 molar ratio) and, in some cases, an electrolyte matrix (PEO (polyethylene oxide)), to improve the ionic mobility on the active film [5,41]. However, despite these efforts, still no emission was observed when the devices were biased. Next, neat films of **DiKTa-OBuIm** and **DiKTa-DPA-OBuIm** were directly used as active layers. Non-doped small molecule films have shown recently promising results in LEEC devices [42]. As both emitters are ionic, in principle there is no need to incorporate additional mobile ions. A host–guest approach, using 1 wt % of **DiKTa-DPA-OBuIm** in **DiKTa-OBuIm** was also used, the latter acting as a host matrix for the former. The electroluminescence (EL) of the three device stacks is shown in Figure 5a. Similar to the PL, the EL spectra are broad and unstructured. The EL of **DiKTa-OBuIm** and **DiKTa-DPA-OBuIm** occurs at λ_{EL} of 534 and 656 nm, respectively. Both neat-film EL spectra are red-shifted from the solution state and the 1 wt % in mCP film PL spectra. The origin of this red shift could be ascribed to the presence of emissive aggregates in the emissive layer [19]. Interestingly, in the host–guest system the energy transfer is not complete and both molecules are responsible for the electroluminescence, with a λ_{EL} at 586 nm, between the emission of the neat films. *JVL* characterization (from −2 to 8 V) was carried out on the three stacks (Figure 5b–d). As it can be seen, the current density reaches high values, and the injection is primarily dominated by ohmic behavior. The device with **DiKTa-DPA-OBuIm** shows a steeper injection reaching values of

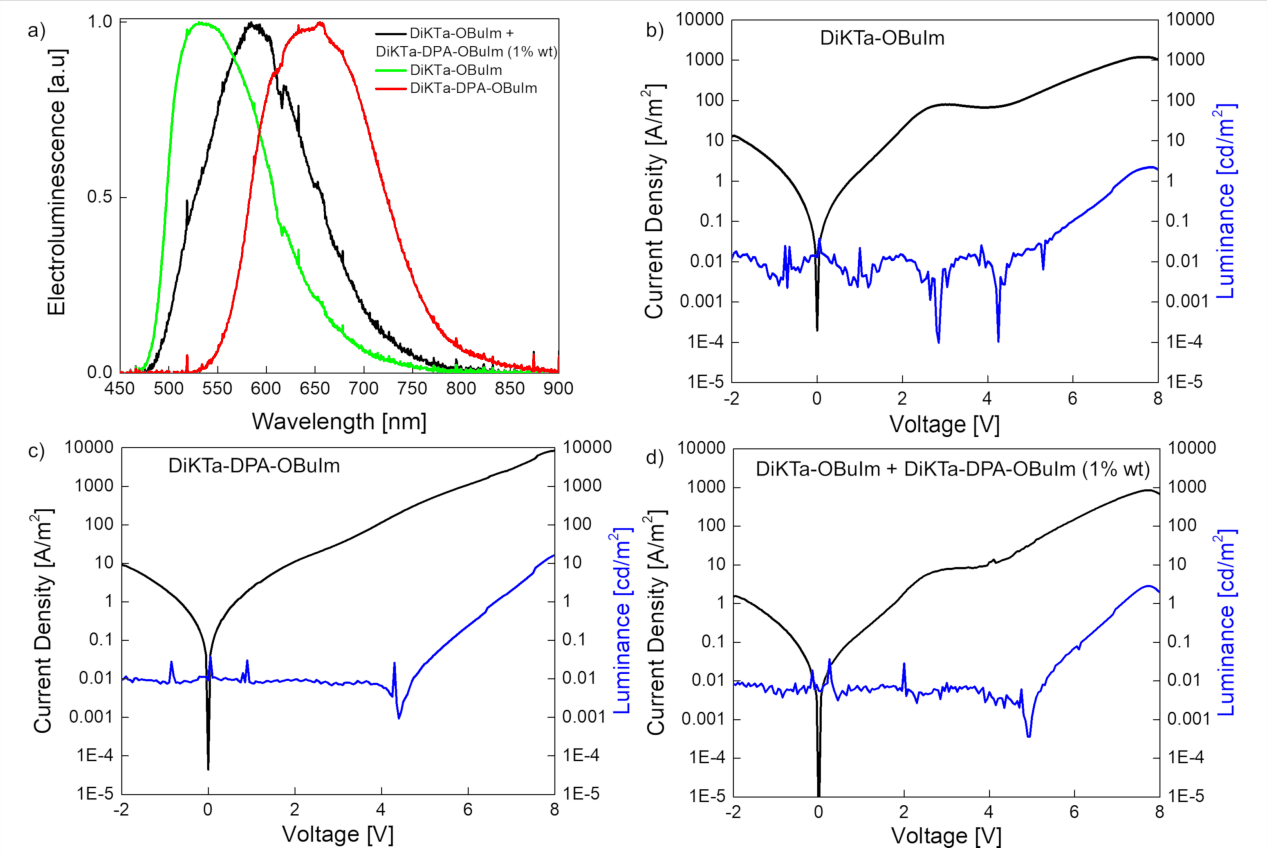

Figure 5: (a) Electroluminescence spectra of **DiKTa-OBuIm** (green curve), **DiKTa-DPA-OBuIm** (red curve) and 1% of **DiKTa-DPA-OBuIm** in **DiKTa-OBuIm** (black curve). Current (black) and luminance (blue) versus voltage (*JVL*) sweep (from −2 to 8 V) of (b) **DiKTa-OBuIm**, (c) **DiKTa-DPA-OBuIm**, and (d) 1% of **DiKTa-DPA-OBuIm** in **DiKTa-OBuIm**.

10,000 A m^{-2} at 8 V when compared with the device with **DiKTa-OBuIm**, which shows a current density of 1000 A m^{-2} at the same voltage value. The current density in the device with the host–guest system is dominated by the presence of **DiKTa-OBuIm**. Light emission is detected at around ≈5 V, with values of 15 cd m^{-2} for the device with **DiKTa-DPA-OBuIm** and around 2 cd m^{-2} for the devices with **DiKTa-OBuIm** and the host–guest system, each at 8 V. From the EL spectra it is possible to estimate the external quantum efficiency (EQE) values; however, they are also highly affected by the luminance levels, giving as a result very low efficiencies (<0.01%).

Conclusions

Two new ionic TADF emitters were designed and synthesized for LEECs application using a known MR-TADF emitter **DiKTa**. Our MR-TADF green emitter, **DiKTa-OBuIm** exhibited efficient green luminescence and TADF in 1 wt % mCP film (λ_{PL} = 499 nm, FWHM = 66 nm, Φ_{PL} = 71%, τ_d = 317 µs, k_{RISC} = 2.85 × 10^3 s^{-1}). This emitter represents a rare example of an ionic MR-TADF emitter for LEEC applications. The red emitter, **DiKTa-DPA-OBuIm**, was obtained by coupling a methoxy-modified diphenylamine unit onto the **DiKTa** fragment. Addition of a donor unit red-shifted the emission to red region with TADF (λ_{PL} = 577 nm, FWHM = 95 nm, Φ_{PL} = 61%, τ_d = 242 µs, k_{RISC} = 3.04 × 10^3 s^{-1}, 1 wt % in mCP). Different strategies were explored to prepare LEECs based on **DiKTa-OBuIm** and **DiKTa-DPA-OBuIm** as emitters. The devices showed green and red emission, respectively.

Supporting Information

The research data supporting this publication can be accessed at https://doi.org/10.17630/6ef45b8f-579d-4075-891e-595516c56e47.

Supporting Information File 1

^{1}H NMR and ^{13}C NMR spectra, GC–MS, and HRMS; supplementary computational data and coordinates; additional photophysical.
[https://www.beilstein-journals.org/bjoc/content/supplementary/1860-5397-18-136-S1.pdf]

Acknowledgements

We thank Dr. David Hall for providing help with the calculations and initial samples of some of the intermediates.

Funding

M. K. would like to thank 2214-A International Research Fellowship Programme for Ph.D. students (1059B141900585). This project has received funding from the European Union's Horizon 2020 research and innovation programme under the Marie Skłodowska Curie grant agreement No 838885 (NarrowbandSSL). S.M.S. acknowledges support from the Marie Skłodowska-Curie Individual Fellowship (grant agreement No 838885 NarrowbandSSL). A. K. G. is grateful to the Royal Society for Newton International Fellowship NF171163. L.M acknowledges that the project who gave rise to these results received support from the European Research Council (ERC) under the European Union's Horizon 2020 research and innovation programme Grant agreement No. 834431, the Spanish Ministry of Science, Innovation and Universities (MICIU, RTI2018-095362-A-I00, and EQC2018-004888-P) and the Comunitat Valenciana (IDIFEDER/2020/063 and PROMETEU/2020/077). D.T. acknowledges support from the Comunitat Valenciana (CIGE/2021/0).

ORCID® iDs

Merve Karaman - https://orcid.org/0000-0003-2803-7414
Abhishek Kumar Gupta - https://orcid.org/0000-0002-0203-6256
Tomas Matulaitis - https://orcid.org/0000-0003-0470-7356
Lorenzo Mardegan - https://orcid.org/0000-0002-9262-8094
Daniel Tordera - https://orcid.org/0000-0001-9283-8801
Henk J. Bolink - https://orcid.org/0000-0001-9784-6253
Ifor D. Samuel - https://orcid.org/0000-0001-7821-7208
Eli Zysman-Colman - https://orcid.org/0000-0001-7183-6022

Preprint

A non-peer-reviewed version of this article has been previously published as a preprint: doi:10.26434/chemrxiv-2022-n35w9-v3

References

1. Pei, Q.; Costa, R. D. *Adv. Funct. Mater.* **2020,** *30,* 2002879. doi:10.1002/adfm.202002879
2. van Reenen, S.; Matyba, P.; Dzwilewski, A.; Janssen, R. A. J.; Edman, L.; Kemerink, M. *J. Am. Chem. Soc.* **2010,** *132,* 13776–13781. doi:10.1021/ja1045555
3. Lindh, E. M.; Lundberg, P.; Lanz, T.; Edman, L. *Sci. Rep.* **2019,** *9,* 10433. doi:10.1038/s41598-019-46860-y
4. Youssef, K.; Li, Y.; O'Keeffe, S.; Li, L.; Pei, Q. *Adv. Funct. Mater.* **2020,** *30,* 1909102. doi:10.1002/adfm.201909102
5. Mindemark, J.; Edman, L. *J. Mater. Chem. C* **2016,** *4,* 420–432. doi:10.1039/c5tc03429a
6. Ràfols-Ribé, J.; Zhang, X.; Larsen, C.; Lundberg, P.; Lindh, E. M.; Mai, C. T.; Mindemark, J.; Gracia-Espino, E.; Edman, L. *Adv. Mater. (Weinheim, Ger.)* **2022,** *34,* 2107849. doi:10.1002/adma.202107849
7. Bai, R.; Meng, X.; Wang, X.; He, L. *Adv. Funct. Mater.* **2020,** *30,* 1907169. doi:10.1002/adfm.201907169
8. Zhang, C.; Liu, R.; Zhang, D.; Duan, L. *Adv. Funct. Mater.* **2020,** *30,* 1907156. doi:10.1002/adfm.201907156
9. Hu, T.; He, L.; Duan, L.; Qiu, Y. *J. Mater. Chem.* **2012,** *22,* 4206–4215. doi:10.1039/c2jm16185k
10. Housecroft, C. E.; Constable, E. C. *J. Mater. Chem. C* **2022,** *10,* 4456–4482. doi:10.1039/d1tc04028f
11. Costa, R. D.; Ortí, E.; Bolink, H. J.; Monti, F.; Accorsi, G.; Armaroli, N. *Angew. Chem., Int. Ed.* **2012,** *51,* 8178–8211. doi:10.1002/anie.201201471
12. Henwood, A. F.; Zysman-Colman, E. *Top. Curr. Chem.* **2016,** *374,* 36. doi:10.1007/s41061-016-0036-0
13. Kanagaraj, S.; Puthanveedu, A.; Choe, Y. *Adv. Funct. Mater.* **2020,** *30,* 1907126. doi:10.1002/adfm.201907126
14. Wong, M. Y.; Zysman-Colman, E. *Adv. Mater. (Weinheim, Ger.)* **2017,** *29,* 1605444. doi:10.1002/adma.201605444
15. Nakanotani, H.; Tsuchiya, Y.; Adachi, C. *Chem. Lett.* **2021,** *50,* 938–948. doi:10.1246/cl.200915
16. Wong, M. Y.; Hedley, G. J.; Xie, G.; Kölln, L. S.; Samuel, I. D. W.; Pertegás, A.; Bolink, H. J.; Zysman-Colman, E. *Chem. Mater.* **2015,** *27,* 6535–6542. doi:10.1021/acs.chemmater.5b03245
17. Uoyama, H.; Goushi, K.; Shizu, K.; Nomura, H.; Adachi, C. *Nature* **2012,** *492,* 234–238. doi:10.1038/nature11687
18. Pertegás, A.; Wong, M. Y.; Sessolo, M.; Zysman-Colman, E.; Bolink, H. J. *ECS J. Solid State Sci. Technol.* **2016,** *5,* R3160–R3163. doi:10.1149/2.0201601jss
19. Wong, M. Y.; La-Placa, M.-G.; Pertegas, A.; Bolink, H. J.; Zysman-Colman, E. *J. Mater. Chem. C* **2017,** *5,* 1699–1705. doi:10.1039/c6tc04821h
20. Lundberg, P.; Tsuchiya, Y.; Lindh, E. M.; Tang, S.; Adachi, C.; Edman, L. *Nat. Commun.* **2019,** *10,* 5307. doi:10.1038/s41467-019-13289-w
21. Lundberg, P.; Wei, Q.; Ge, Z.; Voit, B.; Reineke, S.; Edman, L. *J. Phys. Chem. Lett.* **2020,** *11,* 6227–6234. doi:10.1021/acs.jpclett.0c01506
22. Matsuki, K.; Pu, J.; Takenobu, T. *Adv. Funct. Mater.* **2020,** *30,* 1908641. doi:10.1002/adfm.201908641
23. Yu, R.; Song, Y.; Zhang, K.; Pang, X.; Tian, M.; He, L. *Adv. Funct. Mater.* **2022,** *32,* 2110623. doi:10.1002/adfm.202110623
24. Shen, H.-L.; Hsiao, P.-W.; Yi, R.-H.; Su, Y.-H.; Chen, Y.; Lu, C.-W.; Su, H.-C. *Dyes Pigm.* **2022,** *203,* 110346. doi:10.1016/j.dyepig.2022.110346
25. Hirai, H.; Nakajima, K.; Nakatsuka, S.; Shiren, K.; Ni, J.; Nomura, S.; Ikuta, T.; Hatakeyama, T. *Angew. Chem., Int. Ed.* **2015,** *54,* 13581–13585. doi:10.1002/anie.201506335
26. Madayanad Suresh, S.; Hall, D.; Beljonne, D.; Olivier, Y.; Zysman-Colman, E. *Adv. Funct. Mater.* **2020,** *30,* 1908677. doi:10.1002/adfm.201908677
27. Hall, D.; Suresh, S. M.; dos Santos, P. L.; Duda, E.; Bagnich, S.; Pershin, A.; Rajamalli, P.; Cordes, D. B.; Slawin, A. M. Z.; Beljonne, D.; Köhler, A.; Samuel, I. D. W.; Olivier, Y.; Zysman-Colman, E. *Adv. Opt. Mater.* **2020,** *8,* 1901627. doi:10.1002/adom.201901627
28. Wu, S.; Li, W.; Yoshida, K.; Hall, D.; Madayanad Suresh, S.; Sayner, T.; Gong, J.; Beljonne, D.; Olivier, Y.; Samuel, I. D. W.; Zysman-Colman, E. *ACS Appl. Mater. Interfaces* **2022,** *14,* 22341–22352. doi:10.1021/acsami.2c02756
29. Yuan, Y.; Tang, X.; Du, X.-Y.; Hu, Y.; Yu, Y.-J.; Jiang, Z.-Q.; Liao, L.-S.; Lee, S.-T. *Adv. Opt. Mater.* **2019,** *7,* 1801536. doi:10.1002/adom.201801536

30. Subeesh, M. S.; Shanmugasundaram, K.; Sunesh, C. D.; Chitumalla, R. K.; Jang, J.; Choe, Y. *J. Phys. Chem. C* **2016,** *120,* 12207–12217. doi:10.1021/acs.jpcc.6b03710
31. Tang, S.; Sandström, A.; Lundberg, P.; Lanz, T.; Larsen, C.; van Reenen, S.; Kemerink, M.; Edman, L. *Nat. Commun.* **2017,** *8,* 1190. doi:10.1038/s41467-017-01339-0
32. Connelly, N. G.; Geiger, W. E. *Chem. Rev.* **1996,** *96,* 877–910. doi:10.1021/cr940053x
33. Yan, C.; Shang, R.; Nakamoto, M.; Yamamoto, Y.; Adachi, Y. *Chem. Lett.* **2020,** *49,* 457–460. doi:10.1246/cl.200089
34. Yang, M.; Park, I. S.; Yasuda, T. *J. Am. Chem. Soc.* **2020,** *142,* 19468–19472. doi:10.1021/jacs.0c10081
35. Qi, Y.; Ning, W.; Zou, Y.; Cao, X.; Gong, S.; Yang, C. *Adv. Funct. Mater.* **2021,** *31,* 2102017. doi:10.1002/adfm.202102017
36. Xu, Y.; Li, C.; Li, Z.; Wang, Q.; Cai, X.; Wei, J.; Wang, Y. *Angew. Chem., Int. Ed.* **2020,** *59,* 17442–17446. doi:10.1002/anie.202007210
37. Serevičius, T.; Skaisgiris, R.; Dodonova, J.; Fiodorova, I.; Genevičius, K.; Tumkevičius, S.; Kazlauskas, K.; Juršėnas, S. *J. Phys. Chem. Lett.* **2022,** *13,* 1839–1844. doi:10.1021/acs.jpclett.1c03810
38. Melhuish, W. H. *J. Phys. Chem.* **1961,** *65,* 229–235. doi:10.1021/j100820a009
39. Tsuchiya, Y.; Diesing, S.; Bencheikh, F.; Wada, Y.; dos Santos, P. L.; Kaji, H.; Zysman-Colman, E.; Samuel, I. D. W.; Adachi, C. *J. Phys. Chem. A* **2021,** *125,* 8074–8089. doi:10.1021/acs.jpca.1c04056
40. Huang, F.; Wang, K.; Shi, Y.-Z.; Fan, X.-C.; Zhang, X.; Yu, J.; Lee, C.-S.; Zhang, X.-H. *ACS Appl. Mater. Interfaces* **2021,** *13,* 36089–36097. doi:10.1021/acsami.1c09743
41. Alahbakhshi, M.; Mishra, A.; Haroldson, R.; Ishteev, A.; Moon, J.; Gu, Q.; Slinker, J. D.; Zakhidov, A. A. *ACS Energy Lett.* **2019,** *4,* 2922–2928. doi:10.1021/acsenergylett.9b01925
42. John, J. C.; Shanmugasundaram, K.; Gopakumar, G.; Choe, Y. *ACS Photonics* **2022,** *9,* 203–210. doi:10.1021/acsphotonics.1c01397

License and Terms

BEILSTEIN JOURNAL OF ORGANIC CHEMISTRY

Naphthalimide-phenothiazine dyads: effect of conformational flexibility and matching of the energy of the charge-transfer state and the localized triplet excited state on the thermally activated delayed fluorescence

Kaiyue Ye[‡1], Liyuan Cao[‡1], Davita M. E. van Raamsdonk[‡2], Zhijia Wang[1], Jianzhang Zhao[*1,3], Daniel Escudero[*2] and Denis Jacquemin[*4]

Full Research Paper

Open Access

Address:
[1]State Key Laboratory of Fine Chemicals, Frontiers Science Center for Smart Materials, School of Chemical Engineering, Dalian University of Technology, Dalian 116024, P. R. China, [2]Department of Chemistry, KU Leuven, B-3001 Leuven, Belgium, [3]State Key Laboratory of Chemistry and Utilization of Carbon Based Energy Resources, College of Chemistry, Xinjiang University, Urumqi 830017, P. R. China and [4]Nantes Université, CNRS, CEISAM UMR-6230, Nantes F-44000, France

Email:
Jianzhang Zhao[*] - zhaojzh@dlut.edu.cn; Daniel Escudero[*] - daniel.escudero@kuleuven.be; Denis Jacquemin[*] - Denis.Jacquemin@univ-nantes.fr

* Corresponding author ‡ Equal contributors

Keywords:
charge-transfer; electron donor; intersystem crossing; TADF; triplet state

Beilstein J. Org. Chem. **2022,** *18,* 1435–1453.
https://doi.org/10.3762/bjoc.18.149

Received: 14 April 2022
Accepted: 26 September 2022
Published: 11 October 2022

This article is part of the thematic issue "Organic TADF materials design".

Guest Editor: E. Zysman-Colman

Abstract

In order to investigate the joint influence of the conformation flexibility and the matching of the energies of the charge-transfer (CT) and the localized triplet excited (^{3}LE) states on the thermally activated delayed fluorescence (TADF) in electron donor–acceptor molecules, a series of compact electron donor–acceptor dyads and a triad were prepared, with naphthalimide (NI) as electron acceptor and phenothiazine (PTZ) as electron donor. The NI and PTZ moieties are either directly connected at the 3-position of NI and the *N*-position of the PTZ moiety via a C–N single bond, or they are linked through a phenyl group. The tuning of the energy order of the CT and LE states is achieved by oxidation of the PTZ unit into the corresponding sulfoxide, whereas conformation restriction is imposed by introducing *ortho*-methyl substituents on the phenyl linker, so that the coupling magnitude between the CT and the ^{3}LE states can be controlled. The singlet oxygen quantum yield (Φ_Δ) of **NI-PTZ** is moderate in *n*-hexane (HEX, Φ_Δ = 19%). TADF was observed for the dyads, the biexponential luminescence lifetime are 16.0 ns (99.9%)/14.4 µs (0.1%) for the dyad and 7.2 ns (99.6%)/2.0 µs (0.4%) for the triad. Triplet state was observed in the nanosecond transient absorption spectra with lifetimes in the 4–48 µs range. Computational investigations show that the orthogonal electron donor–acceptor molecular structure is beneficial for TADF. These calculations indicate small energetic difference between the ^{3}LE and ^{3}CT states, which are

helpful for interpreting the ns-TA spectra and the origins of TADF in **NI-PTZ**, which is ultimately due to the small energetic difference between the ^{3}LE and ^{3}CT states. Conversely, **NI-PTZ-O**, which has a higher CT state and bears a much more stabilized ^{3}LE state, does not show TADF.

Introduction

Thermally activated delayed fluorescence (TADF) has attracted much attention in recent years, not only for its application in organic light emitting diodes (OLED) [1-3] but also as a mean for studying of charge-transfer (CT) and intersystem-crossing (ISC) phenomena [4,5]. Compounds showing TADF are usually presenting an orthogonal electron donor–acceptor molecular structure, i.e., the π-planes of the electron donor and acceptor adopt an orthogonal geometry [6,7]. Such an architecture is beneficial to spatially split HOMO and LUMO orbitals, thus reducing the electron-exchange integral (J) for the two electrons in the frontier molecular orbitals which reduced the energy gap ($2J$) between these two states. lt is widely considered that this small energy gap (a few dozens of meV) is beneficial for both ISC and the reverse ISC (rISC) in TADF [1-3,8-13].

However, it is noted that in some electron donor–acceptor dyads, TADF is not observed even when the CT state is accessible [14,15]. This is typically because the direct ISC between ^{1}CT and ^{3}CT is forbidden and non-efficient, and this hyperfine interaction-driven ISC is slow. Recently, it was proposed that an intermediate localized triplet state (^{3}LE) is essential to enhance the ISC and rISC, through the so-called spin-vibronic coupling effect [8,16-19]. However, the effect of the molecular geometry on the ISC and rlSC is complicated, and additional investigations are required to verify the above postulate and to unravel the TADF mechanism.

Recently, we and others found that the orthogonal donor–acceptor dyad derived from 1,8-naphthalimide (NI) and phenothiazine (PTZ) shows TADF in the red spectral range [20-22]. Our purpose of designing that dyad was to study the spin–orbit charge-transfer ISC (SOCT-ISC), i.e., to determine, if the ISC is enhanced by the charge recombination (CR) in the orthogonal dyad. Indeed, CR is accompanied by orbital angular momentum change, which off-sets the electron spin angular momentum change, allowing the angular momentum to be conserved and, consequently, ISC to be enhanced [23-31]. We underline that the orthogonal geometry of this dyad reduces the ^{1}CT/^{3}CT states energy gap while simultaneously enhancing the ISC for the ^{1}CT→^{3}LE process. Therefore, we propose that the TADF is actually a special case of SOCT-ISC, when the three ^{1}CT/^{3}CT/^{3}LE states have similar energies. Nevertheless, in most orthogonal dyads showing SOCT-ISC, the ^{3}LE state has a much lower energy than the CT states, especially in triplet photosensitizers, for which a final ^{3}LE state is desired [32,33]. As explained above, an orthogonal geometry is beneficial to achieve SOCT-ISC. However, for TADF, it was proposed that the rotational freedom is beneficial for the rISC, and that too rigid molecular structures may favor phosphorescence and therefore limit rISC and TADF [34,35]. Studies with time-resolved electron paramagnetic resonance (TREPR) spectra and theoretical methods also support that conformation fluctuations are beneficial to TADF [16]. This is in stark contrast with the SOCT-ISC mechanism.

To further explore these contradictory requirements for SOCT-ISC and TADF, we designed herein a series of **NI-PTZ** dyads, and the synthesis route is mentioned in the following section of molecular design and structural confirmation. These dyads are different from the previously reported dyads by the substitution position, and the number of PTZ moieties attached on the NI unit, as well as the redox potential of the PTZ moiety. **NI-PTZ** has a linkage at the 3-position of the NI moiety, for the recently reported analogous dyad, however, the substitution is at the 4-position [20]. For the current **NI-PTZ** dyad, the torsion between the NI and PTZ has a larger freedom, due to the reduced steric hindrance originating from the *peri*-H atoms on the two chromophores. We also tuned the redox potentials by oxidation of the electron donor PTZ (**NI-PTZ-O**). Thus, the energy of CT states and the matching with their ^{3}LE counterpart can be altered. We underline that the approach of oxidation of the PTZ unit, which has minimal impacts on the geometry and the ^{3}LE state energy in the dyad, was rarely explored [8]. We also modified the energy of the CT states by increasing the distance between the electron donor and acceptor by using an intervening phenyl linker between the NI and the PTZ moieties (**NI-Ph-PTZ** and **NI-PhMe$_2$-PTZ**) [36]. The electronic coupling between the NI and PTZ units differ these two dyads. Finally, in **NI-PhMe$_2$-PTZ** with methyl substituents, the phenyl linker adopts an orthogonal geometry with respect to the NI moiety, inducing a weaker coupling than that in **NI-Ph-PTZ**. The photophysical properties of the dyads were studied with steady-state and time-resolved spectroscopic methods, as well as theoretical calculations.

Results and Discussion

Molecular design and structure confirmation

In order to study the effect of conformational flexibility on TADF, **NI-PTZ** was designed (Scheme 1). As dicussed above,

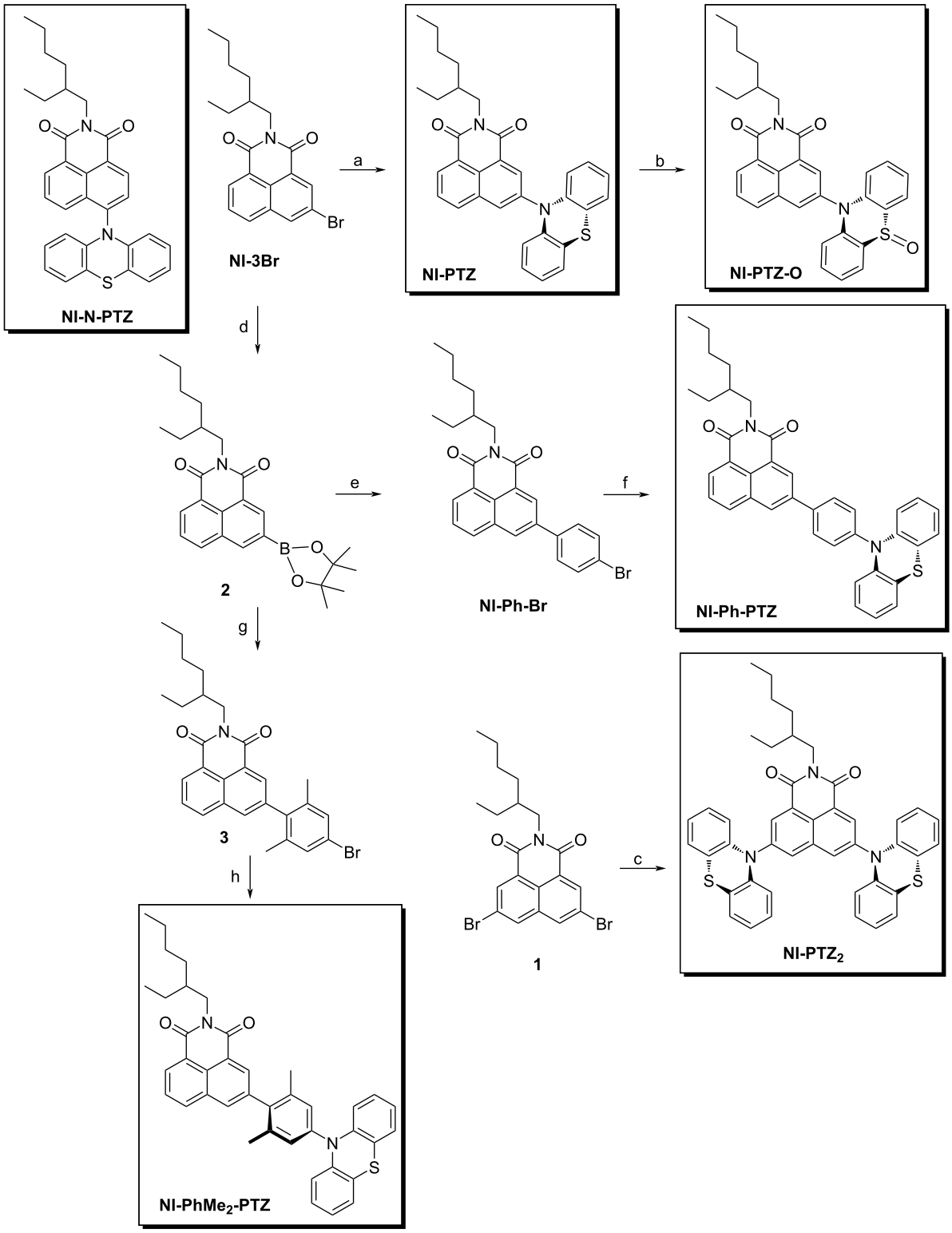

Scheme 1: Synthesis of the compounds[a]. [a]Key: (a) phenothiazine, sodium *tert*-butoxide, dried toluene (TOL), tri-*tert*-butylphosphine tetrafluoroborate, $Pd(OAc)_2$, 120 °C, 8 h, 93.1%; (b) H_2O_2 (30%), CH_3COOH, 40 °C, 1 h, yield: 87.2%; (c) similar to step (a), yield: 80.0%; (d) bis(pinacolato)diboron, KOAc, $Pd(dppf)Cl_2$, toluene, N_2, 110 °C, 16 h, yield: 11.9%.; (e) 1-bromo-4-iodobenzene, $Pd(PPh_3)_4$, K_2CO_3, TOL, EtOH, H_2O, N_2, reflux, 8 h, yield: 92.9%; (f) similar to step (a), yield: 62.4%; (g) 5-bromo-2-iodo-1,3-dimethylbenzene, $Pd(PPh_3)_4$, K_2CO_3, TOL, EtOH, H_2O, N_2, 110 °C, 9 h, yield: 60.6%; (h) similar to step (a), yield: 28.3%.

various approaches (different connection, linkers, oxidation of the PTZ, and addition of methyl groups) have been used to tune the relative energies of the key states and the geometry. Scheme 1 summarizes the synthetic routes used to obtain the various compounds and shows the molecular structures. The synthesis of the dyads is based on the ordinary derivatization of the NI and PTZ chromophores [20]. The molecular structures were confirmed by ^{1}H NMR, ^{13}C NMR, and HRMS methods (Experimental section).

UV–vis absorption and fluorescence emission spectra

The UV–vis absorption spectra of the compounds were studied (Figure 1 and Figure S25 in Supporting Information File 1). **NI-PTZ** shows structured absorption bands in the 300–350 nm range, which are attributed to the NI moiety [20]. Moreover, there is a broad, structureless absorption band centered at 412 nm ($\varepsilon = 1.30 \times 10^3$ M^{-1} cm^{-1}), which is assigned to a CT absorption band, i.e., to the $S_0 \rightarrow {}^1$CT transition. This is an indication of the strong electronic coupling between the electron donor (PTZ) and acceptor (NI). Indeed, in the absence of such coupling, the $S_0 \rightarrow {}^1$CT transition would be forbidden, and no CT absorption band would be observed [14,37-41].

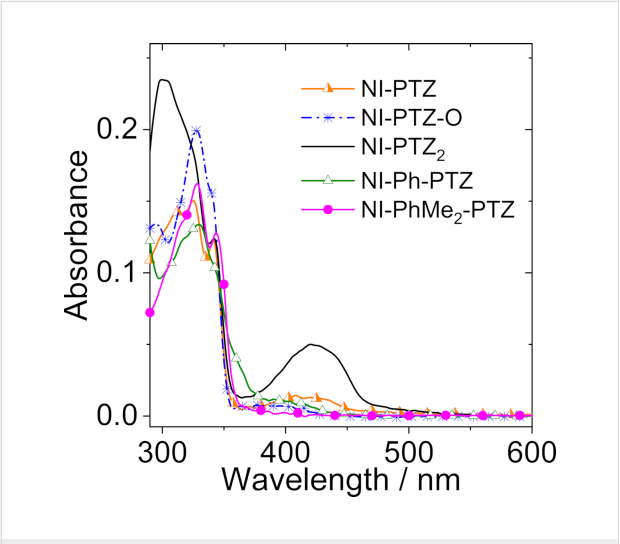

Figure 1: UV–vis absorption spectra of **NI-PTZ**, **NI-PTZ-O**, **NI-PTZ$_2$**, **NI-Ph-PTZ**, and **NI-PhMe$_2$-PTZ** in HEX. $c = 1.0 \times 10^{-5}$ M at 20 °C.

Interestingly, the CT absorption is similar to the previously reported **NI-N-PTZ** dyad with a linkage at the 4-position of the NI moiety [20], for which the CT absorption band is centered at 411 nm. Interesting in the **NI-PTZ$_2$** triad, the absorption band at 300–350 nm is different from that of **NI-PTZ**, and the CT absorption band centered at 423 nm is much more intense than that of **NI-PTZ**, indicating that the electronic effect of the substituents does not have a simple additive effect on the photophysical properties [42]. The CT absorption band of **NI-PTZ-O** is much weaker, confirming that the CT absorption band strongly depends on the electron-donating ability of the donor. In both **NI-Ph-PTZ** and **NI-PhMe$_2$-PTZ**, the CT band is negligible, due to the large separation between the NI and PTZ moieties. Note that in **NI-Ph-PTZ**, the electronic coupling between the NI and the phenyl linker is non-negligible, which results in a CT absorption in which the phenyl moiety acts as the donor. This analysis is supported by the UV–vis absorption spectrum of the 3-phenyl NI [43]. A careful examination of the UV–vis absorption spectra indicates that the PTZ moiety in **NI-Ph-PTZ** induces a slight redshift of the CT absorption band (centered at 405 nm) as compared to that of 3-phenyl NI [43].

These results show that our methods for tuning the electronic coupling between the donor and acceptor groups by alternation of the redox potentials of the donor (or acceptor), variation of the distance between the donor and acceptor, and conformational restriction, are all successful [44-46].

The fluorescence of the dyads was studied (Figure 2 and Figure S26 in Supporting Information File 1). As compared to that in cyclohexane (CHX) and HEX, the fluorescence of **NI-PTZ** is strongly quenched in TOL and solvents with higher polarity. This trend is similar to the one previously reported for the **NI-N-PTZ** analog [20]. We note that the CT emission band of **NI-PTZ** is slightly red-shifted as compared to that of the previously reported dyad. Upon oxidation of the PTZ moiety, i.e., for **NI-PTZ-O**, the fluorescence quenching in polar solvents is less significant than that of **NI-PTZ** (Figure 2b), and the CT emission band is blue-shifted as compared to that of **NI-N-PTZ** [20], a likely consequence of the reduced electron-donating ability of the PTZ moiety.

For **NI-PTZ$_2$**, a solvent polarity-dependent fluorescence band was observed (Figure 2c), which is similar to that of **NI-PTZ**. For **NI-Ph-PTZ**, a structured fluorescence band was observed in the 400–600 nm range (Figure 2d), which is assigned to LE emission. In toluene, however, a broad emission band centered at 624 nm was observed, which we attribute to the CT emission (with the phenyl moiety as donor group). The emission maximum (624 nm) is blue-shifted as compared to that of **NI-PTZ** (731 nm in toluene), indicating that the CT state energy of **NI-Ph-PTZ** is higher than that of **NI-PTZ** [47]. Similar results were observed for **NI-PhMe$_2$-PTZ** (Supporting Information File 1, Figure S26).

As a preliminary study to assess the existence of TADF for the dyads and the triad, the fluorescence spectra of the compounds in N_2-saturated and air-saturated solution were recorded (Figure 3 and Figure S27 in Supporting Information File 1). For

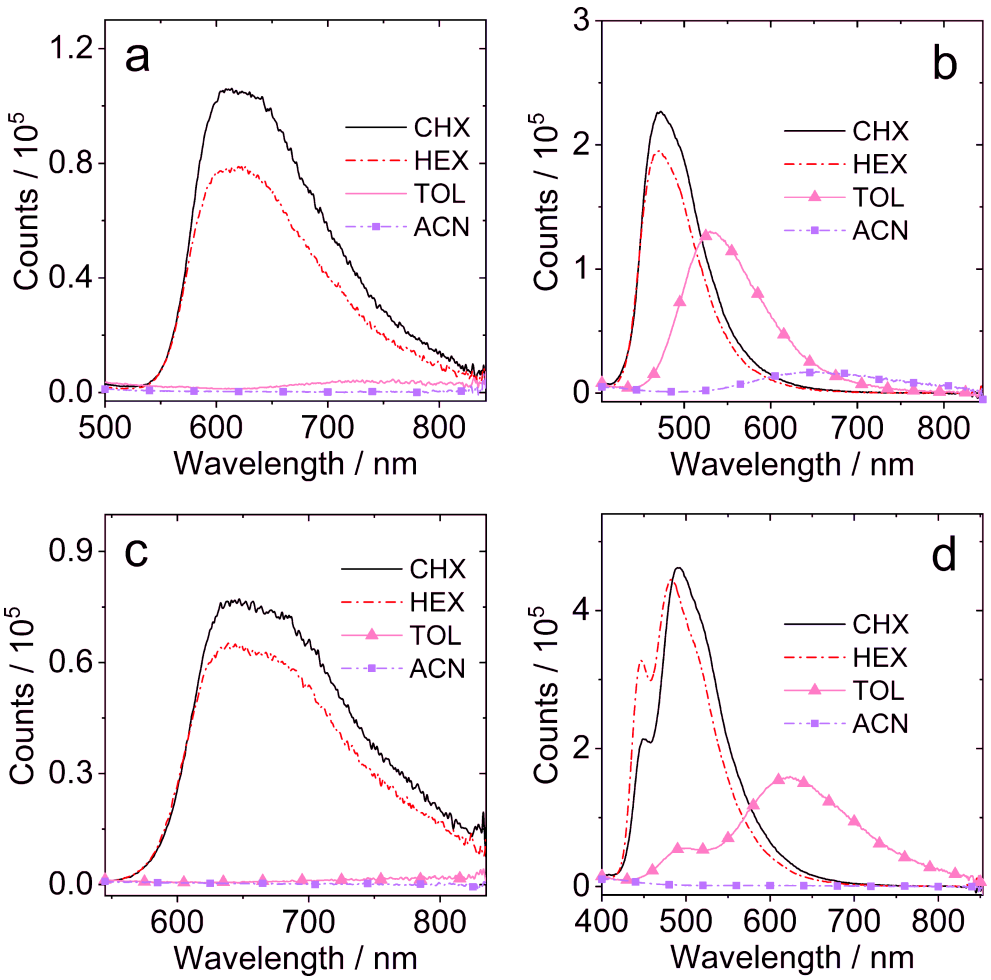

Figure 2: Fluorescence spectra of the compounds (a) **NI-PTZ**; (b) **NI-PTZ-O**; (c) **NI-PTZ$_2$**, and (d) **NI-Ph-PTZ** in different solvents. The solvents used are: CHX, HEX, TOL and acetonitrile (ACN). Optically matched solutions were used, A = 0.100, λ_{ex} = 330 nm, 20 °C.

both **NI-PTZ** and **NI-PTZ$_2$**, the fluorescence intensity was quenched significantly in aerated solution as compared to that in deaerated solution (Figure 3a and 3c and Figure S27a and S27c in Supporting Information File 1). For **NI-PTZ-O** and **NI-Ph-PTZ** (Figure 3b and 3d), however, the fluorescence intensity is less dependent on the atmosphere.

However, one should be careful with the interpretation of such data, as the quenching of the fluorescence in aerated solution does not necessarily imply TADF, since fluorescence species with long fluorescence lifetime can be also quenched by O_2 (a paramagnetic species). This is in particular relevant for the present compounds, since the fluorescence of **NI-PTZ** and **NI-PTZ$_2$** originate from CT states, whereas the emissions of **NI-PTZ-O** and **NI-Ph-PTZ** come from an emissive ^{1}LE state (due to the oxidation of the PTZ unit, or the phenyl linker, the CT state energy increases, and the ^{1}LE state becomes the lowest-lying state). Longer lifetimes are typically found for CT emission than LE emission, because of the forbidden feature of the ^{1}CT→S_0 transition.

Therefore, the fluorescence decay trace of the compounds was recorded (Figure 4). The fluorescence decay trace of **NI-PTZ** shows a distinct biexponential signature, the lifetime is 16.0 ns (99.9%)/14.4 µs (0.1%) in deaerated *n*-hexane (Figure 4a). In aerated solution, the luminescence lifetime is reduced to 7.6 ns (99.8%)/0.19 µs (0.2%) (Figure 4d). These are footprints for TADF. Similar features were reported for an analogous **NI-PTZ** dyad [20]. **NI-PTZ$_2$** displays similar characteristic TADF lifetimes (Figure 4b and 4e). Clearly, besides the conformational flexibility, other factors do play a role in the photophysical properties of the dyad, i.e., the magnitudes of CT/^{3}LE energy gap, and related spin–vibronic couplings. Increasing the CT state energy either through oxidation of the PTZ moiety (for **NI-PTZ-O**) or by using a longer linker (**NI-Ph-PTZ** and **NI-PhMe$_2$-PTZ**), leads to a normal fluorescence decay. Specif-

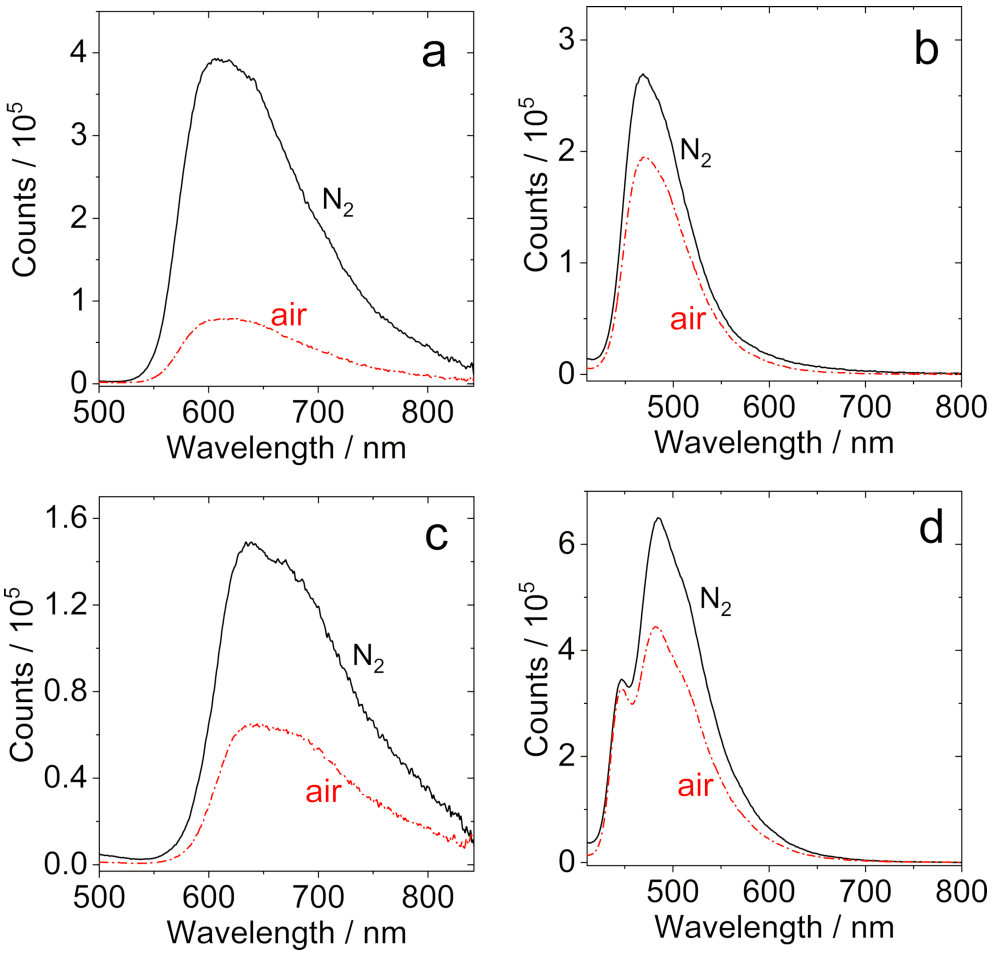

Figure 3: Fluorescence spectra of (a) **NI-PTZ**, (b) **NI-PTZ-O**, (c) **NI-PTZ$_2$**, and (d) **NI-Ph-PTZ** in HEX under different atmospheres (N_2, air). Optically matched solutions were used, A = 0.100, λ_{ex} = 330 nm, c = 1.0 × 10^{-5} M, 20 °C.

ically, the luminescence lifetimes of **NI-PTZ-O** and **NI-Ph-PTZ** are 3.1 ns (99%)/22.1 ns (1%) and 1.2 ns (77%)/4.5 ns (23%), respectively (Figure 4c and 4f). The fluorescence lifetimes of **NI-PhMe$_2$-PTZ** in CHX, HEX, and TOL were determined to be 1.6 ns (56%)/12.9 ns (44%), 1.2 ns (51%)/7.2 ns (49%), and 2.7 ns (22%)/18.7 ns (78%), respectively (Figure S28 in Supporting Information File 1).

In order to determine the ^{3}NI energy in the dyads and in the triad, the phosphorescence emission spectra of **NI-PTZ-O** in frozen solution at 77 K were recorded (Figure 5 and Figure S29 in Supporting Information File 1). No phosphorescence was detected for **NI-PTZ** nor **NI-PTZ$_2$**. For **NI-PTZ-O** (Figure 5a), a structured emission with significant vibrational progression was observed in the 520–650 nm range, which is attributed to the ^{3}LE state, as the emission band is similar to the one of 4-bromo NI [48]. Thus, the ^{3}NI state energy can be approximated to be 2.29 eV from the 0–0 band of the phosphorescence. The ^{3}NI energy of **NI-Ph-PTZ**, **NI-PhMe$_2$-PTZ**, and **NI-3Br** were determined to be 2.24 eV, 2.27 eV, and 2.27 eV, respectively (see Supporting Information File 1, Figure S29). For **NI-PTZ-O** (Figure 5b), the phosphorescence lifetime of the frozen solution attains 363 ms, which is similar to the phosphorescence lifetime of unsubstituted NI (ca. 410.3 ms) [48]. The phosphorescence lifetime of **NI-Ph-PTZ**, **NI-PhMe$_2$-PTZ**, and **NI-3Br** are 432 ms (Figure S30a, Supporting Information File 1), 376 ms (Figure S30b), and 4 ms (Figure S30c), respectively.

The photophysical properties of all compounds are compiled in Table 1. The fluorescence quantum yields of the dyads (1.0% to ≈4.5%) are generally much lower than those of the amino-NI derivatives (60% to ≈70%) [20]. In order to have a preliminary evaluation of the ISC of the compounds, the singlet oxygen quantum yields (Φ_Δ) were studied in several solvents (Table 1 and Table 2). For **NI-PTZ**, Φ_Δ is high in HEX (19%), which is similar to the value previously reported for the analogous dyad **NI-N-PTZ** (Φ_Δ = 16%) [20]. However, Φ_Δ is lower in CHX

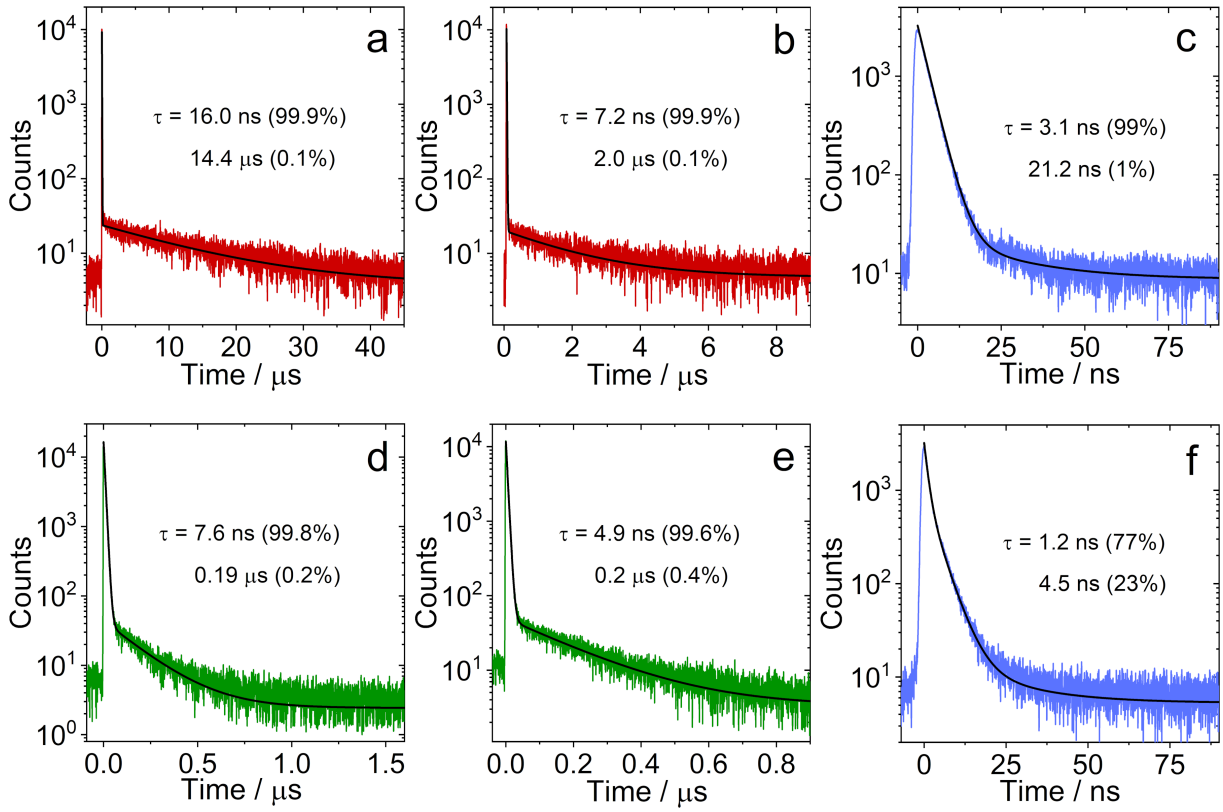

Figure 4: Fluorescence lifetime of **NI-PTZ** under (a) N_2 atmosphere and (d) air atmosphere (λ_{em} = 610 nm, c = 5.0 × 10^{-5} M). Fluorescence lifetime of **NI-PTZ$_2$** under (b) N_2 atmosphere and (e) air atmosphere (λ_{em} = 610 nm, c = 5.0 × 10^{-5} M). Fluorescence lifetime of (c) **NI-PTZ-O** (λ_{em} = 472 nm, c = 1.0 × 10^{-5} M) and (f) **NI-Ph-PTZ** (λ_{em} = 482 nm, c = 1.0 × 10^{-5} M). Excited with a picoseconds pulsed laser (λ_{ex} = 340 nm), in HEX, 20 °C.

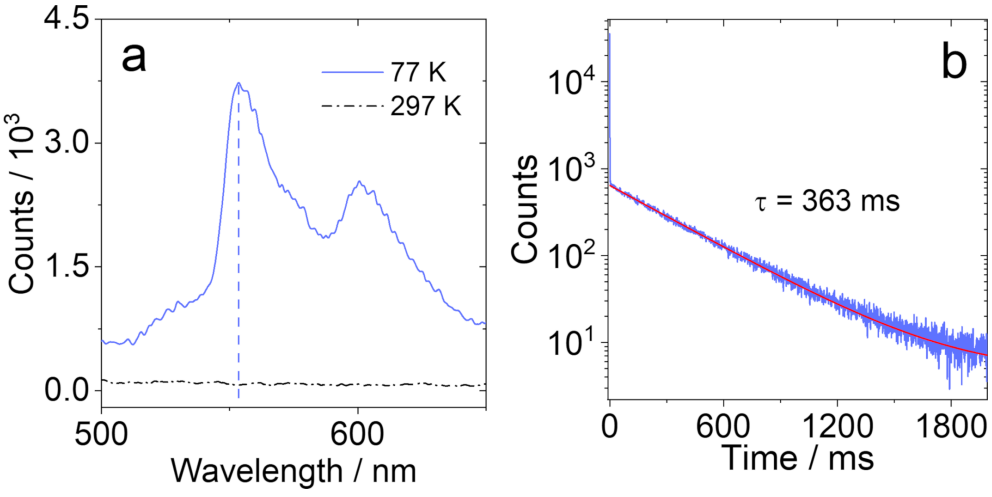

Figure 5: (a) Phosphorescence spectra of **NI-PTZ-O**; (b) decay traces of the phosphorescence of the compounds **NI-PTZ-O**. λ_{ex} = 340 nm, at 77 K, in 2-methyltetrahydrofuran, c = 1.0 × 10^{-5} M.

(Φ_Δ = 8%) and negligible in other solvents with higher polarity. In contrast, **NI-PTZ-O**, **NI-PTZ$_2$**, **NI-Ph-PTZ**, and **NI-PhMe$_2$-PTZ** show much larger Φ_Δ values in HEX (20% to ≈50%), respectively. For **NI-3Br** and **NI-Ph-Br**, Φ_Δ are much larger, up to 100% in dichloromethane (DCM) and ACN, likely due to the heavy-atom effect.

Table 1: Photophysical parameters of the compounds.

Compound	Solvent	λ_{abs} (nm)[a]	ε[b]	λ_{em} (nm)[c]	τ_F (ns)[d]	τ_P (ms)[e]	Φ_F (%)[f]	Φ_Δ (%)[g]
NI-PTZ	CHX	327	1.5	605	9.9 (99.7%) 250 (0.3%)	–[h]	1.9	8
	HEX	325	1.5	644	7.6 (99.8%) 190 (0.2%)		1.7	19
NI-PTZ-O	CHX	329	2.0	468	3.4 (99%) 18.1 (1%)	363	2.0	33
	HEX	327	2.0	472	3.1 (99%) 21.2 (1%)		1.2	37
	TOL	335	2.0	542	4.3 (99%) 19.8 (1%)		2.0	53
NI-PTZ$_2$	CHX	295	2.7	630	5.8 (99.6%) 260 (0.4%)	–[h]	1.9	1
	HEX	301	2.4	644	4.9 (99.6%) 200 (0.4%)		1.7	38
NI-Ph-PTZ	CHX	332	1.4	490	1.3 (54%) 5.4 (46%)	432	4.2	31
	HEX	332	1.4	482	1.2 (77%) 4.5 (23%)		4.1	28
	TOL	336	1.3	585	0.9 (31%) 14.1 (69%)		4.5	34
NI-PhMe$_2$-PTZ	CHX	328	1.6	479	1.6 (56%) 12.9 (44%)	376	1.3	35
	HEX	329	1.6	478	1.2 (51%) 7.2 (49%)		1.0	42
	TOL	333	1.6	595	2.7 (22%) 18.7 (78%)		1.3	40

[a]Maximal UV–vis absorption wavelength, c =1.0 × 10–^{5} M, 20 °C; [b]molar absorption coefficient at absorption maxima, ε: 10^4 M^{-1} cm^{-1}; [c]emission wavelength; [d]fluorescence lifetime, λ_{ex} = 340 nm; [e]phosphorescence lifetime, λ_{ex} = 340 nm, in 2-methyltetrahydrofuran; [f]fluorescence quantum yields determined, λ_{ex} = 330 nm; [g]singlet oxygen quantum yields, $Ru(bpy)_3[PF_6]_2$ was used as standard compound (Φ_Δ = 57% in DCM); [h]not observed.

Table 2: Singlet oxygen quantum yields (Φ_Δ, in%) in different solvents[a].

Compound	CHX	HEX	TOL	DCM	ACN
NI-PTZ	8	19	–[b]	–[b]	–[b]
NI-PTZ-O	33	37	53	90	9
NI-PTZ$_2$	1	38	–[b]	–[b]	–[b]
NI-Ph-PTZ	31	28	34	–[b]	–[b]
NI-PhMe$_2$-PTZ	35	42	40	–[b]	–[b]
NI-3Br	33	38	46	100	100
NI-Ph-Br	30	39	50	100	100

[a]The E_T (30) values of the solvents are 30.9 (CHX), 31.0 (HEX), 33.9 (TOL), 40.7 (DCM), and 45.6 (ACN), respectively, in kcal mol^{-1}. Singlet oxygen quantum yield (Φ_Δ) with $Ru(bpy)_3[PF_6]_2$ as standard (Φ_Δ = 0.57 in DCM) in different solvents, λ_{ex} = 437 nm; [b]not observed.

Electrochemistry study

The redox potentials of the dyads were studied with cyclovoltammetry (Figure 6, Table 3), and the Gibbs free energy changes of the charge separation (ΔG_{CS}) and charge separation states energy levels (E_{CS}) of the compounds were calculated (Table 4). A reversible oxidation wave at +0.36 V (vs Fc/Fc^+) was observed for **NI-PTZ**, which is attributed to the oxidation of the PTZ units. A reversible reduction wave at −1.75 V (vs Fc/Fc^+) was observed, which is attributed to the reduction of the NI moiety. These reduction potentials are similar to the ones previously reported for the **NI-N-PTZ** dyad (+0.39, −1.72). However, for **NI-PTZ-O**, an irreversible oxidation wave at +1.09 V (vs Fc/Fc^+) was observed, which indicates that, upon oxidation, the PTZ moiety becomes a poor electron donor. A reversible reduction wave at −1.57 V was observed, which is cathodically shifted as compared to that of **NI-PTZ**, an expected trend considering the poor electron-donating ability of the oxidized PTZ moiety.

However, the data of **NI-PTZ$_2$** shows less intuitive trends, as a reversible reduction wave is observed at −1.63 V (vs Fc/Fc^+), which is not in line with the presence of two electron-donating PTZ moieties – one would expect, the reduction potential of **NI-PTZ$_2$** should be more negative than the one for **NI-PTZ**. Slightly lower oxidation potentials were observed for **NI-Ph-PTZ** and **NI-PhMe$_2$-PTZ**. However, the 0.04 eV difference in

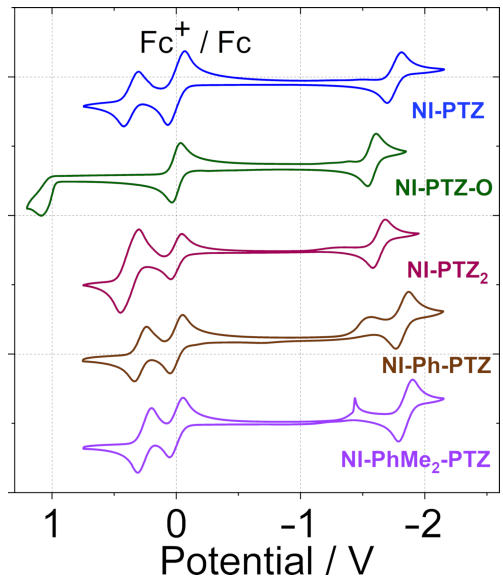

Figure 6: Cyclic voltammograms of the compounds. **NI-PTZ**, **NI-PTZ$_2$**, **NI-Ph-PTZ**, and **NI-PhMe$_2$-PTZ** were studied in deaerated DCM; **NI-PTZ-O** in deaerated ACN. Ferrocene (Fc) was used as internal reference (set as 0 V in the cyclic voltammograms). 0.10 M Bu_4NPF_6 as supporting electrolyte. Scan rates: 100 mV/s, $c = 1.0 \times 10^{-3}$ M, 20 °C.

Table 3: Electrochemical redox potentials of the compounds.[a]

Compound	*E*(ox)/V	*E*(red)/V
NI-PTZ[b]	+0.36	−1.75
NI-PTZ-O[c]	+1.09	−1.57
NI-PTZ$_2$[b]	+0.38	−1.63
NI-Ph-PTZ[b]	+0.29	−1.82
NI-PhMe$_2$-PTZ[b]	+0.25	−1.84
NI-3Br[b]	–[d]	−1.56
NI-N-PTZ[b]	+0.39	−1.72

[a]Cyclic voltammetry in N_2-saturated solvents containing 0.10 M Bu_4NPF_6. Pt electrode as the counter electrode, glassy carbon electrode as the work electrode, ferrocene (Fc/Fc^+) as the internal reference (set as 0 V in the cyclic voltammograms), and $Ag/AgNO_3$ couple as the reference electrode; [b]in DCM; [c]in ACN; [d]not observed.

the oxidation potentials of these two dyads indicates that the different conformational restriction affects the electronic coupling between the NI and PTZ moieties. To help the assignment of the possible CT states in the time-resolved spectra (see later section), the spectroelectrochemistry of the compounds was studied (Figure 7).

For **NI-PTZ**, when a positive potential of +0.53 V (vs $Ag/AgNO_3$) was applied, the hallmark absorption bands of the $PTZ^{\bullet+}$ radical cation centered at 516, 794, and 891 nm are observed [20]. These bands are similar to the ones observed for the previously reported **NI-N-PTZ** dyad. Upon a negative potential at −1.83 V (vs $Ag/AgNO_3$) applied, the absorption bands of the $NI^{\bullet-}$ radical anion at 424, 492, 720, and 801 nm are observed, which are also similar to the ones of the analogous dyad [20]. For **NI-PTZ-O**, similar $NI^{\bullet-}$ absorption bands were observed. However, the $PTZ^{\bullet+}$ absorption bands of **NI-PTZ-O** are less resolved as compared to those of **NI-PTZ** (Figure 7a). These results indicate the effect of oxidation of the PTZ moiety.

The spectroelectrochemistry traces of **NI-Ph-PTZ**, **NI-PTZ$_2$**, and **NI-PhMe$_2$-PTZ** were also studied (Supporting Information File 1, Figure S31). For **NI-Ph-PTZ**, the $NI^{\bullet-}$ absorption bands in the 350–600 nm range are less resolved than for **NI-PTZ**. This likely comes from the effect of the π-conjugation of the phenyl ring with the NI moiety in **NI-Ph-PTZ**. In contrast, the $PTZ^{\bullet+}$ absorption band of **NI-Ph-PTZ** resembles the one of **NI-PTZ**, indicating that the spin density of $PTZ^{\bullet+}$ in **NI-Ph-PTZ** is confined on the PTZ moiety, and does not significantly spread on the phenyl linker. The spectroelectrochemistry of **NI-PhMe$_2$-PTZ** shows that the $NI^{\bullet-}$ absorption band in this dyad is similar to that of **NI-PTZ**, but not to the one of

Table 4: Gibbs free energy changes of the charge separation (ΔG_{CS}) and charge separation states energy (E_{CS}) of the compounds[a].

Compound	ΔG_{CS} (eV)				E_{CS} (eV)			
	HEX	TOL	DCM	ACN	HEX	TOL	DCM	ACN
NI-PTZ[b]	−0.38	−0.51	−0.85	−0.95	2.28	2.15	1.81	1.71
NI-PTZ-O[c]	−0.23	−0.29	−0.47	−0.52	2.88	2.81	2.63	2.58
NI-PTZ$_2$[d]	−0.29	−0.34	−0.93	−1.06	2.39	2.24	1.75	1.62
NI-Ph-PTZ[e]	−0.04	−0.28	−1.10	−1.31	2.98	2.74	1.92	1.71
NI-PhMe$_2$-PTZ[f]	−0.07	−0.32	−1.16	−1.37	3.00	2.75	1.91	1.70

[a]Cyclic voltammetry in deaerated solutions containing 0.10 M Bu_4NPF_6. Pt electrode as counter electrode, glassy carbon electrode as working electrode, and $Ag/AgNO_3$ couple as the reference electrode; [b]E_{00} = 2.66 eV; [c]E_{00} = 3.11 eV; [d]E_{00} = 2.68 eV; [e]E_{00} = 3.02 eV; [f]E_{00} = 3.07 eV. E_{00} ($E_{00} = 1240/\lambda$) is the singlet state energy of compounds, λ is the wavelength of the crossing point of normalized UV–vis absorption spectra and fluorescence emission spectra.

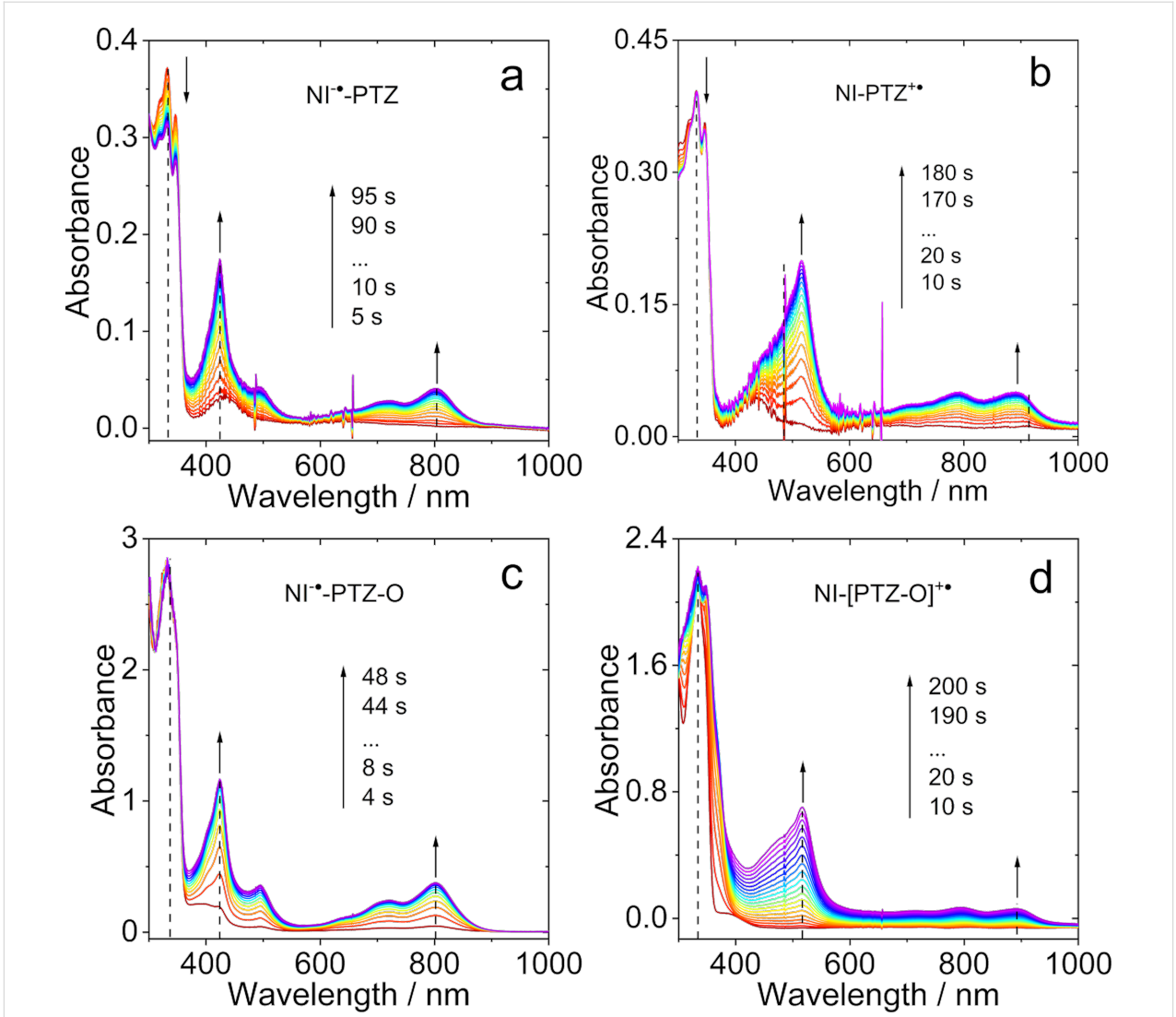

Figure 7: Spectroelectrochemistry traces of the UV–vis absorption spectra for (a) **NI-PTZ** observed from neutral (red) to monoanion (purple) with a potential of –1.83 V applied; (b) **NI-PTZ** observed from neutral (red) to monocationic (purple) at a potential of 0.53 V applied; (c) **NI-PTZ-O** observed from neutral (red) to monoanion (purple) at controlled-potential of –1.80 V; (d) **NI-PTZ-O** observed from neutral (red) to monocationic (purple) at controlled-potential of 2.00 V. In deaerated DCM containing 0.10 M $Bu_4[NPF_6]$ as supporting electrolyte and with $Ag/AgNO_3$ as reference electrode, 20 °C.

NI-Ph-PTZ. This illustrates the impact of the conformational restriction on the photophysical properties of **NI-PhMe$_2$-PTZ**.

We underline that the absorption of the CT states of the dyads may not be the "*simple sum*" of the absorption of the radical cation and the radical anion of the dyads, obtained by the spectroelectrochemistry (Figure 7). The reason is that, in spectroelectrochemistry, one forms either $D^{\bullet+}$–A or D–$A^{\bullet-}$, but not $D^{\bullet+}$–$A^{\bullet-}$. When photoexciting the dyads, however, the CT ($D^{\bullet+}$–$A^{\bullet-}$) state is formed resulting in a different exciton binding energy related to the interaction between the radical anion and cation; this interaction being far from negligible in *compact* dyads.

Nanosecond transient absorption (ns-TA) spectra

In order to identify the lowest-lying transient species of the dyads and the triad formed upon photoexcitation, the ns-TA spectra of the compounds were recorded (Figure 8). For the reference **NI-3Br** (Figure S33a, Supporting Information File 1), sharp excited state absorption (ESA) bands centered at 360 and 470 nm were observed in HEX, and a 63 µs lifetime was determined. For **NI-PTZ**, positive absorption bands centered at 360, 470, 390, and 520 nm were observed upon pulsed laser in HEX (Figure 8a). This absorption profile drastically differs from the absorption of the radical anion and the cation (see Figure 7a and b) and that of **NI-3Br**. It is also different from the previously

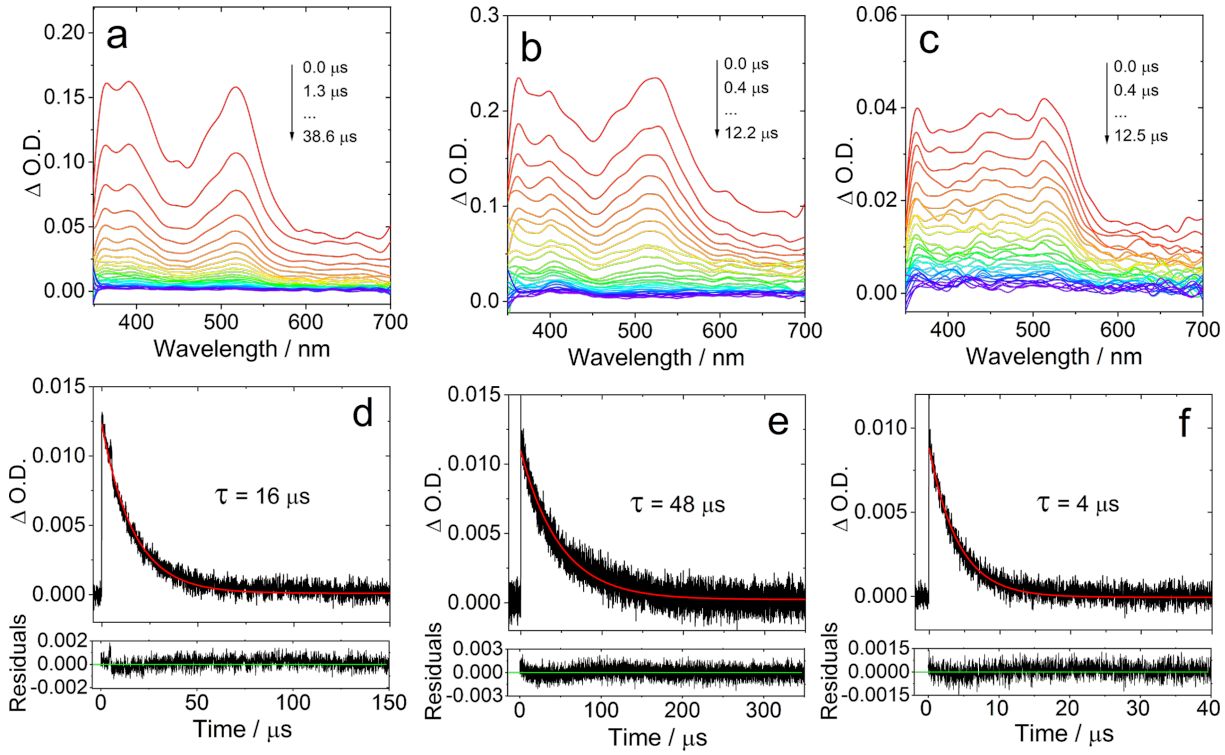

Figure 8: Nanosecond transient absorption spectra of (a) **NI-PTZ** (c = 1.5 × 10^{-4} M), (b) **NI-PTZ-O** (c = 2.5 × 10^{-4} M), and (c) **NI-PTZ$_2$** (c = 5.0 × 10^{-5} M). The corresponding decay traces are (d) **NI-PTZ** (c = 5.0 × 10^{-6} M) at 520 nm, (e) **NI-PTZ-O** (c = 2.0 × 10^{-6} M) at 530 nm, and (f) **NI-PTZ$_2$** (c = 6.0 × 10^{-6} M) at 510 nm. In deaerated HEX, λ_{ex} = 355 nm, 20 °C.

studied analogous dyad, for which a CT state was observed [20]. Thus, we tentatively propose that a ^{3}LE state was observed for **NI-PTZ**. The lifetime of the transient species was determined as 16 μs. This lifetime is much longer than that observed for the analogous dyad (2.6 μs), which was assigned to a CT state [20]. This conclusion is supported by the fact that the ^{3}LE state energy (2.27 eV) of **NI-PTZ** is slightly lower than its CT state (2.34 eV, approximated from the CT emission band, Figure 3a). Discrepancy results were observed for **NI-PTZ$_2$** (Figure 8c) and the lifetime was determined to be 4 μs (Figure 8f). In this case the ^{3}LE and CT states share similar energy, the CT state energy is 2.25 eV (approximated from the CT emission band, Figure 3c), and the ^{3}LE state energy, 2.27 eV. Observation of a long-lived CT state in compact donor–acceptor dyads is rare [49-51], the CR of ^{3}CT→S_0 is spin forbidden, the ^{3}CT state should be longer-lived than the ^{1}CT state, which is attributed to the electron spin control effect [15,52-57]. These results confirm that the molecules showing TADF can have either a lowest-lying CT state or a lowest-lying ^{3}LE state.

The ns-TA spectra of **NI-PTZ-O** were also studied (Figure 8b). Upon oxidation of the PTZ moiety, the CT state energy increases by 0.6 eV as compared to that of **NI-PTZ** (Table 4). However, the ESA bands of **NI-PTZ-O** are close to those of **NI-PTZ**. Thus, we tentatively assign the transient species as ^{3}LE state of **NI-PTZ-O**, and that the ^{3}LE state stands as the lowest-lying triplet state with an energy of 2.29 eV based on the low temperature phosphorescence, significantly below the estimated value of 2.88 eV for the CT state (approximated from the CT absorption band, Figure 1). The longer lifetime of **NI-PTZ-O** infers that for **NI-PTZ**, CT state sharing similar energy with ^{3}LE may drain the excited state and shorten the triplet state lifetime.

The ns-TA spectra of **NI-Ph-PTZ** and **NI-PhMe$_2$-PTZ** were also studied (Figure S32 in Supporting Information File 1). For these two dyads, especially **NI-PhMe$_2$-PTZ**, the ESA bands and the triplet state lifetimes (43 μs) are similar to those of **NI-3Br**, and the ^{3}LE state is therefore observed in these two dyads. Interestingly, the conformation restriction in **NI-PhMe$_2$-PTZ** leads to literally the same ESA bands as in **NI-3Br**. Due to the large separation of the electron donor and acceptor, the CT state energy is increased by ca. 0.7 eV as compared to that of **NI-PTZ** (Table 4). In **NI-PhMe$_2$-PTZ**, the CT state energy is 3.02 eV (approximated from the CT emission band, Figure S26

in Supporting Information File 1), and the ^{3}LE state energy attains 2.27 eV (approximated from the low temperature phosphorescence). For **NI-Ph-PTZ**, the CT state energy is 2.99 eV (approximated from the CT emission band, Figure 3d), and the ^{3}LE state energy is 2.24 eV (approximated from the low temperature phosphorescence). Therefore, it is evident that the ^{3}LE state is the lowest-lying triplet state in both **NI-Ph-PTZ** and **NI-PhMe$_2$-PTZ**.

It is known that the CT state energy decreases substantially when increasing the solvent polarity. For instance, in **NI-PTZ,** the CT state lies at 2.28 eV in HEX (Table 4), but only at 1.71 eV in ACN, whereas the ^{3}LE state is much less sensitive to the polarity and remains at ca. 2.27 eV. Therefore, the ns-TA spectra of the dyads in ACN were studied as well (Figure S34 in Supporting Information File 1). For **NI-PTZ**, positive absorption bands centered at 420 nm and a minor band at 510 nm were observed. These absorption bands are different from the ns-TA of **NI-PTZ** in HEX, however, a feature which is similar to the one found in **NI-N-PTZ** [20]. In other words, the transient species of **NI-PTZ** in ACN upon photoexcitation corresponds to be a CT rather than the ^{3}LE state. The CT state lifetime was determined to be 0.37 µs (Figure S34b, Supporting Information File 1), and it is ca. twice longer than the CT state lifetime of **NI-N-PTZ** measured in the same experimental conditions (ca. 0.16 µs, Figure S34d). The CT state lifetime of **NI-PTZ** is rather long, considering the compact dyad structure and the low CT energy in ACN (ca. 1.71 eV). For **NI-PTZ$_2$**, the CT state was measured in ACN as well, and a 189 ns lifetime was determined (Figure S35a in Supporting Information File), hinting that the CT state observed in the **NI-PTZ$_2$** ns-TA experiments is in fact a ^{3}CT state, rather than a ^{1}CT state. Indeed, the luminescence studies have shown that the lifetime of ^{1}CT state is short with prompt fluorescence on ns timescale.

In comparison, we also studied the triplet state ns-TA spectra of the reference compound **NI-3Br** in ACN (see Supporting Information File 1, Figure S33c), and the data were compared to the ns-TA spectra in HEX. The results show that **NI-3Br** has similar ns-TA spectral features in both HEX and ACN, and the triplet state lifetime are similar in both solvents (63 µs and 118 µs, respectively). Similar results were observed for **NI-Ph-Br,** the triplet state lifetimes are 45 µs and 108 µs in HEX and ACN, respectively (Figure S36, Supporting Information File 1). For **NI-PTZ-O**, ^{3}LE and ^{3}CT states were observed in ACN, and the lifetime was determined as 71 µs (Figure S35c).

Computational investigations

To explain the experimental results, quantum chemical calculations were used to obtain additional insights into both the excited states involved and the photo-deactivation dynamics. First, the ground state geometry of the compounds was optimized (Figure 9). For the compact **NI-PTZ** and **NI-PTZ-O** dyads, the two units adopt almost orthogonal geometry. A similar result was observed for the triad **NI-PTZ$_2$**. For the dyads containing a phenyl linker between the NI and the PTZ

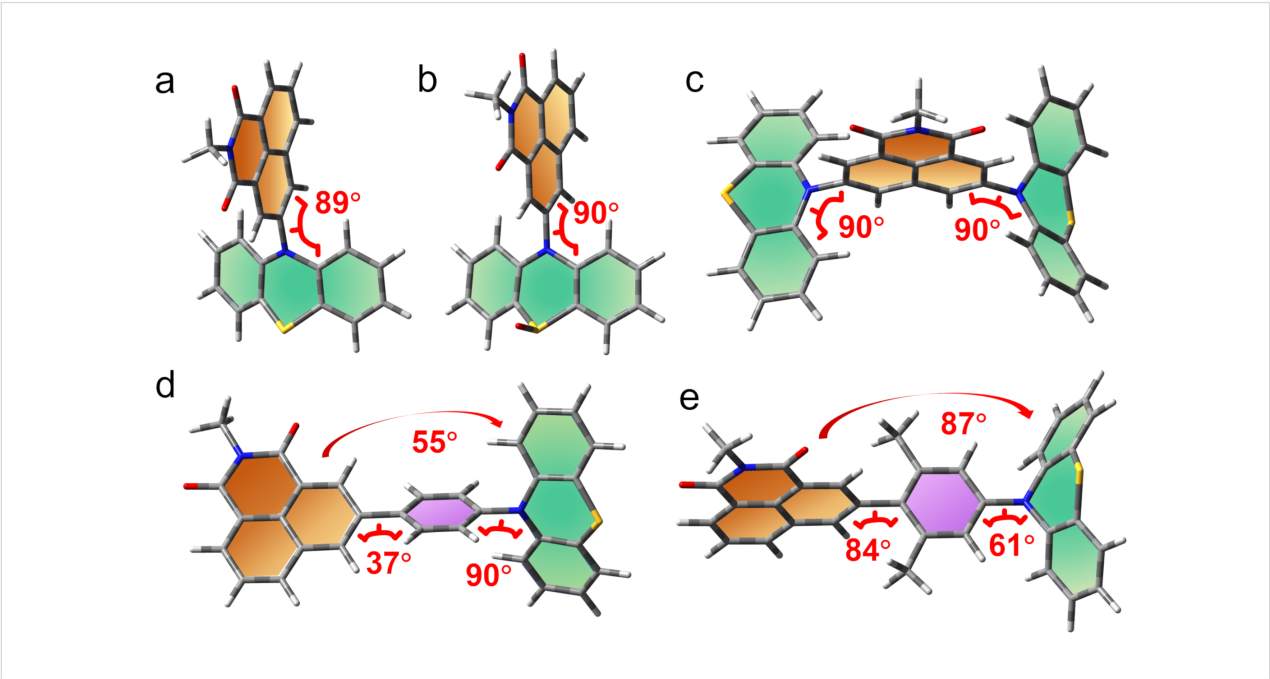

Figure 9: Optimized ground state geometry of (a) **NI-PTZ**, (b) **NI-PTZ-O**, (c) **NI-PTZ$_2$**, (d) **NI-Ph-PTZ**, and (e) **NI-PhMe$_2$-PTZ**; the green and orange sheets show the planes of the donor and the receptor.

moieties, the steric hindrance imposed by the methyl substituents on the phenyl linker is significant: the dihedral angle between the NI and the phenyl linker is 37° only in **NI-Ph-PTZ**, but it increases up to 84° in **NI-PhMe$_2$-PTZ**. In **NI-Ph-PTZ**, the dihedral angle between the NI and the PTZ is ca. 55°, and it increases up to 87° in **NI-PhMe$_2$-PTZ**.

As shown in Table S1 (Supporting Information File 1), for all compounds, S_1 corresponds to a HOMO→LUMO electronic transition (see the molecular orbitals involved in Figure 10) at the Franck–Condon region. The spatial separation between the HOMO and LUMO orbitals along with the very small calculated oscillator strengths (see Table S1 and Table S2, Supporting Information File 1) are clear indicators of a CT character for S_1. Relaxation on the lowest triplet excited state potential energy surfaces leads to different scenarios for the studied compounds as shown in Table S2: a ^{3}CT character is found for the lowest triplet excited state (T_1) of **NI-PTZ** and a considerable ^{3}CT character is found for the T_1 of **NI-N-PTZ** and **NI-PTZ$_2$**. Conversely, for **NI-PhMe$_2$-PTZ**, **NI-Ph-PTZ**, and **NI-PTZ-O** a predominant ^{3}LE character is found at the T_1 optimized minima (see Table S2). Note that, at the Frank–Condon region, T_1 corresponds to a ^{3}LE state for all the compounds (see Table S1). Thus, in **NI-PTZ-O**, the relaxation on the T_1 and T_2 potential energy surfaces leads to the same state ordering between the ^{3}LE and ^{3}CT states with respect to the Franck–Condon region, i.e., the ^{3}LE state remains the lowest triplet excited state at both the Franck–Condon region and at its optimized geometry. T_1 corresponds to a ^{3}LE state localized on the acceptor ligand and it predominantly involves a HOMO-2-to-LUMO electronic excitation (see Figure 10 for the orbitals). For the same compound, T_2 corresponds to a HOMO→LUMO transition with a predominant ^{3}CT character. The computed triplet energies (see Table S2) are in reasonable agreement with the experimental ones. More in details, the experimental emission maximum for the for ^{3}LE band peaks at 2.29 eV, which reasonably matches the computed one (2.02 eV). Note that experimentally, the ^{3}LE state was still observed to be the lowest triplet state for **NI-PTZ**. In this respect, the computed energetic difference between T_1 and T_2 falls within the typical TD-DFT error bar (ca. 0.3 eV), which explains the difference in state ordering between experiments and calculations. Note also, that the experimental results point to a small energetic difference between the ^{3}LE and ^{3}CT states, as triplet state lifetime is shorter than the pristine ^{3}NI state.

For completeness, Table S3 (Supporting Information File 1) reports the adiabatic and vertical energies of the ^{3}LE and ^{3}CT states for **NI-PTZ** and **NI-PTZ-O** (as representative cases of the different photophysical scenarios within the series of compounds) along with the state ordering at the ^{1}CT optimized geometries. Comparing **NI-PTZ-O** with **NI-PTZ** at their ^{1}CT

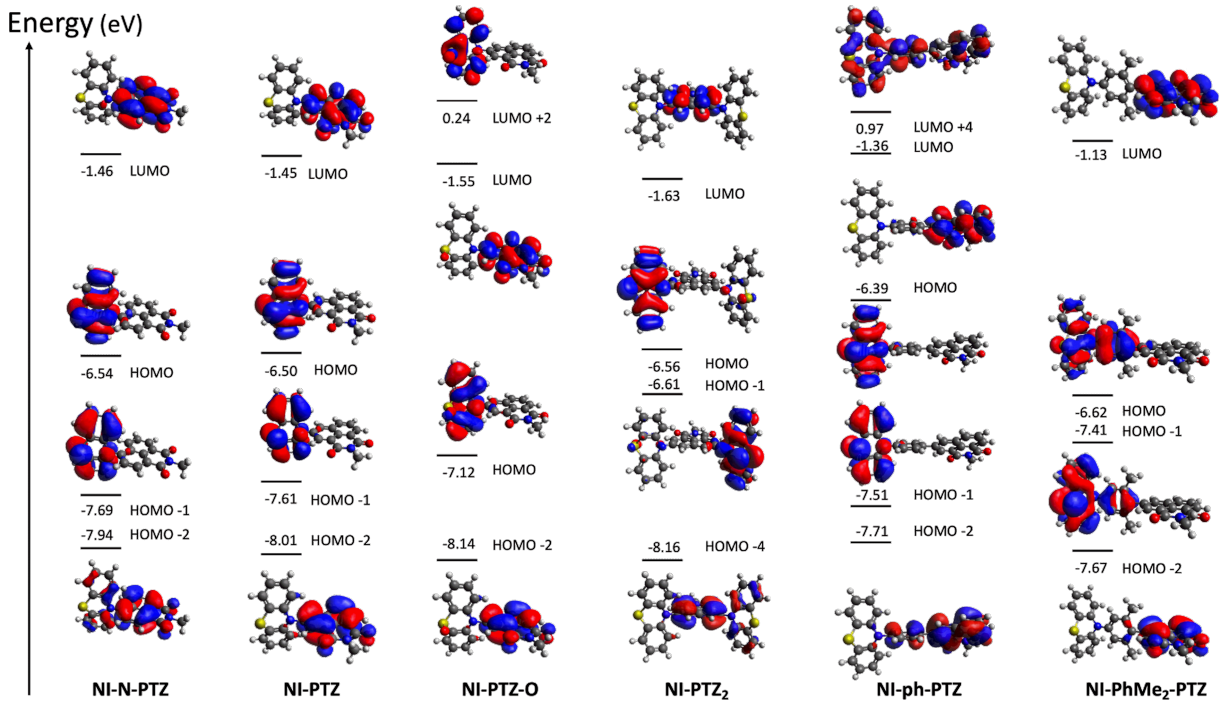

Figure 10: Kohn–Sham frontier molecular orbitals (CAM-B3LYP/6-31G(d) in gas phase) involved in S_1, T_1, and T_2 of **NI-N-PTZ**, **NI-PTZ**, **NI-PTZ-O**, **NI-PTZ$_2$**, **NI-Ph-PTZ**, and **NI-PhMe$_2$-PTZ**, based on the optimized ground state geometries. An isovalue of 0.02 is used.

optimized geometries, a different ordering of the triplet excited states is obtained. More in details, for **NI-PTZ-O**, both ^{3}LE (2.63 eV) and ^{3}CT (3.09 eV) are lower in energy than the ^{1}CT state (3.12 eV), but for **NI-PTZ** the ^{3}LE state (2.74 eV) is higher in energy than the ^{1}CT state (2.60 eV), while ^{3}CT remains slightly lower in energy (2.57 eV). This has some important consequences on the TADF mechanisms.

Table 5 lists spin–orbit couplings matrix elements (SOCMEs) between ^{1}CT, ^{3}LE, and ^{3}CT states. The SOCMEs between ^{1}CT and ^{3}CT are small, 0.03 cm^{-1} at most, which was expected as they involve the same electronic transitions. Conversely, the SOCMEs between ^{1}CT and ^{3}LE amount up to 0.47 cm^{-1} in the case of **NI-PTZ-O**. For **NI-PTZ** the computed ISC rate from ^{1}CT towards ^{3}LE attains to 2.92×10^7 s^{-1}, which is two orders of magnitude larger than the ISC rate towards ^{3}CT (8.51×10^5 s^{-1}). The RISC from ^{3}CT (2.79×10^5 s^{-1}) back to ^{1}CT is large enough to compete with other photodeactivation processes, so TADF is likely. In order to further proof this, we also calculated the phosphorescence rate (k_{phos}; see Experimental section, Computational details). The computed k_{phos} amounts up to 6.85×10^{-1} s^{-1}, thus confirming that phosphorescence from ^{3}CT is not competitive with RISC, also in agreement with the experimental evidences. For **NI-PTZ-O**, the fastest rate of ISC is found for the ^{1}CT→^{3}LE transition (4.12×10^6 s^{-1}). Conversely, the RISC process from the ^{3}LE state is very unlikely to occur, as the back process to ^{1}CT is characterized by a large energy gap (ca. 0.49 eV, see Table S3 in Supporting Information File 1), thus explaining the different TADF properties experimentally measured for **NI-PTZ-O** and **NI-PTZ**. The analysis of the computed reorganization energies for selected (R)ISC processes of **NI-PTZ-O** and **NI-PTZ** and the activation barriers derived from these values clearly highlight the same trends obtained with the rate calculations [58]. For instance, a negligible RISC decay rate for the ^{3}LE→^{1}CT process in **NI-PTZ-O** roots on a large adiabatic energy difference and an even larger reorganization energy (0.75 and 1.92 eV, respectively), which lead to an activation barrier of ca. 3.42 eV (see details in Supporting Information File 1). Conversely, the sizable value of the RISC rate for the for the ^{3}LE→^{1}CT process in **NI-PTZ** roots on a small adiabatic energy difference and a similar value for the reorganization energy (0.23 vs 0.53 eV, respectively). This results in an activation barrier for the RISC process of ca. 0.076 eV, which is small enough to enable the RISC process at room temperature.

In Scheme 2, a summary of the photodeactivation pathways for **NI-PTZ** and **NI-PTZ-O** is presented. In addition, the impact of solvent on the energy of the states is included. When moving from apolar to polar solvents a little increase in the energy gap between ^{1}CT and ^{3}LE is observed (amounting to up to 0.13 eV in acetonitrile), which is mostly due to the stabilization of ^{3}LE (0.23 eV for **NI-PTZ** and 0.30 eV for **NI-PTZ-O**) while the ^{1}CT state is only stabilized by 0.10 eV and 0.17 eV, respectively for both **NI-PTZ** and **NI-PTZ-O**. Comparing the computed energies (Scheme 2) with the experimental energies (see Table 4) results in a reasonable agreement, especially in a polar solvent (ACN), where the experimental energy of **NI-PTZ** for the ^{1}CT state is 1.71 eV and the computed energy, 1.74 eV. For **NI-PTZ-O** the experimental energy of the ^{3}CT in ACN is 2.58 eV, while the computed energy, 2.82 eV, deviates more from the experiment (0.24 eV), but remains in a reasonable agreement with the measured values. The CT character of the ^{1}CT and ^{3}CT states is visible in the electronic density difference (EDDs) plots shown in Scheme 2, which clearly indicates the flow of electron density from the PTZ to the NI moieties. Conversely, the LE states are fully localized within the acceptor fragment.

Conclusion

In order to study the impact of the energy matching between the charge-transfer (CT) and localized triplet excited (^{3}LE) states on the thermally activated delayed fluorescence (TADF), a series of compact electron donor–acceptor dyads and a triad

Table 5: Calculated SOCMEs (cm^{-1}) and computed rates (s^{-1}) along with selected reorganization energies (values between brackets in eV) for the (R)ISC processes **NI-PTZ** and **NI-PTZ-O**.

Molecule	SOCME (cm^{-1})		k_{ISC} (s^{-1})[a]		k_{RISC} (s^{-1})[a]	
	^{1}CT–^{3}LE	^{1}CT–^{3}CT	^{1}CT–^{3}LE	^{1}CT–^{3}CT	^{1}CT–^{3}LE	^{1}CT–^{3}CT
NI-PTZ	0.33	0.03	2.92×10^7	8.51×10^5	3.79×10^5 (0.53)[b]	2.79×10^5
NI-PTZ-O	0.47	0.02	4.12×10^6	1.23×10^5	0 (1.92)[b]	8.13×10^4

[a]Rates obtained by making use of the vertical hessian model as implemented in FCclasses. All computations are performed in the gas phase.
[b]Reorganization energies (in eV) for the RISC processes.

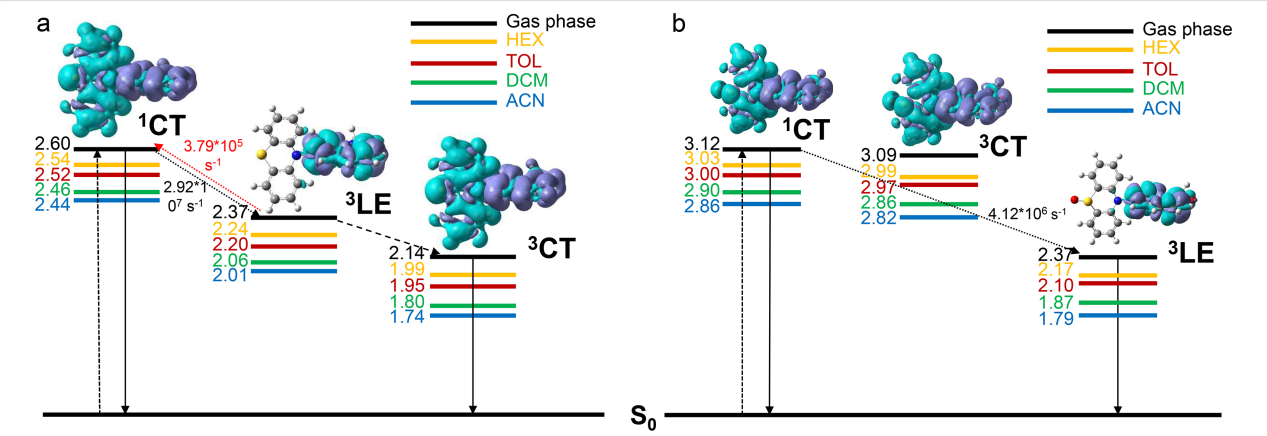

Scheme 2: Jablonski diagram of (a) **NI-PTZ** and (b) **NI-PTZ-O**, including electron density difference (EDD) at T_2 (^{3}LE) geometry and computed in gas phase. EDD isovalues are 0.02 au. The cyan and blue lobes of the EDD indicate increase and decrease of electron density, respectively. The energies in eV were obtained with single point calculations on optimized S_1, T_1, and T_2 geometry in HEX, DCM, TOL, and ACN.

were prepared. In the dyads and the triad, naphthalimide (NI) was used as electron acceptor and phenothiazine (PTZ) as electron donor. The NI and PTZ moieties are either directly connected at the 3-position of NI and the *N*-position of the PTZ moiety via a C–N single bond, or connected through an intervening phenyl linker. Tuning the electron-donating ability of the PTZ unit, and consequently the CT state energy, was achieved by its oxidation to yield the corresponding sulfoxide. The conformation restriction was imposed through introducing *ortho*-methyl substituents on the phenyl linker. TADF was observed for the dyads and the triad, indicated by the biexponential fluorescence decay, for instance 16.0 ns (99.9%)/14.4 µs (0.1%). Singlet oxygen photosensitizing experiments showed that the Φ_Δ of **NI-PTZ** is moderate in HEX (Φ_Δ = 19%), but that upon oxidation of the PTZ unit in the dyad much larger values were observed for the resulted dyad **NI-PTZ-O** (up to 90% in DCM) due to the increase of the CT state energy. In nanosecond transient absorption spectra in HEX, in general a ^{3}LE state was observed (lifetime: 16–48 µs). For all the compounds, CT emission bands were observed in HEX. In polar solvents, CT state was observed for **NI-PTZ**, **NI-N-PTZ**, and **NI-PTZ$_2$** (lifetime: 156–365 ns). Computational investigations unambiguously unraveled the origins of TADF in **NI-PTZ**. Our investigations also underpin the striking photophysical behavior of **NI-PTZ-O** (i.e., phosphorescence and absence of TADF) which originates from a different excited state ordering between the ^{3}CT and ^{3}LE states in **NI-PTZ** and **NI-PTZ-O**. The tuning of the energy order of the ^{3}CT and ^{3}LE state is achieved by the feasible oxidation of the PTZ unit in the dyads, while the other factors kept intact; this approach may become a promising methodology in the study of the entangled excited states and the photophysical processes of TADF molecules based on the electron donor–acceptor dyads structure motif. These studies are also useful to understand the subtle entanglement of the ^{1}LE, ^{1}CT, ^{3}CT, and ^{3}LE states of TADF based on electron donor–acceptor dyads, as well as the photophysical processes of these dyads upon photoexcitation.

Experimental

General methods

All the chemicals used in synthesis are analytical pure and were used as received without purification. UV–vis absorption spectra were measured on a UV-2550 spectrophotometer (Shimadzu Ltd., Japan). Fluorescence emission spectra were recorded with an FS5 spectrofluorometer (Edinburgh instruments Ltd., U.K.). Fluorescence quantum yields (Φ_F) were measured by an absolute photoluminescence quantum yield spectrometer (Quantaurus-QY Plus C13534-11, Hamamatsu Ltd., Japan). Luminescence lifetimes of compounds were recorded with an OB920 luminescence lifetime spectrometer (Edinburgh Instruments Ltd., U.K.). **NI-PTZ**, **NI-PTZ-O**, **NI-PTZ$_2$**, **NI-Ph-PTZ**, and **NI-PhMe$_2$-PTZ** were prepared according to the literature methods [21,59].

Synthesis of **NI-PTZ**

Compound **NI-PTZ** was synthesized in a manner similar to [21]. Under N_2 atmosphere, **NI-3Br** (468.0 mg, 1.209 mmol), phenothiazine (289.0 mg, 1.452 mmol), $Pd(OAc)_2$ (49.2 mg, 0.219 mmol) and sodium *tert*-butoxide (760.0 mg, 7.908 mmol) were dissolved in dry toluene (22 mL). Then tri-*tert*-butylphosphine tetrafluoroborate (66.4 mg, 0.229 mmol) was added. The mixture was refluxed and stirred for 8 h under N_2. After cooling, water (20 mL) was added, and the mixture was extracted with ethyl acetate (80 mL). The organic layer was separated and washed with water and brine (3 × 30 mL), respectively. The organic layer was combined, dried over anhydrous Na_2SO_4, and the solvent was evaporated under reduced pressure. The crude product was purified by column chromatography (silica gel,

DCM/PE 1:3, v:v). Compound **NI-PTZ** was obtained as orange solid. Yield: 570 mg (93.1%). Mp 61.9–62.7 °C; ^{1}H NMR ($CDCl_3$, 400 MHz) δ 0.88 (t, *J* = 14.17 Hz, 3H), 0.94 (t, *J* = 14.89 Hz, 3H), 1.29–1.34 (m, 4H), 1.36–1.41 (m, 4H), 1.93–1.97 (m, 1H), 4.07–4.17 (m, 2H), 6.61 (d, *J* = 7.99 Hz, 2H), 6.97–7.03 (m, 4H), 7.22 (d, *J* = 7.63 Hz, 2H), 7.75–7.77 (m, 1H), 8.08 (s, 1H), 8.13 (d, *J* = 8.18 Hz, 1H), 8.57 (s, 1H), 8.58 (s, 1H); ^{13}C NMR ($CDCl_3$, 125 MHz) δ 164.40, 163.96, 141.60, 138.00, 133.34, 130.84, 130.44, 129.54, 127.72, 127.22, 126.37, 125.31, 125.01, 124.16, 122.85, 119.77, 44.36, 37.97, 30.77, 29.70, 28.71, 24.08, 23.10, 10.66; HRMS–MALDI (*m*/*z*): $[M + H]^+$ calcd for $C_{32}H_{30}N_2O_2S$, 506.2028; found, 506.2023.

Synthesis of **NI-PTZ-O**

Compound **NI-PTZ-O** was synthesized in a manner similar to [59]. Compound **NI-PTZ** (200 mg, 0.4 mmol) was dissolved in glacial acetic acid (28 mL), H_2O_2 (8.2 mL, 30%, 6.5 mmol) was added dropwise. The mixture was stirred at 40 °C overnight. The mixture was poured into water and the pH of the mixture was brought to 7 with a saturated aqueous solution of Na_2CO_3. After cooling, water (20 mL) was added, and the mixture was extracted with ethyl acetate (80 mL). The organic layer was separated and washed with water and brine solution (3 × 30 mL), respectively. The organic layer was dried over anhydrous Na_2SO_4 and the solvent was evaporated under reduced pressure. The crude product was purified by column chromatography (silica gel, DCM/MeOH 50:1, v:v). **NI-PTZ-O** was obtained as yellow solid. Yield: 180 mg (87.2%). Mp 176.2–177.2 °C; ^{1}H NMR ($CDCl_3$, 400 MHz) δ 0.88–0.98 (m, 6H), 1.27–1.43 (m, 8H), 1.95–2.01 (m, 1H), 4.11–4.22 (m, 2H), 6.67 (d, *J* = 8.26 Hz, 2H), 7.29 (d, *J* = 7.38 Hz, 2H), 7.38–7.42 (m, 2H), 7.88–7.92 (m, 1H), 8.05 (d, *J* = 7.38 Hz, 2H), 8.28 (d, *J* = 8.00 Hz, 1H), 8.42 (s, 1H), 8.62 (s, 1H), 8.76 (d, *J* = 7.13 Hz, 1H); ^{13}C NMR ($CDCl_3$, 125 MHz) δ 164.51, 139.11, 138.73, 138.17, 133.68, 133.51, 132.44, 131.95, 131.22, 130.44, 127.36, 123.27, 122.83, 121.64, 44.27, 37.98, 30.75, 28.71, 24.07, 23.10, 20.81, 10.66; HRMS–MALDI (*m*/*z*): $[M + H]^+$ calcd for $C_{32}H_{30}N_2O_3S$, 522.1977; found, 523.2050.

Synthesis of **NI-PTZ$_2$**

Compound **NI-PTZ$_2$** was synthesized in a manner similar to [21]. Under N_2 atmosphere, compound **1** (190.0 mg, 0.409 mmol), phenothiazine (294.5 mg, 1.478 mmol), $Pd(OAc)_2$ (36 mg, 0.160 mmol), and sodium *tert*-butoxide (317.0 mg, 3.299 mmol) were dissolved in dry toluene (12 mL). Then, tri-*tert*-butylphosphine tetrafluoroborate (53.0 mg, 0.183 mmol) was added. The mixture was refluxed and stirred for 24 h under N_2. After cooling, water (20 mL) was added, and the mixture was extracted with ethyl acetate (80 mL). The organic layer was separated and washed with water and brine (3 × 30 mL), respectively. The organic layer was dried over anhydrous Na_2SO_4 and the solvent was evaporated under reduced pressure. The crude product was purified by column chromatography (silica gel, DCM/PE 1:4, v:v). Compound **NI-PTZ$_2$** was obtained as orange solid. Yield: 230 mg (80.0%). Mp 100.1–101.0 °C; ^{1}H NMR ($CDCl_3$, 400 MHz) δ 0.86–0.94 (m, 6H), 1.30–1.41 (m, 8H), 1.90–1.96 (m, 1H), 4.03–4.14 (m, 2H), 6.77 (m, 4H), 7.01–7.11 (m, 8H), 7.25 (d, *J* = 1.51 Hz, 2H), 7.86 (d, *J* = 2.12 Hz, 2H), 8.46 (d, *J* = 2.12 Hz, 2H); ^{13}C NMR ($CDCl_3$, 125 MHz) δ 163.94, 142.79, 135.00, 127.96, 127.82, 126.96, 126.23, 124.62, 123.50, 121.13, 44.52, 37.95, 30.75, 29.70, 28.72, 24.06, 23.10, 10.66; HRMS–MALDI (*m*/*z*): $[M + H]^+$ calcd for $C_{44}H_{37}N_3O_2S_2$, 703.2327; found, 703.2322.

Synthesis of **NI-Ph-PTZ**

Compound **NI-Ph-PTZ** was synthesized in a manner similar to [21]. Under N_2 atmosphere, compound **2** (51 mg, 0.110 mmol), phenothiazine (26.3 mg, 0.132 mmol), $Pd(OAc)_2$ (4.5 mg, 0.020 mmol), and sodium *tert*-butoxide (69.1 mg, 0.720 mmol) were dissolved in dry toluene (3 mL). Then, tri-*tert*-butylphosphine tetrafluoroborate (6.1 mg, 0.021 mmol) was added. The mixture was refluxed and stirred for 8 h under N_2. After cooling, water (20 mL) was added, and the mixture was extracted with ethyl acetate (80 mL). The organic layer was separated and washed with water and brine solution (3 × 30 mL), respectively. The organic layer was dried over anhydrous Na_2SO_4 and the solvent was evaporated under reduced pressure. The crude product was purified by column chromatography (silica gel, DCM/PE 6:1, v:v). The product **NI-Ph-PTZ** was obtained as yellow solid. Yield: 40 mg (62.4%). Mp 126.7–128.3 °C; ^{1}H NMR ($CDCl_3$, 400 MHz) δ 0.94–0.97 (m, 6H), 1.33–1.42 (m, 8H), 1.97 (s, 1H), 4.12–4.22 (m, 2H), 6.41 (d, *J* = 6.75 Hz, 2H), 6.87–6.93 (m, 4H), 7.10 (d, *J* = 6.63 Hz, 2H), 7.54 (d, *J* = 7.13 Hz, 2H), 7.80–7.83 (m, 1H), 7.99 (d, *J* = 6.63 Hz, 2H), 8.29 (d, *J* = 8.13 Hz, 1H), 8.46 (s, 1H), 8.62 (d, *J* = 6.38 Hz, 1H), 8.94 (s, 1H); ^{13}C NMR ($CDCl_3$, 125 MHz) δ 164.54, 139.04, 138.63, 133.96, 132.17, 131.18, 130.58, 129.86, 127.54, 127.46, 126.82, 123.47, 122.80, 117.10, 44.25, 38.01, 30.80, 29.36, 28.75, 24.11, 23.09, 10.69; HRMS–MALDI (*m*/*z*): $[M + H]^+$ calcd for $C_{38}H_{34}N_2O_2S$, 582.2341; found, 582.2336.

Synthesis of **NI-PhMe$_2$-PTZ**

Compound **NI-PhMe$_2$-PTZ** was synthesized in a manner similar to [21]. Under N_2 atmosphere, compound **3** (142 mg, 0.290 mmol), phenothiazine (69.3 mg, 0.348 mmol), $Pd(OAc)_2$ (11.7 mg, 0.052 mmol), and sodium *tert*-butoxide (182.4 mg, 1.898 mmol) were dissolved in dry toluene (5 mL). Then, tri-*tert*-butylphosphine tetrafluoroborate (16.1 mg, 0.055 mmol) was added. The mixture was refluxed and stirred for 8 h under N_2. After cooling, water (20 mL) was added and the mixture was extracted with ethyl acetate (80 mL). The organic layer was separated and washed with water and brine solution

(3 × 30 mL), respectively. The organic layer was dried over anhydrous Na_2SO_4 and the solvent was evaporated under reduced pressure. The crude product was purified by column chromatography (silica gel, DCM/PE 1:5, v:v). The product **NI-PhMe$_2$-PTZ** was obtained as yellow solid. Yield: 50 mg (28.3%). Mp 121.2–122.4 °C; ^{1}H NMR ($CDCl_3$, 400 MHz) δ 0.89–0.97 (m, 6H), 1.33–1.43 (m, 8H), 1.94–2.01 (m, 1H), 1.98 (t, 1H), 2.12 (s, 6H), 4.11–4.22 (m, 2H), 6.36 (s, 2H), 6.91 (s, 3H), 7.00–7.05 (m, 3H), 7.20 (s, 2H), 7.80–7.84 (m, 1H), 8.12 (s, 1H), 8.25 (d, J = 8.13 Hz, 1H), 8.50 (s, 1H), 8.65 (d, J = 7.26 Hz, 1H); ^{13}C NMR ($CDCl_3$, 125 MHz) δ 164.55, 139.69, 139.45, 138.85, 133.63, 132.71, 132.03, 131.20, 127.35, 126.84, 123.29, 122.89, 116.24, 44.24, 38.01, 30.78, 29.70, 28.71, 24.11, 23.09, 21.19, 10.67; HRMS–MALDI (m/z): $[M + H]^+$ calcd for $C_{40}H_{38}N_2O_2S$, 610.2654; found, 610.2649.

Electrochemical studies

The cyclic voltammetry curves were recorded with a CHI610D electrochemical workstation (CHI instruments, Inc., Shanghai, China) using N_2-purged saturated solutions (**NI-PTZ**, **NI-PTZ$_2$**, **NI-Ph-PTZ**, and **NI-PhMe$_2$-PTZ** in deaerated dichloromethane, **NI-PTZ-O** in deaerated acetonitrile) containing 0.10 M Bu_4NPF_6 as a supporting electrolyte, a platinum electrode as counter electrode, a glassy carbon electrode as working electrode, and the $Ag/AgNO_3$ (0.1 M in ACN) couple as the reference electrode. The ferrocenium/ferrocene (Fc^+/Fc) redox couple was used as an internal reference. Spectroelectrochemistry was performed using a 0.1 cm path length quartz electrochemical cell equipped with gauze platinum as working electrode, a platinum wire as counter electrode, and $Ag/AgNO_3$ as reference electrode. $Bu_4N[PF_6]$ was used as the supporting electrolyte. The potential was regulated with a CHI610D electrochemical workstation (CHI instruments, Inc., Shanghai, China), and the spectra were recorded with an Agilent 8453E UV–vis spectrophotometer (Agilent Technologies Inc., USA). Samples were deaerated with N_2 for ca. 5 min before measurement and the N_2 atmosphere was kept during the measurements.

Nanosecond transient absorption spectroscopy

The nanosecond transient absorption spectra were recorded on a LP920 laser flash photolysis spectrometer (Edinburgh Instruments, Ltd., U.K.). The data (kinetic decay traces and the transient difference absorption spectra) were analyzed with the L900 software. All samples were deaerated with N_2 for ca. 15 min in collinear configuration of the pump and probe beams measurements before measurement, and excited with a nanosecond pulsed laser (Quantel Nd: YAG nanosecond pulsed laser). The typical laser power is 65 mJ per pulse.

Computational study

The ground state (S_0) geometries of compounds **NI-N-PTZ**, **NI-PTZ**, **NI-PTZ-O**, **NI-PTZ$_2$**, **NI-Ph-PTZ**, and **NI-PhMe$_2$-PTZ**, were optimized with Density Functional Theory (DFT) using the CAM-B3LYP rane-separated hybrid functional in combination with the 6-31G(d) atomic basis set [60]. The excited states geometries of S_1, T_1, and T_2 were optimized with time-dependent DFT (TD-DFT) in its Tamm–Dancoff approximation (TDA) using the same functional and basis sets as in the ground-state optimizations [61]. TDA-TD-DFT is preferred over standard (or "full") TD-DFT as the former is often more reliable for triplet excited states. Solvent effects were included using the polarizable continuum model (PCM) [62-64]. The above calculations were performed with Gaussian 16 [65]. The spin–orbit matrix elements (SOCME) between the manifold of singlet and triplet excited states were calculated with the pSOC-TD-DFT method, as implemented in ORCA 5.0.2. [61,66,67]. The latter calculations were also performed with CAM-B3LYP using the TDA approximation [61]. In the pSOC-TD-DFT calculations, relativistic effects were considered using the zero-order relativistic approximation (ZORA) and the ZORA-*def2*-TZVP basis sets [66,68,69]. pSOC-TD-DFT calculations were performed at the S_1 optimized geometry [66] for the rate calculations and at the T_1 optimized geometry in the case of the phosphorescence rate calculation. The rates of intersystem crossing (ISC) and reverse ISC (RISC) along with the reorganization energies were calculated with FCclasses making use of the vertical hessian vibronic model [70,71]. For the phosphorescence rate (k_{phos}) calculation a simplified Einstein-based expression, i.e,

$$k_r \approx \frac{\nu^2 \cdot f}{1.5} \quad (1)$$

was used, where ν is the energy gap between the involved states (in cm^{-1}) and f is the oscillator strength for the $T_1 \rightarrow S_0$ process, which was obtained from the pSOC-TD-DFT calculations.

Supporting Information

Supporting Information File 1

General experimental methods, ^{1}H NMR, ^{13}C NMR, HRMS spectra of the compounds, theoretical computation data and the photophysical data.
[https://www.beilstein-journals.org/bjoc/content/supplementary/1860-5397-18-149-S1.pdf]

Acknowledgements

D.J. is indebted to the CCIPL computational center installed in Nantes for the very generous allocation of computational time.

Funding

J. Z. thanks the NSFC (U2001222), the Fundamental Research Funds for the Central Universities (DUT22LAB610) and the State Key Laboratory of Fine Chemicals for financial support. D.E. acknowledges the Research Foundation - Flanders (FWO) and internal KU Leuven funds. D.E., and D.J. are indebted to the PHC program QCQY for supporting their collaboration.

ORCID® iDs

Kaiyue Ye - https://orcid.org/0000-0003-2543-9485
Davita M. E. van Raamsdonk - https://orcid.org/0000-0002-9447-4981
Jianzhang Zhao - https://orcid.org/0000-0002-5405-6398
Denis Jacquemin - https://orcid.org/0000-0002-4217-0708

Preprint

A non-peer-reviewed version of this article has been previously published as a preprint: https://doi.org/10.3762/bxiv.2022.24.v1

References

1. Cai, X.; Su, S.-J. *Adv. Funct. Mater.* **2018,** *28,* 1802558. doi:10.1002/adfm.201802558
2. Cao, X.; Zhang, D.; Zhang, S.; Tao, Y.; Huang, W. *J. Mater. Chem. C* **2017,** *5,* 7699–7714. doi:10.1039/c7tc02481a
3. Im, Y.; Byun, S. Y.; Kim, J. H.; Lee, D. R.; Oh, C. S.; Yook, K. S.; Lee, J. Y. *Adv. Funct. Mater.* **2017,** *27,* 1603007. doi:10.1002/adfm.201603007
4. Zhang, W.; Song, H.; Kong, J.; Kuang, Z.; Li, M.; Guo, Q.; Chen, C.-f.; Xia, A. *J. Phys. Chem. C* **2019,** *123,* 19322–19332. doi:10.1021/acs.jpcc.9b03867
5. Fukuzumi, S. *Pure Appl. Chem.* **2007,** *79,* 981–991. doi:10.1351/pac200779060981
6. Uoyama, H.; Goushi, K.; Shizu, K.; Nomura, H.; Adachi, C. *Nature* **2012,** *492,* 234–238. doi:10.1038/nature11687
7. Tanaka, H.; Shizu, K.; Miyazaki, H.; Adachi, C. *Chem. Commun.* **2012,** *48,* 11392–11394. doi:10.1039/c2cc36237f
8. Drummond, B. H.; Aizawa, N.; Zhang, Y.; Myers, W. K.; Xiong, Y.; Cooper, M. W.; Barlow, S.; Gu, Q.; Weiss, L. R.; Gillett, A. J.; Credgington, D.; Pu, Y.-J.; Marder, S. R.; Evans, E. W. *Nat. Commun.* **2021,** *12,* 4532. doi:10.1038/s41467-021-24612-9
9. Penfold, T. J. *J. Phys. Chem. C* **2015,** *119,* 13535–13544. doi:10.1021/acs.jpcc.5b03530
10. Ogiwara, T.; Wakikawa, Y.; Ikoma, T. *J. Phys. Chem. A* **2015,** *119,* 3415–3418. doi:10.1021/acs.jpca.5b02253
11. Li, M.; Liu, Y.; Duan, R.; Wei, X.; Yi, Y.; Wang, Y.; Chen, C.-F. *Angew. Chem., Int. Ed.* **2017,** *56,* 8818–8822. doi:10.1002/anie.201704435
12. Samanta, P. K.; Kim, D.; Coropceanu, V.; Brédas, J.-L. *J. Am. Chem. Soc.* **2017,** *139,* 4042–4051. doi:10.1021/jacs.6b12124
13. Kuila, S.; Ghorai, A.; Samanta, P. K.; Siram, R. B. K.; Pati, S. K.; Narayan, K. S.; George, S. J. *Chem. – Eur. J.* **2019,** *25,* 16007–16011. doi:10.1002/chem.201904651
14. Hou, Y.; Liu, J.; Zhang, N.; Zhao, J. *J. Phys. Chem. A* **2020,** *124,* 9360–9374. doi:10.1021/acs.jpca.0c07907
15. Liu, D.; El-Zohry, A. M.; Taddei, M.; Matt, C.; Bussotti, L.; Wang, Z.; Zhao, J.; Mohammed, O. F.; Di Donato, M.; Weber, S. *Angew. Chem., Int. Ed.* **2020,** *59,* 11591–11599. doi:10.1002/anie.202003560
16. Evans, E. W.; Olivier, Y.; Puttisong, Y.; Myers, W. K.; Hele, T. J. H.; Menke, S. M.; Thomas, T. H.; Credgington, D.; Beljonne, D.; Friend, R. H.; Greenham, N. C. *J. Phys. Chem. Lett.* **2018,** *9,* 4053–4058. doi:10.1021/acs.jpclett.8b01556
17. Gibson, J.; Monkman, A. P.; Penfold, T. J. *ChemPhysChem* **2016,** *17,* 2956–2961. doi:10.1002/cphc.201600662
18. Etherington, M. K.; Gibson, J.; Higginbotham, H. F.; Penfold, T. J.; Monkman, A. P. *Nat. Commun.* **2016,** *7,* 13680. doi:10.1038/ncomms13680
19. Chen, X.-K.; Zhang, S.-F.; Fan, J.-X.; Ren, A.-M. *J. Phys. Chem. C* **2015,** *119,* 9728–9733. doi:10.1021/acs.jpcc.5b00276
20. Tang, G.; Sukhanov, A. A.; Zhao, J.; Yang, W.; Wang, Z.; Liu, Q.; Voronkova, V. K.; Di Donato, M.; Escudero, D.; Jacquemin, D. *J. Phys. Chem. C* **2019,** *123,* 30171–30186. doi:10.1021/acs.jpcc.9b09335
21. Masimukku, N.; Gudeika, D.; Volyniuk, D.; Bezvikonnyi, O.; Simokaitiene, J.; Matulis, V.; Lyakhov, D.; Azovskyi, V.; Gražulevičius, J. V. *Phys. Chem. Chem. Phys.* **2022,** *24,* 5070–5082. doi:10.1039/d1cp05942d
22. Wang, B.; Zheng, Y.; Wang, T.; Ma, D.; Wang, Q. *Org. Electron.* **2021,** *88,* 106012. doi:10.1016/j.orgel.2020.106012
23. van Willigen, H.; Jones, G.; Farahat, M. S. *J. Phys. Chem.* **1996,** *100,* 3312–3316. doi:10.1021/jp953176+
24. Harriman, A.; Mallon, L. J.; Ulrich, G.; Ziessel, R. *ChemPhysChem* **2007,** *8,* 1207–1214. doi:10.1002/cphc.200700060
25. Dance, Z. E. X.; Mickley, S. M.; Wilson, T. M.; Ricks, A. B.; Scott, A. M.; Ratner, M. A.; Wasielewski, M. R. *J. Phys. Chem. A* **2008,** *112,* 4194–4201. doi:10.1021/jp800561g
26. Epelde-Elezcano, N.; Palao, E.; Manzano, H.; Prieto-Castañeda, A.; Agarrabeitia, A. R.; Tabero, A.; Villanueva, A.; de la Moya, S.; López-Arbeloa, Í.; Martínez-Martínez, V.; Ortiz, M. J. *Chem. – Eur. J.* **2017,** *23,* 4837–4848. doi:10.1002/chem.201605822
27. Hou, Y.; Zhang, X.; Chen, K.; Liu, D.; Wang, Z.; Liu, Q.; Zhao, J.; Barbon, A. *J. Mater. Chem. C* **2019,** *7,* 12048–12074. doi:10.1039/c9tc04285g
28. Filatov, M. A. *Org. Biomol. Chem.* **2020,** *18,* 10–27. doi:10.1039/c9ob02170a
29. Gibbons, D. J.; Farawar, A.; Mazzella, P.; Leroy-Lhez, S.; Williams, R. M. *Photochem. Photobiol. Sci.* **2020,** *19,* 136–158. doi:10.1039/c9pp00399a
30. Shao, S.; Gobeze, H. B.; Bandi, V.; Funk, C.; Heine, B.; Duffy, M. J.; Nesterov, V.; Karr, P. A.; D'Souza, F. *ChemPhotoChem* **2020,** *4,* 68–81. doi:10.1002/cptc.201900189
31. Bassan, E.; Gualandi, A.; Cozzi, P. G.; Ceroni, P. *Chem. Sci.* **2021,** *12,* 6607–6628. doi:10.1039/d1sc00732g
32. Zhang, X.; Wang, Z.; Hou, Y.; Yan, Y.; Zhao, J.; Dick, B. *J. Mater. Chem. C* **2021,** *9,* 11944–11973. doi:10.1039/d1tc02535j
33. Chen, X.; Xiao, X.; Zhao, J. *J. Mater. Chem. C* **2022,** *10,* 4546–4557. doi:10.1039/d1tc04888k
34. Ward, J. S.; Nobuyasu, R. S.; Batsanov, A. S.; Data, P.; Monkman, A. P.; Dias, F. B.; Bryce, M. R. *Chem. Commun.* **2016,** *52,* 2612–2615. doi:10.1039/c5cc09645f

35. Peng, Q.; Fan, D.; Duan, R.; Yi, Y.; Niu, Y.; Wang, D.; Shuai, Z. *J. Phys. Chem. C* **2017,** *121,* 13448–13456. doi:10.1021/acs.jpcc.7b00692
36. Hou, Y.; Kurganskii, I.; Elmali, A.; Zhang, H.; Gao, Y.; Lv, L.; Zhao, J.; Karatay, A.; Luo, L.; Fedin, M. *J. Chem. Phys.* **2020,** *152,* 114701. doi:10.1063/1.5145052
37. Sasaki, S.; Hattori, K.; Igawa, K.; Konishi, G.-i. *J. Phys. Chem. A* **2015,** *119,* 4898–4906. doi:10.1021/acs.jpca.5b03238
38. Wang, Z.; Zhao, J.; Di Donato, M.; Mazzone, G. *Chem. Commun.* **2019,** *55,* 1510–1513. doi:10.1039/c8cc08159j
39. Chen, K.; Kurganskii, I. V.; Zhang, X.; Elmali, A.; Zhao, J.; Karatay, A.; Fedin, M. V. *Chem. – Eur. J.* **2021,** *27,* 7572–7587. doi:10.1002/chem.202100611
40. Chen, K.; Taddei, M.; Bussotti, L.; Foggi, P.; Zhao, J.; Di Donato, M. *ChemPhotoChem* **2020,** *4,* 487–501. doi:10.1002/cptc.201900294
41. Dong, Y.; Sukhanov, A. A.; Zhao, J.; Elmali, A.; Li, X.; Dick, B.; Karatay, A.; Voronkova, V. K. *J. Phys. Chem. C* **2019,** *123,* 22793–22811. doi:10.1021/acs.jpcc.9b06170
42. Chen, K.; Zhao, J.; Li, X.; Gurzadyan, G. G. *J. Phys. Chem. A* **2019,** *123,* 2503–2516. doi:10.1021/acs.jpca.8b11828
43. Imran, M.; Sukhanov, A. A.; Maity, P.; Elmali, A.; Zhao, J.; Karatay, A.; Mohammed, O. F.; Voronkova, V. K. *J. Phys. Chem. B* **2021,** *125,* 9244–9259. doi:10.1021/acs.jpcb.1c03537
44. Mi, Q.; Chernick, E. T.; McCamant, D. W.; Weiss, E. A.; Ratner, M. A.; Wasielewski, M. R. *J. Phys. Chem. A* **2006,** *110,* 7323–7333. doi:10.1021/jp061218w
45. Collini, M. A.; Thomas, M. B.; Bandi, V.; Karr, P. A.; D'Souza, F. *Chem. – Eur. J.* **2017,** *23,* 4450–4461. doi:10.1002/chem.201700200
46. Schuster, D. I.; Cheng, P.; Jarowski, P. D.; Guldi, D. M.; Luo, C.; Echegoyen, L.; Pyo, S.; Holzwarth, A. R.; Braslavsky, S. E.; Williams, R. M.; Klihm, G. *J. Am. Chem. Soc.* **2004,** *126,* 7257–7270. doi:10.1021/ja038676s
47. Dance, Z. E. X.; Mi, Q.; McCamant, D. W.; Ahrens, M. J.; Ratner, M. A.; Wasielewski, M. R. *J. Phys. Chem. B* **2006,** *110,* 25163–25173. doi:10.1021/jp063690n
48. Ventura, B.; Bertocco, A.; Braga, D.; Catalano, L.; d'Agostino, S.; Grepioni, F.; Taddei, P. *J. Phys. Chem. C* **2014,** *118,* 18646–18658. doi:10.1021/jp5049309
49. Suneesh, C. V.; Gopidas, K. R. *J. Phys. Chem. C* **2010,** *114,* 18725–18734. doi:10.1021/jp107606t
50. Hviid, L.; Brouwer, A. M.; Paddon-Row, M. N.; Verhoeven, J. W. *ChemPhysChem* **2001,** *2,* 232–235. doi:10.1002/1439-7641(20010417)2:4<232::aid-cphc232>3.0.co;2-3
51. Pearce, N.; Davies, E. S.; Horvath, R.; Pfeiffer, C. R.; Sun, X.-Z.; Lewis, W.; McMaster, J.; George, M. W.; Champness, N. R. *Phys. Chem. Chem. Phys.* **2018,** *20,* 752–764. doi:10.1039/c7cp06952a
52. Ohkubo, K.; Kotani, H.; Shao, J.; Ou, Z.; Kadish, K. M.; Li, G.; Pandey, R. K.; Fujitsuka, M.; Ito, O.; Imahori, H.; Fukuzumi, S. *Angew. Chem., Int. Ed.* **2004,** *43,* 853–856. doi:10.1002/anie.200352870
53. Geiß, B.; Lambert, C. *Chem. Commun.* **2009,** 1670–1672. doi:10.1039/b820744e
54. Hankache, J.; Wenger, O. S. *Chem. Commun.* **2011,** *47,* 10145–10147. doi:10.1039/c1cc13831f
55. Blas-Ferrando, V. M.; Ortiz, J.; Ohkubo, K.; Fukuzumi, S.; Fernández-Lázaro, F.; Sastre-Santos, Á. *Chem. Sci.* **2014,** *5,* 4785–4793. doi:10.1039/c4sc01579g
56. McGarrah, J. E.; Kim, Y.-J.; Hissler, M.; Eisenberg, R. *Inorg. Chem.* **2001,** *40,* 4510–4511. doi:10.1021/ic015559u
57. Suzuki, S.; Sugimura, R.; Kozaki, M.; Keyaki, K.; Nozaki, K.; Ikeda, N.; Akiyama, K.; Okada, K. *J. Am. Chem. Soc.* **2009,** *131,* 10374–10375. doi:10.1021/ja904241r
58. Saigo, M.; Miyata, K.; Tanaka, S.; Nakanotani, H.; Adachi, C.; Onda, K. *J. Phys. Chem. Lett.* **2019,** *10,* 2475–2480. doi:10.1021/acs.jpclett.9b00810
59. Zhao, X.; Sukhanov, A. A.; Jiang, X.; Zhao, J.; Voronkova, V. K. *J. Phys. Chem. Lett.* **2022,** *13,* 2533–2539. doi:10.1021/acs.jpclett.2c00435
60. Yanai, T.; Tew, D. P.; Handy, N. C. *Chem. Phys. Lett.* **2004,** *393,* 51–57. doi:10.1016/j.cplett.2004.06.011
61. Hirata, S.; Head-Gordon, M. *Chem. Phys. Lett.* **1999,** *314,* 291–299. doi:10.1016/s0009-2614(99)01149-5
62. Miertuš, S.; Scrocco, E.; Tomasi, J. *Chem. Phys.* **1981,** *55,* 117–129. doi:10.1016/0301-0104(81)85090-2
63. Miertuš, S.; Tomasi, J. *Chem. Phys.* **1982,** *65,* 239–245. doi:10.1016/0301-0104(82)85072-6
64. Pascual-ahuir, J. L.; Silla, E.; Tuñon, I. *J. Comput. Chem.* **1994,** *15,* 1127–1138. doi:10.1002/jcc.540151009
65. *Gaussian 16;;* Gaussian, Inc.: Wallingford, CT, 2016.
66. Wang, F.; Ziegler, T. *J. Chem. Phys.* **2005,** *123,* 154102. doi:10.1063/1.2061187
67. Neese, F. *Wiley Interdiscip. Rev.: Comput. Mol. Sci.* **2012,** *2,* 73–78. doi:10.1002/wcms.81
68. van Lenthe, E.; Baerends, E. J.; Snijders, J. G. *J. Chem. Phys.* **1993,** *99,* 4597–4610. doi:10.1063/1.466059
69. Weigend, F.; Ahlrichs, R. *Phys. Chem. Chem. Phys.* **2005,** *7,* 3297–3305. doi:10.1039/b508541a
70. Santoro, F.; Cerezo, J. FC classes3, a code for vibronic calculations; 2019.
71. Avila Ferrer, F. J.; Santoro, F. *Phys. Chem. Chem. Phys.* **2012,** *14,* 13549–13563. doi:10.1039/c2cp41169e

License and Terms